Deciphering lodging resistance in oat and other cereal crops

A DISSERTATION
SUBMITTED TO THE FACULTY OF
UNIVERSITY OF MINNESOTA
BY

Alexander Q. Susko

IN PARTIAL FULFILLMENT OF THE REQUIREMENTS
FOR THE DEGREE OF
DOCTOR OF PHILOSOPHY

Kevin P. Smith, advisor

August 2019

Acknowledgements

Thank you to my advisor Dr. Kevin Smith, who quickly and unexpectedly took me on as a PhD student. The skills and credentials I have built since have altered my life in a good way. I also thank my committee (Drs. Cory Hirsch, Aaron Lorenz, and Peter Marchetto) for their review of this dissertation.

Thank you to the large group of people at the University of Minnesota involved with the cereal grains lodging projects of 2017 through 2019 and beyond. Notably I thank Dr. D. Jo Heuschele for her guidance and collaboration on many of these large, interdisciplinary projects. I thank members of the UMN Bioproducts and Biosystems Engineering Department: my committee member and shop guru Dr. Peter Marchetto for all of his electronics, building, and analytical advice, along with Stijn Vandycke, Fletcher Gilbertson, Daniel Furuta, Leonard Reynolds, Ali Moghimi, David Schmidt, and Tyler Nigon. I thank members of the UMN Civil, Environmental, and Geo- Engineering for their help on the mechanical aspects of cereal crop lodging and wind tunnel testing: Dr. Michele Guala, Dr. Dominik Schillinger, Tarun Gangwar, and Chris Feist.

Thank you to the members of Dr. Kevin Smith's lab. I highlight the work and assistance of Dimitri von Ruckert, whose organization of equipment, field space, and lab personnel made these projects possible. Thank you to all of the Oat lab personnel for building and data collection assistance: Erik Boysen, Joan Barreto, Aubrey Howerton, and Madeline Humphrey. Thank you to Karen Beaubien for genotyping assistance, as well as the broader lab group for helpful comments on this work during lab meetings: Ian McNish, Jeffrey Neyhart, John Hill Price, Becky Zhong, Jerry Franckowiak, Ed Schiefelbien, and Guillermo Velasquez.

Thank you to my family for their support: my wife Anne, parents John and Megan, sister Abby, parent's in-law Dave and Denise, brother in- law John, and all our extended family and friends. I extend a special thank you to my good friends Rob Bechtel and Katie Krieger, who housed me during my visits to Saint Paul as I finished this dissertation.

Finally, I thank my funding sources. Minnesota Department of Agriculture Grant No. 122130 and University of Minnesota (UMN) Rapid Agricultural Response Fund Grant No. AES00RR234 funded material costs associated with the research, as well as my initial appointment. My subsequent appoints and interdisciplinary collaboration was made possible by a UMN Informatics Initiative-MnDRIVE Robotics, Sensors, and Advanced Manufacturing graduate assistantship and University of Minnesota Graduate School Interdisciplinary Doctoral Fellowship.

Dedication

This dissertation is dedicated to the reader, whom I hope will find it informative and useful.

Abstract

Lodging impedes the successful cultivation of oat and other cereal crops in the upper midwestern United States. Lodged cereals not only possess reduced grain yields, but also decreased grain quality. This dissertation first conceives of a camera system to capture plant movement in the wind in the field via a 360-degree field of view camera, followed by a video analysis pipeline to quantify the frequency and amplitude of cereal stem movement under varying wind conditions in the field. The natural oscillating frequencies and amplitudes of stems were dependent on wind speeds and at the cultivar, crop level. Nonetheless, the substantial environmental effects in the field that induce lodging make discovering specific morphologies that confer lodging resistance difficult. Next, in seeking to better identify promising morphological targets for breeding and selecting lodging resistance in cereal crops, a diverse panel of 38 cereal cultivars (oat, wheat, barley) were subjected to replicated testing in a wind tunnel. Wind tunnel testing revealed that a cereal ideotype consisting of low total biomass, high stem strength, and high stem elasticity should confer increased lodging resistance. A field study using the camera system to quantify aspects of plant movement and correlated these phenotypes with physical plant traits is presented next, which indicated that patterns of plant movement are spatially independent in a randomized complete block design of 16 cereal cultivars and that the relationships between plant height, heading date, and plant movement vary among the major cereal crops. Finally, a GWAS and QTL validation study is presented on lodging in oat, which revealed significant marker trait associations

for plant height, heading date, and stem snapping, though only QTL for plant height and heading date were successfully validated in derived biparental populations.

Table of Contents

List of Tables

Chapter 3

Chapter 4

Chapter 5

Chapter 6

List of Figures

Chapter 2

Chapter 3

Chapter 4

Chapter 5

Chapter 6

Chapter 1:

Introduction and Literature Review

Alexander Q. Susko[1]

[1]University of Minnesota Dept. of Agronomy and Plant Genetics, 411 Borlaug Hall, 1991 Upper Buford Cir. St. Paul MN 55108

This dissertation is broadly focused on understanding lodging resistance in cereal crops, with attention given to oat (*Avena sativa* L.) as elite cultivars are consistently less lodging resistant than those of other cereal crops such as wheat (*Triticum aestivum* L.). Severe weather events that induce lodging are becoming more common in Minnesota as a result of climate change. Increasing atmospheric temperature and moisture have the potential to increase the frequency and severity of thunderstorms in the upper Midwest (Kunkel et al, 2013). Ten separate billion-dollar severe weather events since 2000 that have affected Minnesota and other midwestern states have already caused a combined $42.2 billion (CPI-adjusted) in economic losses (NOAA, 2017). These costs include crop losses, which will likely increase as severe weather events become more frequent. Breeding agricultural crops, including oats, that are more resistant to lodging is one step to reduce to the economic costs anticipated with more severe weather. Insights for lodging resistance are drawn from examining phenotypes in the major crops of oat, wheat, and barley to inform future selection targets for lodging resistant cereal ideotypes. The literature review that follows begins with a background on oat cultivar development and breeding, and then transitions to a review on the general problem of lodging in cereal crops.

Background on oat

Oat (*Avena sativa* L.) is an allohexaploid, self-pollinating cereal grain with a long but incompletely understood history as a food crop. The genus *Avena* contains five cultivated species and 17 wild species, whose center of diversity spans the Mediterranean basin east to Asia Minor (Moore-Colyer, 1995). Prior to domestication of *A. sativa*,

humans in the Jordan River Valley were cultivating wild oat (*A. sterilis* L.) as early as 11,400 years before present (BP) (Weiss et al, 2006). The modern *A. sativa* contains subgenomes from wild species, including *A. magna* and *A. murphyi*, which are hypothesized to impart non-shattering and reduced awn traits in domesticated oat (Ladizinsky, 1995). Subsequent research utilizing a greater number of molecular markers has identified genetic loci governing shattering and awn formation within progeny of an *A. magna* and *A. sativa* cross (Oliver et al, 2011). Current genomic resources in oat are insufficient for inferring timelines corresponding to selective sweeps and dispersal of domesticated oat from marker data. However, archeological evidence indicates that early oat domesticates were brought to Greece by 5,000 years BP, and to the rest of southern Europe between 4- and 3,000 years BP (Moore-Colyer, 1995; Zohary et al 2012). The growth of the Roman Empire is thought to have spread domesticated oat to northern Europe, as oat seeds have been found in the remains of Roman military forts on the British Isles dating to 1900 years BP (Moore-Colyer, 1995).

Oat variety development has become more targeted over time. Early variations of domesticated oat are described from 14th century England, where oats were assigned different price classes depending on the ease of hulling ("naked" vs "non-naked") and seed color (Thirsk, 1967). By the 19th century, domesticated oat varieties were readily differentiated by geographic origin and morphological traits (Moore-Colyer, 1995). One such variety was 'Red Rustproof', a non-pureline variety with large variation in morphological and agronomics traits (Fehr, 1987). Since first documented in 1797, 'Red Rustproof' represents the first described oat variety grown in the United States, with

cultivation of ‘Red Rustproof’ continuing through the 1920s (Fehr, 1987). Importantly, it is thought that selection within this heterogenous variety gave rise to over 100 pureline US oat cultivars (Coffman, 1961). Modern oat varieties in the 20th and 21st centuries are inbred lines that are derived from segregating populations for traits of interest. (Fehr, 1987). Systemic breeding, along with improved agronomic practices, have led to increased oat yields and varieties with improved nutritional qualities.

Oat has long been used for both human and animal consumption. The thousands of oat seeds that have been found at Jordan River Valley sites indicate that oat was a dietary staple of humans in modern day Israel, Jordan and Syria around 11,400 years BP (Weiss et al, 2006). In medieval Europe, oats were milled into meal for use in bread, cakes, and porridge, but they were especially valuable as feed for horses (Moore-Colyer, 1995). Today, oat is consumed directly by humans in the form of oatmeal or in processed granola products, but also has other uses including extracted cosmetic and therapeutic oils (Potter et al, 1997). Oat remains a staple horse feed, with increasing protein in the oat feed mixture resulting in faster race time for race horses (Glade, 1983). Oat is also used as a forage, typically harvested just prior to heading (Stuthman and Marten, 1972). A minor but notable use for oat includes use as a malt, although the high lipid content makes the malt much more susceptible to going rancid than barley (Peterson, 1988).

Diverse uses for oat have led to a wide variety of breeding targets and changes in traits over time. Domestication in oat resulted in selection for non-shattering, reduced awns, and minimized lemma pubescence (Oliver et al, 2011). Each controlled by a small

number of major effect QTL, these traits enabled seed saving and improved seed processing by early domesticators (Oliver et al, 2011). Most traits of interest to oat breeders are highly quantitative. Grain yield is the most important trait in oat and is responsive to selection, with average annual yield gains of 0.8% from 1923-1980 measured in Minnesota germplasm (Wych, 1983). In one short term recurrent selection experiment, gains in yield of 3.8% per generation were realized (Payne et al, 1986). Traits correlated with greater yield in oat include above ground dry mass, increased time to heading, and reduced lodging (Payne et al, 1986; Wych 1983). It is therefore likely that selection for higher yields has increased oat vigor over time. Disease resistance is the second most critical trait in oat breeding. While not static over time, understanding of disease resistance in oat has led to the introduction of horizontal and vertical resistance against fungal diseases such as oat stem and crown rust (Fehr, 1987; Klos et al 2017). Following yield and disease resistance, grain quality is the focus of much oat breeding effort. Protein is a critical trait, given the whole grain consumption of oats by both humans and livestock. High protein oat varieties range between 17-21% protein in the grain depending on soil fertility, while most oat varieties contain between 14-18% protein (Fehr, 1987). The nutritional benefit of oat has largely been focused on increasing grain protein, with protein yield responding to selection with 2.1% per cycle (McFerso et al, 1991). Forage quality has also been the target of breeding in a subset of oat germplasm for forage use. Forage nutritional traits, including in vitro digestible dry matter and crude protein, possess selectable genetic variation across oat varieties (Stuthman, 1972).

The traits important to oat breeders have expanded with technological advances that enable their quantification. Prior to 1950 traits of major importance were yield, stem rust resistance, and lodging resistance (Minnesota Report 247, 2000). In cold climates such as the upper Midwest, agronomic conditions such as planting date were also researched in the late 19th century to improve oat yields (Minnesota Report 247, 2000). These selection targets remain important today. Currently there is a greater emphasis on grain quality, with specific selection for white seed color, increased protein levels, and increased beta glucan levels- a soluble fiber that lowers cholesterol in humans (Braaten et al, 1994). Lodging resistance continues to be a major focus for breeding and improvement, especially given new phenotyping technologies available today. Though genetic markers associated with lodging resistance have been described in oat (Tumino et al, 2017), little is known about the plant anatomy that is most important for lodging resistance in oat under wind stress. A better understanding of the plant anatomy that contributes to lodging in oat will be a major way to further improve the agronomic performance of this cereal crop in the face of more frequent severe weather events in a changing midwestern climate.

Background on lodging in cereal crops

Lodging in cereal crops is primarily quantified by breeders using a visual scale (ie 0-9 rating) to select for lodging resistance. Visual scoring of lodging has been successful in identifying genetic markers linked to quantitative trait loci (QTL) for use in marker assisted breeding to improve lodging resistance in oat. Linkage mapping studies for lodging resistance using SSR, DArT, AFLP markers in oat have identified unique QTL

for lodging visual scores (Tanhaunpaa et al, 2012; Hizbai et al, 2012) and visual scores co-localized with height and heading date (Tanhaunpaa et al, 2012). QTL by environment interaction has also been found to be significant for lodging visual score QTL in oat, as lodging pressures can vary significantly across environments (De Koeyer et al, 2004). Given the near certainty of not experiencing the same lodging pressures year over year, understanding lodging at a more precise level via the phenotypes that contribute to more resilient plant-wind interactions could help to generate better selection targets for improving lodging resistance in breeding programs.

At a level more detailed than the visual severity score, lodging can be described as stem lodging, which typically occurs closer to maturity as cereal stems stiffen, or root lodging, which typically occurs after heading and at lower velocities than stem lodging (Baker et al, 2014). Root lodging is the more severe type of lodging in cereals with respect to yield loss, as the subsequent shading lodged plants cast upon each other during grain filling can reduce yields by 30-40% without accounting for yield loss due to issues with harvestability (Weibel and Pendleton, 1964). Root also occurs over multiple oscillations of the stem, with each oscillation further stressing the culm via a drag force induced torque on the stem tissue (Baker et al, 2014). An inability of the cereal stem to resist the torques applied via distributing the stress along the stem length will result in root lodging (Grafius and Brown, 1954). The core of root and stem lodging resistance at the macroscopic (i.e. plant level) scale could thus lie in accurate description of how cereal stems *respond* to loads (wind-induced drag forces) based on their morphological and physiological components.

The movement of cereal crop stems and in the wind is a recurring theme throughout this dissertation. Plant movement prior to lodging represents yet another dimension of phenotypes to study to help explain lodging resistance in cereals: that of the oscillating or natural frequency (measured in cycles per second, Hz) with some amount of amplitude. Individual plant stems can be physically modeled as a vibrating system that oscillates back and forth at a natural frequency when excited by the wind. This oscillating frequency can be thought of as a consequence of morphological and environmental factors combining to produce a pattern of plant movement (De Langre, 2008). In framing cereals as a vibrating system, morphological or physiological variables that influence plant-wind interactions can be identified to better understand the complex problem of lodging resistance. At a basic level, the natural frequency is equivalent to the square root of the ratio of stem stiffness to stem mass per unit length (Flesch and Grant, 1991): implying that stronger stems oscillate at a higher frequency, and heavier stems at a lower frequency, with incremental changes to either affecting the natural frequency in a non-linear fashion. Because stems are only fixed at the culm, the movement equation becomes more complicated, involving structural and aerodynamic damping coefficients, stem area exposed, and other parameters (Flesch and Grant, 1991). An interpretation of the previously cited work is that increasing wind velocity will induce a drag force and effectively the mass per unit length which, holding other parameters constant, will decrease the frequency of oscillation. If the plant stem cannot resist these drag forces, root lodging will occur over multiple oscillations (Baker, 1995). As such, a plant with morphological or physiological properties to counteract these drag forces would be

expected to dampen these oscillations and possess a higher frequency of oscillation, even under high winds, and should prove more lodging resistant.

The vibrating system composed of a driving force (wind-induced drag) and an oscillating rod fixed at one end (cereal crop) can allow for analysis of relationships between physiological variables and patterns in plant movement to optimize plant lodging resistance. Put another way, changes in one aspect of plant morphology (ie stem length) will manifest as changes in movement under varying driving forces (wind speeds), with some proportion of the variation in stem length explaining changes in plant movement after accounting for variation in the driving force. A number of applied studies have examined how plant morphology alters the movement characteristics in cereal crops, as well as the lodging tolerance. A model of wheat lodging correctly predicted the lodging resistance of 90% of wheat cultivars studied considering many parameters, including the center of gravity height, natural frequency, stem base radius, and structural rooting depth (Baker et al, 1998). The authors found that a natural frequency of 0.5 Hz resulted in a 93% seasonal lodging risk, while a natural frequency of 1.5 Hz resulted in a 11% seasonal lodging risk (Baker et al, 1998). The natural frequency of wheat cultivars can be manipulated via agronomic management, notably through the application of the plant growth regulators Cycol and Terpal, as well as reducing nitrogen to increase the natural frequency of the stem (Berry et al, 2000). In comparative studies of wheat and barley, two spring barley cultivars averaged mean frequencies of 0.67 Hz and 0.6 Hz, while those of the two wheat cultivars averaged 1 Hz and 1.01 Hz (Berry et al, 2006). Additionally, the flexural rigidity (a measure of the force required to bend an object into a

unit of curvature) was nearly four times as high for the wheat cultivars relative to barley, indicating an increased capability of wheat stems to resist bending that could contribute to higher natural frequencies (Berry et al, 2006). The effect of panicle mass is also a subject of empirical study on the natural stem frequency, with an exponential decrease in the stem frequency observed as the panicle mass increases, all other properties of the stem held constant (Zebrowski, 1999). Barley and wheat stems both demonstrate lower Young's moduli (a measurement of material stiffness) when green as opposed to mature, implying less force is required to induce stem failure and root lodging in cereals before senescence (Neenan and Spencer-Smith, 1975). The majority of the studies mentioned above have used a manual method of natural frequency estimation, accomplished by pulling back a stem and manually timing the oscillations visually (Berry et al, 2004). The proliferation of new camera technology could enable systematic quantification of aspects of plant movement for purposes of improving the cereal germplasm via high throughput methods. In doing so, large-scale validation of the morphology and physiology that contribute to higher stem natural frequencies in cereal crops would be possible, leading to new selection targets for cereal breeding programs that could accelerate the selection of lodging resistant varieties.

High throughput phenotyping technologies have provided the means to quantify new aspects of plant biology. Recent explosions in high throughput phenotyping capabilities, from improved cameras and unmanned aerial vehicles that can capture data large numbers of plots to sophisticated image analysis, can quantify previously undiscovered phenotypes (Singh et al, 2016). Quantifying dynamic phenotypes such as

plant movement, however, remains largely unexplored. The earliest published methodologies for quantifying the oscillation frequency of plants was via a stopwatch in forest trees (Sugden, 1962). Digital data on plant movement from a micro logger (accelerometer, gyrometer) data acquisition system further allowed theoretical assumptions of plant movement to be refined on the individual plant level in maize by the late 1980s (Flesch and Grant, 1991). The advent of digital video cameras have enabled new quantifications of plant movement, such as adapting the technique of Particle Image Velocimetry (PIV) to light reflected off of an alfalfa canopy to map turbulent air flows over the crop canopy (Py et al, 2005). Interactions between individual plants have also been quantified through video analysis, specifically by tracking changes in color within a given region of a video as stems oscillate and collide with each one another (Doare et al, 2004). By quantifying plant movement without interference as common methods such as a pull-back oscillation test (Berry et al, 2004), plant movement data derived from video analysis could better estimate the variability in plant movement under different driving forces (windspeeds) and identify physiological relationships with movement that are strong enough to be detected under varying wind conditions.

In this dissertation, I investigate the physiological and genetic basis for lodging resistance in oat. I also incorporate other cool-season cereals (wheat, 2-row barley, and 6-row barley) with diverse morphologies to better understand the traits that confer lodging resistance. This investigation is broken up into five main objectives:

1. Developing a hardware and camera system to capture lodging and crop movement under high wind conditions in the field
2. Developing a video analysis method to quantify wind induced plant movement in the field
3. Quantifying plant drag coefficients and stem bending under controlled wind tunnel conditions
4. Elucidating how plant morphology influences plant movement under field wind conditions and subsequent lodging outcomes
5. Identifying and validating loci associated with lodging resistance in a diverse oat population.

Chapter 2:

An automatable, field camera track system for phenotyping crop lodging and crop movement[*]

Alexander Q. Susko[1], Fletcher Gilbertson[2], D. Jo Heuschele[1], Kevin P. Smith[1], and Peter Marchetto[2]

[1]University of Minnesota Department of Agronomy and Plant Genetics

411 Borlaug Hall, 1991 Upper Buford Circle, St. Paul, MN, USA, 55108

[2]University of Minnesota Department of Bioproducts and Biosystems Engineering

1390 Eckles Ave., St. Paul, MN, USA, 55108

[*] AQS Conceived of the research in this chapter, organized construction, performed construction, and wrote the manuscript. FG provided technical expertise on the project and created the blueprints in the figures. DJH and KPS reviewed the research and provided manuscript edits, while PM served as the principal investigator. A version of this chapter is published in the journal HardwareX:

Susko, A.Q., Gilbertson, F., Heuschele, D.J., Smith, K. and Marchetto, P., 2018. An automatable, field camera track system for phenotyping crop lodging and crop movement. HardwareX, 4, https://doi.org/10.1016/j.ohx.2018.e00029

Introduction

High throughput phenotyping provides plant breeders detailed and timely information on plant traits. Many of the traits that plant breeders study exhibit quantitative variation, such as lodging resistance (stem breakage or falling over). Some quantitative traits can be measured objectively (eg. grain yield) while others such as lodging are typically measured subjectively using a visual rating scale (1-10) (Simko and Piepho, 2011). Though genes associated with lodging can be inferred from these rating scales (Tumino et al, 2017), the simplification of such complex phenotypes in to subjective scales reduces a breeder's ability to estimate precise genetic effects for the trait. Quantitative traits such as lodging are also influenced by environmental conditions (precipitation, breezes, and temperature) over the growing season that affect the plant response to severe wind events. Thus, providing more continuous data on crop lodging and any morphological changes prior to lodging in the field could improve selection for lodging resistance and many other quantitative plant traits.

The hardware presented enables detailed, automatable video imaging of agricultural research plots for capturing continuous variation of crop lodging and plant movement. The camera track system represents one of many new methods of high throughput phenotyping in plant breeding and other agricultural disciplines. Crop lodging severity has been quantified from unmanned aerial vehicle (UAV) images (Chapman et al, 2014), however UAVs may not be operable in the presence of wind gusts that induce plant movement and lodging in situ. Our fixed system can address these limitations because it can operate under the high wind conditions that initiate plant movement and

lodging but prohibit drone flights. Commercial track based phenotyping systems exist, such as the PhenoSpex FieldScan , but the designs we present are open source and are simplified for smaller research plots. Furthermore, the hardware system could serve as the base for other sensors that offer data collection in a 360 degree field of view, and represents an accessible design for breeders looking to obtain large amounts of image and video data on plant traits in an automated fashion. Additionally, the system lends itself to quantifying novel aspects of plant-wind interaction (such as plant movement) from the video data collected.

The hardware presented constitutes an automatable camera system for the video or still imaging of agricultural research plots. The track system comprises commercially available hardware and electronics that allow for automatable high throughput phenotyping of lodging and plant movement. Material costs for the track system approximate the price of a commercial imaging drone. Additionally, the track system can be operated with higher frequency and greater autonomy than commercial imaging drones. The hardware as presented is designed to accommodate 360 degree field of view cameras. The maximum load on the track for the presented configuration is 22.7 kg, which is far greater than the typical mass of a 360 degree field of view camera (~100g). This opens the possibility of deploying heavier sensing equipment, such as lidar detectors. Movement of the camera along the track is carried out by a motor driven through UNIX commands executed on a Raspberry Pi. This system was built to image crop lodging and plant movement in agricultural research plots, but it could be used to quantify many other aspects of plant growth such as, maturity and/ or nutrient

deficiencies through the use of image data. The dimensions of this system are customizable to the research field and crop system under study. For our purposes, the track system is designed to span a 39.6 m (130') research field, by 36.6 m (120') in width at 2.7 m (9') off the ground.

Materials and Methods

Building instructions for the camera track system are provided in the appendix, with Appendix I containing the design files summary and location of the design files in an online repository, Appendix II containing the Bill of Materials, Appendix III the step-by-step building and safety instructions, and Appendix IV supplemental figures 1-4 displaying blueprints and wiring diagrams for the camera track system design. All design files are available online (Susko, 2018a).

Results and Discussion

We imaged an agricultural field experiment using this hardware during the summer of 2017 (Minnesota Agricultural Experiment Station, St. Paul, MN). The field experiment was designed to evaluate the ability of novel phenotyping methods to investigate lodging in cereal crops. The experiment contained four varieties of four different cereal grains (wheat, oat, 2-row barley, and 6-row barley) for a total of 16 lines. Varieties were planted in single row plots of 3.04 m (10') in length with 61 cm (2') spacing between rows. Varieties were arranged in a randomized complete block design with each variety replicated 8 times. Furthermore, this design was planted at four different planting dates, each spaced one week apart in adjacent regions of the field. The

camera system bisected the center of each planting date of the experimental design, allowing video imaging of different crop genotypes and growth stages with one pass of the camera. For analysis purposes, the most useful portion of the camera field of view encompassed 4 replicates: 2 on either side of the camera track (a 55' (16.75m) wide cross section). In total, the camera mounted to this hardware captured 72 Gb of hemispherical 4K video that was used to detect crop lodging and plant movement at high throughput. The installed camera track is shown in Figure 1.

We captured two different classes of video using this hardware during the 2017 field season. "Moving video" constituted a video of the entire field experiment as the camera traveled down and back the length of the camera track. "Stationary video" captured specific regions of the experiment over multiple timepoints, with the camera stopping at a predetermined QR code along the track to record plant movement under the wind conditions present at the recording time. These modes of hardware operation allowed for the imaging of both crop lodging and the movement experienced by plants prior to a lodging event.

We present sensor data from the onboard accelerometer, gyrometer, and magnetometer of the 360FLY camera to show properties of the camera track during a typical moving video. The data from the run presented represents forward motion along the entire 130 foot span taken on 19-July 2017. The run duration lasted 9 minutes 50 seconds, resulting in an average camera speed of 4.02 m (13.2') per minute. Similar camera speeds were observed for all runs taken during July 2017, with slower speeds following successively cloudy days when the battery contained less charge from the solar

panels. Wind gusts on operating days ranged between 0 and 12.5 mph (20.1 kph). Small areas of variable acceleration and gyration existing along the camera track at the Track Connectors. The magnitude of acceleration taken as the square root of the squared sum of the X and Y axes from the 360FLY accelerometer revealed regular peaks at track connectors, with some over 5 m/s in acceleration magnitude (Figure 2 A). The magnitude of gyration was much lower and not as regular at track connectors (Figure 2 B). The steel posts interfered substantially with the 360FLY 4K camera magnetometer, resulting in inaccurately sensed direction throughout the entire run (Figure 2 C). Filing the track segments smooth at each track connector could lead to smoother camera movement and reduce the magnitude of acceleration in these areas along the camera track system to minimize errors in subsequent video analysis.

From the 2.74m (9') height of this camera track, the edges of a 36.57m (120') diameter research field are in view (Figure 3). Crop movement in response to wind was captured using this hardware. Videos were taken under varying wind speeds at fixed locations within each planting date, comprising 27.2 Gb of total videos. Utilizing MATLAB we were able to quantify plant movement in this hemispherical video as the frequency and magnitude with which plant stems oscillate back and forth under windy conditions. This data analysis was done by estimating the mean red value of pixels within a square foot adjacent to the crop row, normalizing to the red square in the QR code, iterating this calculation over all frames, and then plotting the results (Figure 4). Our results showed movement of two different oat varieties is distinguishable based on the frequency and amplitude of the oscillations (Figure 4). This camera track is uniquely

suited to capturing real time plant traits at different plot locations within an experimental field, however the system can capture video of plant phenotypes after an environmental event similar to a commercial drone. We were able to phenotype lodging within our experimental field using video in less time than manually scoring in the field, the typical method for recording lodging data in crops (Figure 3).

Both automated (using motorrun.sh) and manual (through motorForward.sh and motorReverse.sh) operation of the hardware was used to obtain the video recordings. In our field set-up, fully automated operation was hindered due to birds sitting on and tampering with the timing belt. This problem often led to the timing belt slipping out of the support pulleys, making scheduled automated use of the hardware difficult. Protecting the timing belt, through a long pipe or other enclosure above the camera track, is recommended for more automatable and error-free operation of this hardware.

These two video types (moving and stationary) captured from this camera system represent novel data collection on crop lodging and movement in a field setting. This camera system enabled the imaging of novel properties of plant movement that will be used to identify new breeding targets for increased wind resistance in cereal crops. Furthermore, this automatable camera system is readily adapted to other field dimensions, crops, and sensor systems for the procurement of high throughput phenotypic data in agricultural research.

Figures

Figure 1. View down the camera track and various components. 1) Support pulley holding timing belt 2) 3” C-clamps holding L bracket 3) Mounted 360 FLY camera on trolley 4) Support roller for timing belt

Figure 2. Magnitude of Acceleration (A), Gyration (B), and Heading Change (C) in a forward camera track run taken on 19-Jul 2017. The frequency of measurement was higher for the 360FLY accelerometer than the gyrometer or magnetometer.

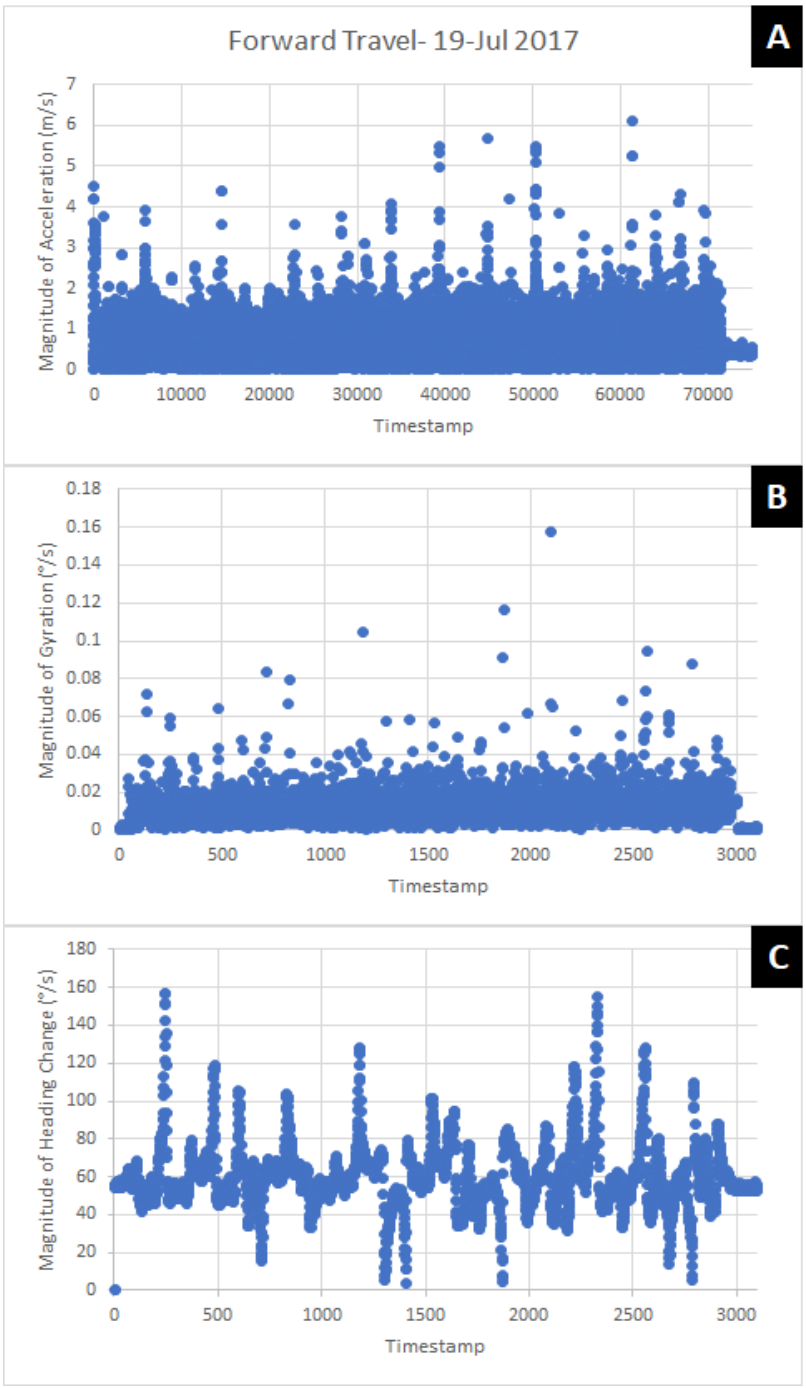

Figure 3. Imaging crop lodging. Still frames from video taken using a 360FLY camera mounted to the trolley on the camera track. Lodging can be differentiated from these images, with (A) taken before a lodging event and (B) taken after a lodging event. The orange box highlights three rows with lodging, while the green box highlights 3 rows without lodging.

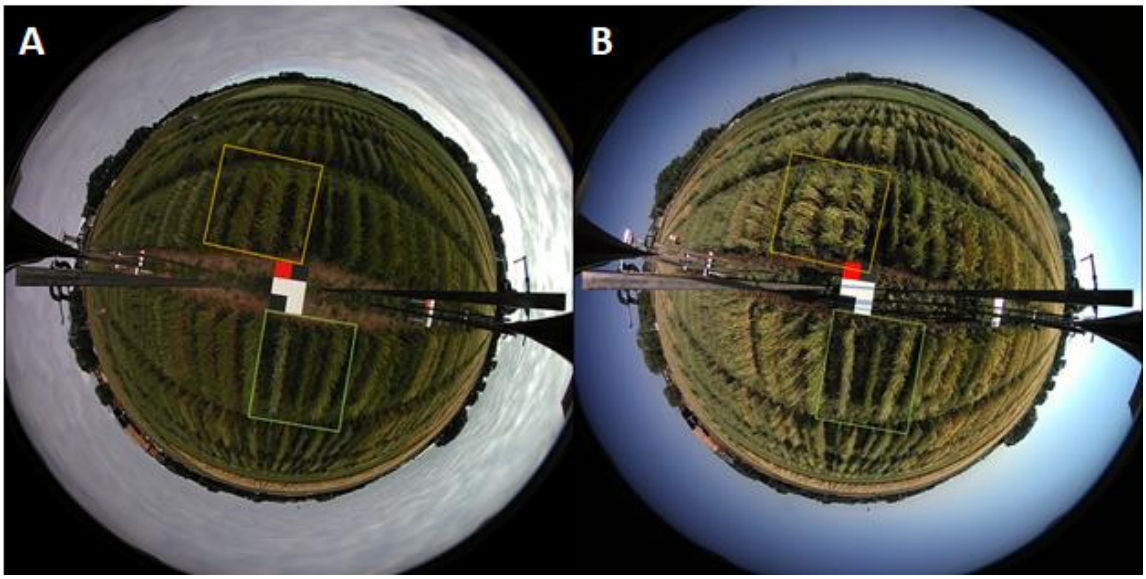

Figure 4. Oscillograms of wave movement through grain rows based on the mean red pixel value for each frame, normalized to the red QR square over one video (07_10_17, planting date 1). Differences in the frequency, amplitude of grain wave movements are detectable between the two oat varieties from the 360FLY camera mounted to this hardware.

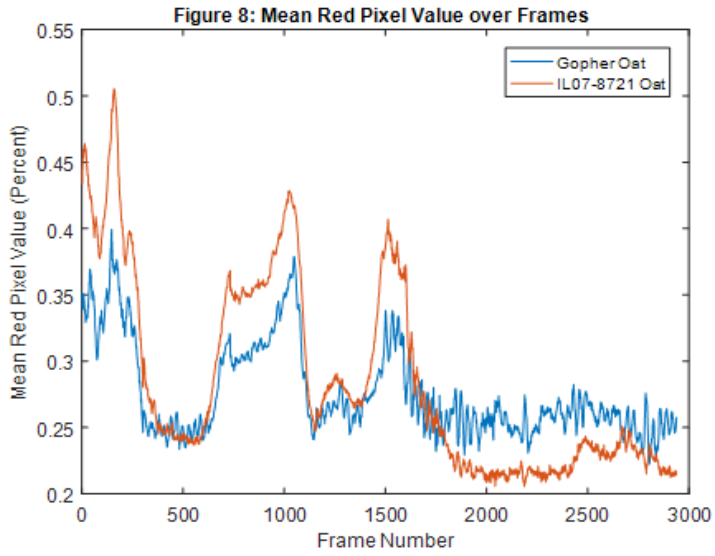

Chapter 3:

Quantifying cereal crop movement through hemispherical video analysis of agricultural plots[*]

Alexander Q. Susko[1], Peter Marchetto[2], D. Jo Heuschele[2], and Kevin P. Smith[2]

[1] University of Minnesota Department of Agronomy and Plant Genetics, 411 Borlaug Hall, 1991 Upper Buford Circle, St. Paul, MN 55108

[2] University of Minnesota Department of Bioproducts and Biosystems Engineering, 1390 Eckles Ave., St. Paul, MN 55108

[*] AQS conceived of the research in this chapter, organized construction of the camera system, performed construction of the camera system, developed the video analyses, and wrote the manuscript. PM and DJH provided substantial manuscript edits as well as technical advice, while KPS served as principal investigator. A version of this chapter is published in the journal Plant Methods:

Susko, A.Q., Marchetto, P., Heuschele, D.J. and Smith, K.P., 2019. Quantifying cereal crop movement through hemispherical video analysis of agricultural plots. Plant methods, 15(1), p.55, https://doi.org/10.1186/s13007-019-0437-5

Introduction

Prior to the failure (lodging) of plant stems under wind stress, an entire plant experiences movement. This movement occurs in plants of all sizes and taxa; it is dependent on plant structural traits and wind conditions, which together govern the failure velocity at which a plant stem will fail in the wind (De Langre, 2008; Gardiner et al, 2016). Increasing stem resistance to wind is of critical interest to breeders of cereal crops such as oat, barley, and wheat, where development of lodging resistant varieties is a continuous challenge. Lodging in cereals is a major contributor to yield loss, which can be as severe as 31--37% when stems are lodged at a 45 degree angle or greater (Pendleton, 1954; Weibel and Pendleton, 1964). While most strategies for improving lodging resistance focus on scoring lodging after a storm or measuring physiological parameters such as stem strength, less is known about how plants interact with the wind in real time, nor do methods exist to systematically quantify plant movement in agronomic or breeding experiments.

Plant movement has been studied theoretically from the scale of individual plants to entire canopies (De Langre, 2008; Gardiner et al, 2016). At a basic glance, plant movement is governed by the spring constant (stiffness, K) of the stem (Flesch and Grant, 1991). In the simplest representation, the natural frequency (ω_n) at which a plant stem moves is governed by the ratio of stem stiffness to mass per unit length (m_p) of the stem (Flesch and Grant, 1991) (Eq. 1):

$$\omega_n = \sqrt{\frac{K}{m_p}}$$

From Eq. 1, an increase in the stiffness of the stem, holding m_p constant, will increase the natural frequency of the plant oscillations (movement). If the intermittent gusts across a cereal canopy encounter plants whose ω_n matches that of the gusts, the movement of the plant will not dissipate and will likely be amplified. If the vibration is sustained long enough to cross a failure threshold, the plants will lodge. However, additional physical parameters and the wind conditions all interact in reality to make plant movement a function of various physical properties at any given time point. These can include the structural (ζ_s) and aerodynamic (ζ_a) damping coefficients of the plant, stem acceleration ($\ddot{\theta}$), stem velocity ($\dot{\theta}$), stem angle (θ), and the wind moment (force of wind multiplied by area exposed, M_w). These values can be used to estimate the ω_n at a given moment by the equation (Flesch and Grant, 1991) (Eq. 2):

$$\omega_n = \sqrt{\frac{K\left(\ddot{\theta} + 2\omega_n[\zeta_s + \zeta_a]\dot{\theta} + {\omega_n}^2\theta\right)}{M_w}}$$

An increase in plant natural frequency should increase the wind velocity required to induce failure and result in greater lodging resistance, because stem oscillations would dissipate after being excited by gusts that occur at a lesser frequency (Berry et al, 2006). Realistically however, any change in physiology (ie mass per unit length, structural loading) or environment (ie wind moment) will affect the resonant frequency and thereby change the failure velocity (Baker, 1995; Berry et al, 2006) (Eq. 1,2). These expectations have been used to derive detailed equations relating plant movement and aerodynamic

forces, which consider the natural frequency of plant stems as a component along with other physiological traits to model the failure of plants under wind stress (Baker, 1995; Moore and Maguire, 2004; De Langre, 2008). In agronomic crops, plant movement has been factored into models that describe theoretical failure velocities in wheat, barley, and maize for given certain physiological parameters (Flesch and Grant, 1992; Berry et al, 2003; Berry et al, 2006). However, the physiological factors incorporated into these models are not easy to quantify quickly, nor is there a large scale validation method for models of plant movement that could be employed across variable germplasm. Thus, quantifying the phenomenon of plant movement relatively quickly that is scalable to large field experiments could lead to optimal phenotypic combinations for breeders to target that increase the wind resistance of cereal crops.

Empirical studies on plant-wind interaction employ a variety of technologies to quantify movement in plant systems primarily developing or validating theoretical models on a small scale. A large portion of experimental research on plant movement has focused on understanding tree sway to minimize timber losses from storms (Gardiner et al, 2016). The earliest research on tree movement involved using a stopwatch to calculate a tree sway period. The study reported that as tree height increased, tree sway frequency decreased (Sugden, 1962). Digital data on plant movement from a micrologger (accelerometer, gyrometer) data acquisition system further allowed theoretical assumptions of plant movement to be refined on the individual plant level in maize by the late 1980s (Flesch and Grant, 1991). The advent of digital video cameras have enabled new quantifications of plant movement, such as adapting the technique of Particle Image

Velocimetry (PIV) to light reflected off of an alfalfa canopy to map turbulent air flows over the crop canopy (Py et al, 2005). Interactions between individual plants have also been quantified through video analysis, specifically by tracking changes in color within a given region of a video as stems oscillate and collide with each one another (Doare et al, 2004). Color changes within defined regions of digital video, analyzed as time-varying signals, can thus be a non-invasive measure of plant movement.

Treating plant natural frequency (ω_n) and the amount of movement (amplitude) at that frequency as plant phenotypes could enable genetic studies and breeding based on a crops's real-time response to field wind stress. Implementing a method to quantify phenotypes of plant movement at high throughput in experimental designs such as the randomized complete block (RCB) pose another use for relating physiology, movement, and lodging: to better optimize physical trait combinations that are desirable in theory but in practice will require high statistical power to validate under variable field environments. While no systematic approaches exist for quantifying plant movement for purposes of improving crop lodging resistance from video, many studies have devised methods to quantify crop lodging from image and spectral data. Recent lodging phenotyping efforts include analyzing lodging in the visible spectrum from unmanned aerial vehicle (UAV) images in wheat , rice , and maize (Chapman et al, 2014; Chu et al, 2017; Yang et al, 2017). Additionally, lodging has been quantified in the field using merged thermal and infrared images, as well as through plant height differences detected through LIDAR (Madec et al, 2017; Lie et al, 2018). UAV systems are not ideal for capturing video data, especially when data on plant movement is desired under high wind

or stormy conditions. Ground based, automatable camera systems are more amenable to capturing video under inclement weather, and 360 degree field of view video cameras are capable of imaging a full hemisphere per frame (Chapter 3). The use of a 360 video camera alleviates the need for multiple cameras to capture replicated plots and for synchronization of separate videos at exact moments in time, while remaining close enough to the canopy level to capture small differences in movement. Though hemispherical video can capture a large field of view, the analysis and demarcation of individual plots is more trigonometrically rigorous and requires novel analysis protocols. For purposes of measuring plant movement, the two can be combined in a way that any field design can serve as input to guide image analysis and data organization.

In this study, we develop novel video analyses and demonstrate that can be used to quantify plant movement as a phenotype in the field from a stationary, 360 degree field of view camera system for purposes of understanding cereal crop lodging resistance under field wind stress. The context of this method focuses on individual plant rows as opposed to canopy dynamics of uniform fields, with the idea that this method could be generalized to an applied breeding scheme. The method presented quantifies the natural frequency (ω_n) of movement and amplitude of single, homogenous rows of cereal cultivars without mechanical interference. Our method accomplishes this primary objective by 1) identifying plots from a predefined field design to systematize data analysis, 2) employing signal processing techniques to analyze plant movement as changes in the RGB color space, and 3) demonstrating the method's capabilities by

quantifying plant movement in the field for 16 cereal varieties planted in a randomized complete block (RCB) design.

Materials and Methods

Camera, field, and naming conventions.

Camera System. We designed and constructed an automatable camera track system to collect hemispherical video of single row research plots (Chapter 3). Briefly, the camera track system spanned 39.6m at 2.7m above ground level and deployed a 360fly 4k hemispherical video camera (360fly, Inc.). The camera tracking was repurposed industrial curtain tracking (AmCraft Manufacturing, Inc.) mounted on 3.65m, 5.08x5.08cm steel posts set 61cm into concrete form tubes below the field surface. Movement of the camera along the track was accomplished by attaching the camera to a custom trolley linked to by a timing belt to a solar powered motor. Control of the motor was automated using a Raspberry Pi 3 Linux computer (Raspberry Pi Foundation). An example photo of the camera track is shown (Figure 1). Importantly, 91x61cm painted panels (panels) with a unique black, white, and red block design were centered underneath the camera track at regular intervals with the red square always oriented in the northwestern corner of the installed panel (Figure 2A). The unique black and white block design served to uniquely mark the field location at each panel, while the red square served to orient the camera and apply necessary corrections to the geometric transformation of the 2D field into a 3D, hemispherical image.

Camera Specifications. The 360fly 4k hemispherical video camera (referred to as 360 camera) recorded plant movement in the field. The 360 camera contained an 8 Elements Glass Ultra Fisheye Lens with an aperture of F2.5, effective focal length of 0.88mm, and a minimum focus distance of 30cm. The horizontal field of view was 360°, while the vertical field of view was 240°. Brightness was set to full brightness, while the aperture and contrast settings were set in the middle values for each. Videos were recorded at 24 frames per second with a per frame image size of 2880 x 2880 pixels. The 360fly ios app (V 2.0.0) was used to maintain consistent settings and initiate camera recordings while the camera was mounted on the track system, and the 360fly Director (V 0.10.4.0) software for Microsoft Windows 10 was used to download the videos from the camera and export them into .mp4 format.

Field Design. The camera system imaged a randomized complete block (RCB) design. The design contained four cultivars of four different cereal grains (Table 1) for a total of 16 cultivars. Cereal cultivars were planted in single row plots (hereafter referred to as plots) of 3.04m in length with 30cm spacing between rows with a north-south orientation. A row of winter wheat separated each cereal plot used in the study. Each cultivar was replicated 8 times, with four replicates sufficiently close to the camera for analysis. Furthermore, this design was planted at four different planting dates (25 Apr, 5 May, 15 May, and 26 May 2017) in adjacent regions of the field. The camera system bisected the center of each planting date of the experimental design between the 4th and 5th replication, allowing video recording of different cultivars and growth stages at each video recording date. Average wind speed, gust, and direction data were obtained for

each video date from the Minnesota DNR Mesonet station located on the research plots of the Minnesota Agricultural Experiment Station in St. Paul, MN (Table 2) (University of Minnesota DNR, 2017).

Pre-analysis procedures. Prior to identifying plot regions within the 360 video and subsequent signal processing, we defined the field coordinate system and plot naming conventions. This allowed us to generalize the matlab scripts in the pipeline across different parts of the field RCB as indicated by the unique panels. The lodging RCB was numbered in a serpentine pattern beginning in the northeastern corner of the field, moving to the west, and then back to the east in the next replicate at each panel (see Additional file 3 for an illustration). We organized the plot naming and field coordinates according to this serpentine order. At each camera stopping point over a panel, 4 blocks were in view that contained between 22 and 28 plots in total. We created two files associated with each panel, one for plot names and the other for plot coordinates. For our field layout, the plot name files (Additional files 4-7) were 22-28 lines depending on the panel it was associated with and contained the cultivar names associated with the serpentine numbered plots, beginning in the northeast corner of the analyzable field region. Each plot was named: *Cultivar_Crop_PlantingDateRep* (ie Gopher_oat_4A). This allowed for regular expressions to search the names and append relevant plot data to the signal output from the videos. The plot coordinates file (Additional files 8-11) contained the same number of rows as the plot names file for a given panel. The columns in the coordinates files contained the x, y, and z coordinates for each corner of a plot to represent the top of the canopy in 3D space. The first column contained plant heights (z

values) for each plot. The remaining 8 columns contained the cartesian (x,y values) coordinates for each corner of a plot (SW, SE, NW, NE), with 2 columns (containing x,y distances) for each corner of the plot. These plot coordinates are hand-defined by the researcher and utilized in subsequent transformations to demarcate regions in the hemispherical image. We present distances in feet within the supplemental files given our field planting equipment, but ultimately these units are arbitrary. Plot coordinates were expressed from the center of the panel, with the x axis denoting the camera track path, and the y axis perpendicular to the camera track at the panel center point (origin). In our field setup, points north of the x axis had positive y values while those south had negative y values, and points east of the y axis had positive x values while those west had negative x values.

Video naming protocol: We set a standard file naming convention for videos (.mp4 files) so that the date information could be obtained throughout the video analysis and signal processing pipelines. We used the following file naming convention for videos: FLYmm_dd_yy_pn.mp4, with n being the panel number imaged in that video.

Table 1. Chapter 3 List of Abbreviations.

Abbreviation	Definition
C_n	Percent of image size along image y axis from image center to the nth point
dB	Decibel
D_n	Distance to the nth point as mapped on the image (as a percentage of image size)
fps	Frames per second
GCP	Ground Control Point
Hz	Hertz
m_p	Stem mass
M_w	Wind moment (height*force)
n	The nth coordinate point in a field design (ft)
RCB	Randomized Complete Block
R_n	Percent of image size along image x axis from image center to the nth point
SW_{xn}, SW'_{xn}	Field design x cartesian coordinates to the nth southwest corner, field design x cartesian coordinates to rotated nth southwest corner (ft)
SW_{yn}, SW'_{yn}	Field design y cartesian coordinates to the nth southwest corner, field design y cartesian coordinates to rotated nth southwest corner (ft)
UAV	Unmanned Aerial Vehicle
x_n	Field design x cartesian coordinates to the nth point (ft)
y_n	Field design y cartesian coordinates to the nth point (ft)
z_n	Field design z coordinates from the height of the canopy at the nth point to the height of the camera (ft)
ζ_a	Aerodynamic loading coefficient of plant stem
ζ_s	Structural loading coefficient of plant stem
θ	Stem angle (°)
$\dot{\theta}$	Stem velocity
$\ddot{\theta}$	Stem acceleration
Θ_n	Longitude angle of the nth point (°)
Θ_{off}	Rotation angle of field design relative to camera axes
φ_n	Latitude angle of the nth point (°)
ω_n	Natural frequency of a plant stem or cultivar row (Hz)

Table 2. Chapter 3 Additional Files. Available online (Susko, 2018b)

File Name	Ext	Data Title	Data Description
Additional file 1	.m	plotfinder_published	Matlab script to demarcate user-defined regions of a field from hemispherical video
Additional file 2	.mp4	FLY07_12_17_p2	MP4 video file from 360Fly 4k camera, taken 12 Jul 2017 at planting date 2. Used as sample video for published scripts
Additional file 3	.xls	fieldmap_readme	Field design at the panel in planting date 2. Corresponds to analyzable plots in Additional file 2
Additional file 4	.txt	fieldPlotnames7	Field plot names file for 25 Apr 2017 planting date
Additional file 5	.txt	fieldPlotnames5	Field plot names file for 5 May 2017 planting date
Additional file 6	.txt	fieldPlotnames3	Field plot names file for 15 May 2017 planting date
Additional file 7	.txt	fieldPlotnames1	Field plot names file for 25 May 2017 planting date
Additional file 8	.csv	fieldCoordinates7	Field Coordinates file for 25 Apr 2017 planting date
Additional file 9	.csv	fieldCoordinates5	Field Coordinates file for 5 May 2017 planting date
Additional file 10	.csv	fieldCoordinates3	Field Coordinates file for 15 May 2017 planting date
Additional file 11	.csv	fieldCoordinates1	Field Coordinates file for 25 May 2017 planting date
Additional file 12	.m	FLY07_12_17_p2	Matlab script to obtain normalized waveforms from sample video (Additional file 2)

Additional file 13	.m	bandpassParse_p2	Matlab script to filter and parse waveforms from Additional file 12
Additional file 14	.r	stationary_organization_published	R script to organize the frequency, amplitude, and plot data from Additional file 13 into an statistically analyzable format
Additional file 15	.r	stationary_analysis_published	R script to analyze the data from Additional file 14

Plotfinder Analysis to demarcate agricultural plots in a 360 image.

This portion of the methods section details the demarcation of agricultural plots from images taken using the 360 camera along with researcher defined field coordinates and plot names. The text below explains the processes coded in Additional file 1. Analysis was written in Matlab v2016b, and must be executed in Matlab v2016b or later.

Section 1.1: Locate panel in the 360 video still frame (image). The panel, identified by the red square in the northwest corner of each panel, provides a reference upon which all subsequent transformations of the field design are based. Masking the red square in the northwest corner of the panel provides a reference point for all measurements to conduct this transformation. The red square is masked by applying a threshold (with threshold values determined using the Matlab color thresholder application) to the 360 image in RGB color space (R: 251-255, G: 0-159, B: 0-255). Depending on ambient lighting conditions, these threshold values may need to be changed for individual videos to completely identify the red square. To ensure that the masked object using the threshold

is the red square on the panel, square structuring elements of 4 pixels in size helped define the right angle edges of the red square, while all masked objects whose areas were less than 5000 pixels (the area of the true red square is approximately 6000 pixels in the center of the image) were then unmasked, leaving only a masked image of the red square. While not experienced in this experiment, sunlight conditions that create an excessively saturated image might necessitate altering the minimum red square size or ensuring that the red square is adjacent to black panels instead of white to better define the location of the red square. With the red square masked from the original image, the left-most corner of the square serves as the reference point for all subsequent measurement (Figure 2B). The leftmost corner of the red square is identified by finding the minimum column index of the image array where a non-zero element is present. Knowing the column index for the leftmost corner, the row index is found where the minimum row in the minimum column index is not zero. The column and row indices for the left most corner are then retained in memory as the script advances.

Section 1.2: Identify direction and calculate angle of rotation. Estimating the direction and angle of rotation of the panel within the image allows the field design to be rotated to the correct orientation in the image. The column index of the leftmost corner of the red square is used to determine which direction the panel is facing in relative terms within the 360 image, as the camera axes might not be in line with the field axes when the camera is installed on the track system. The direction of rotation is determined by obtaining the RGB color values of the 40 pixels above and below the leftmost corner column (Figure

2B). A mean red color value of greater than 245 will indicate the presence of a white square, while lower values will indicate that the ground is in view. Thus if the mean value of the indices below the left most column is greater than 245 while the mean above the left most column is less than 245, the panel is rotated northeastward relative to the camera axes (Figure 2A-B). Once the direction of rotation is known, the degrees rotated in that direction can be calculated from the remaining indices of the masked red square. In Figure 2C representing a northeastern rotation of the panel in the image, the angle between the camera x axis and the field x axis (Θ_{off}) is calculated using the relationship (Eq. 5a)

$$\Theta_{off} = -90 - \text{tand}^{-1}\frac{\overline{AB}}{\overline{BC}}$$

While in Figure 2D representing a southwestern rotation (as well as the northwest and southeastern rotations) of the panel in the image, the same angle is calculated (Eq. 5b)

$$\Theta_{off} = \text{tand}^{-1}\frac{\overline{AB}}{\overline{BC}}$$

With the points A,B,C representing the same triangulation (in row indices for AB and column indices for BC) of the panel offset angle in the image. The leftmost corner of the red square will not always represent the same point on the physical panel (Figure 2C-D). Thus, the script will identify the indices of the relevant corner given a certain rotation condition.

Section 1.3: Identify the panel in frame and incorporate field design. The researcher assigns the panel in frame a number that corresponds to those in the field coordinates or plot names files so that the correct versions of these files are used in subsequent transformations. The panel is identified based on user input at line 14 of the plotfinder script (Additional file 1). Once the panel is known, the corresponding plot names and plot coordinates files are read into the script from the working directory.

Section 1.4: Rotate field design, transform field design to spherical coordinates. This section describes the rotation of the field design according to the direction of rotation and Θ_{off} value calculated in section 1.2. Following this rotation, the rotated 2D plot coordinates are transformed into spherical coordinates for use in identifying their location on a hemisphere. Each set of field (x,y) coordinates are extracted from the file into an *n x 2* matrix, which is then transposed to a *2 x n* matrix. All points in the *2 x n* matrix are rotated clockwise around the origin by multiplying with a *2 x 2* rotation matrix. In the case of a northeastern rotation of the panel (Figure 2C) and a *2 x n* matrix representing the x and y coordinates of the southwestern corner points of the plots, the calculation is (Eq. 4a):

$$\begin{bmatrix} \text{cosd}\,\Theta_{off} & \text{sind}\,\Theta_{off} \\ -\text{sind}\,\Theta_{off} & \text{cosd}\,\Theta_{off} \end{bmatrix} * \begin{bmatrix} SW_{y1} & SW_{y2} & SW_{yn}\ldots \\ SW_{x1} & SW_{x2} & SW_{xn}\ldots \end{bmatrix} = \begin{bmatrix} SW'_{y1} & SW'_{y2} & SW'_{yn}\ldots \\ SW'_{x1} & SW'_{x2} & SW'_{xn}\ldots \end{bmatrix}$$

For a southwestern rotation of the panel (Figure 2D) in the image, 180 degrees is added to theta offset in the rotation matrix (Eq. 4b):

$$\begin{bmatrix} \text{cosd}(\Theta_{off} + 180) & \text{sind}(\Theta_{off} + 180) \\ -\text{sind}(\Theta_{off} + 180) & \text{cosd}(\Theta_{off} + 180) \end{bmatrix} * \begin{bmatrix} SW_{y1} & SW_{y2} & SW_{yn} \ldots \\ SW_{x1} & SW_{x2} & SW_{xn} \ldots \end{bmatrix} = \begin{bmatrix} SW'_{y1} & SW'_{y2} & SW'_{yn} \ldots \\ SW'_{x1} & SW'_{x2} & SW'_{xn} \ldots \end{bmatrix}$$

The rotation matrix for a northwestern rotation is the same as in Eq. 4a, while a southeastern rotation will have 90 degrees added to Θ_{off} instead of the 180 degrees as in Eq. 4b. In addition to adding 90 or 180 degrees to Θ_{off}, it is necessary to flip the sign of all field coordinate values in a southeastern or southwestern rotation condition. This is done by element wise multiplication of -1 to all values within the coordinate matrices prior to multiplication by the rotation matrix.

Following rotation of the field coordinates in relation to the camera axes, the rotated field coordinates are transformed from the Cartesian (x,y) to spherical (latitude, longitude) coordinates. This is accomplished by two separate triangulations in three dimensional space (Figure 3). The latitude angle (φ_n) for a given coordinate *n* is calculated by taking the inverse sine of the ratio of plant height to the distance from the camera height to the *nth* point on the field (Eq. 5):

$$\varphi_n = \text{sind}^{-1} \frac{z_n}{\sqrt{x'_n + y'_n + z_n}}$$

With the value of φ_n ranging from 0 to 90 degrees. The longitude angle (Θ_n) for a given coordinate is calculated by taking the inverse 4-quadrant tangent of the ratio of y to x distance to the rotated field coordinate (Eq. 6):

$$\Theta_n = \text{tan2d}^{-1} \frac{y'_n}{x'_n}$$

With the value of Θ_n ranging from -180 to 180 degrees. The *nth* plot coordinate is then represented in a new *n x 2* matrix containing the latitude and longitude values for each coordinate in the rotated hemispherical image. These values are stored in plot order corresponding to that given in the plot coordinates and plot names files.

Section 1.5: Obtain indexed pixel values as a function of spherical coordinates for each field design coordinate. Once plot coordinates are transformed from Cartesian to spherical coordinates, the latitude for a given point can then be represented in terms of the distance from the center of the image as a percentage of total pixels. This assumes that the image was taken directly above the panel so that the image center (pole) and the panel center are in alignment. The relationship between degrees latitude and number of pixels is non-linear: as latitudinal coordinates approach the equator (0 degrees), fewer pixels are required to represent the change in latitude. Given the 240° field of view captured by the 360Fly 4K camera, the edge of the hemisphere does not represent the equator. Instead, the radius from the image center to the equator is assumed to be located at the 1440th row for frames taken at a 2880x2880 pixel resolution. Due to the field of view and other unknowns regarding the lens optics, we empirically determined the relationship between degrees latitude and the percentage of pixels in the image along the radius at the 1440th row. The percent distance (D_n) in an image is thus a quadratic function of a point's latitude (Eq. 7)

$$D_n = {\varphi_n}^2 * 10^{-7} - \varphi_n * 5^{-3} + 0.3609$$

As the *1 x n* matrix of D_n values represents the hypotenuse out to a given point based on the n_{th} point's latitude and longitude, this distance D_n for a point is used to estimate the distance (in percent of total indices) along the x and y axes within the image. The percentage of the image in terms of rows (R_n) is calculated as (Eq. 8a).

$$R_n = \frac{D_n * \text{sind}\,\theta_n}{sind(90)}$$

And the percentage of the image in terms of columns (C_n) is calculated as (Eq. 8b).

$$C_n = \sqrt{{D_n}^2 - {R_n}^2}$$

The resulting *1 x n* matrices of R_n and C_n values are concatenated into a *2 x n* matrix of the same dimensions as the initial coordinate input for a given set of points. Expressing distances as a percent of the image size from the image center (radius), they represent the percent distance in rows and columns to a given point from the field design on the hemispherical image.

Section 1.6: Create correction matrix for points in field design for applying correct index sign. Though the row and column indices are expressed as percentages of the radius of the hemispherical image, the calculations in section 1.5 do not assign the correct sign to these indices to indicate their location in regards to the image center. The R_n and C_n values calculated above are expressed in percent distance from the image center without the correct sign indicating where the points fall with respect to the image center. Longitude angles for the *nth* point are used to assign the appropriate sign to the R_n and C_n values. For rows, if the longitude angle for the *nth* point is between 0 and 180, R_n will be

negative while if the longitude angle is between 0 and -180, R_n will be positive. For columns, if the longitude angle for the n_{th} point is between 90 and -90, C_n will be positive while if the longitude angle is between 90 and 180 or -180 and -90, C_n will be negative. The correction matrix will have dimensions of *n x 2*, with the first column containing the row distance as a percentage of image size, the second column containing the column distance as a percentage of image size, and *n* rows for the number of points in the field design.

Section 1.7: Apply the correction matrix to the index values. The correction matrix indicating the correct sign for the row, column index percentages is applied, with the index percentages converted to actual pixel indices based on the image size, and then added to the image center row, column index to obtain the final transformation of the field coordinates to their location in the hemispherical image. The correction matrix for each coordinate is multiplied element-wise by the matrix of row and column distance percentages (Eq. 9)

$$\begin{bmatrix} -1 & 1 \\ 1 & -1 \\ \vdots & \vdots \end{bmatrix} .* \begin{bmatrix} R_1 & C_1 \\ R_2 & C_2 \\ R_n & C_n \end{bmatrix} = \begin{bmatrix} -R_1 & C_1 \\ R_2 & -C_2 \\ R_n & C_n \end{bmatrix}$$

This resulting matrix contains the R_n and C_n values whose signs reflect the correct orientation with respect to the image center. The R_n and C_n distance percentages are then multiplied element-wise by the image size (2880 pixels) express these values as image pixels. Since these values now represent the number of pixels to the *nth* point along the image y and x axes from the center of the image, half the value of the image size (1440 pixels) is added to every element within this matrix. The resulting array contains the

indexed pixel value for the row and column in the image where a plot coordinate is located.

Section 1.8: Crop plots based on these rotated coordinates, export images and cropping functions. With each of the four corners of a plot represented in terms of indexed rows and columns pixels in the image, demarcation of the original image can begin. Each row in the resulting pixel arrays for plot corners (NW,NE,SE,SW) represents a unique plot in the field design that corresponds with the order in the original plot coordinates and plot names files. The *nth* row of each of the four arrays containing row and column pixels are used to demarcate a polygon cropping region on the original image with the plot name appended to the filename according to the *nth* row of the plot names file. The script will produce the same number of images as the number of rows in the input plot coordinates and plot names files. Additionally, a cropping function is generated by the script that can demarcate the plot region across frames in a video. Examples of the resulting cropped plots in different rotation conditions and region of interest sizes are shown (Figure 4A-D). The correctness of the plot demarcation can be visually assessed by the user though comparing the cropped image of a plot with the entire field captured in one of the uncropped frames.

Plotfinder Accuracy. We assessed the plotfinder accuracy by comparing the differences in feet on the ground generated by automatic angle detection and manual angle measurement. We ran the still frames from each video through the plot finder script to

calculate Θ_{off} and obtain the rotated coordinates for each corner of the demarcated 929cm^2 area. We then manually calculated the angle of the red square by measuring the distance manually using the line tool in Powerpoint (Office 365), which gives the height and width that the line travels in the image and used those values to calculate Θ_{off} manually (Eq. 5A-B). This value of Θ_{off} was then used to recalculate the x and y coordinates of each plot corner. The average x,y values of the outer and inner reps were then grouped and averaged, with the x and y differences calculated before a final averaging of the x and y differences for the outer and inner reps.

To evaluate the automatic plotfinder script demarcation error on quantifying color changes indicative of plant movement, we manually outlined cropping function demarcating 929cm^2 regions (as in Figures 4C-D) of the 98 plots at each of the 5 video dates using the image segmenter app built into Matlab v2016b. We used this manual demarcation to compare with the automatically generated cropping function using the plotfinder script and plot names, plot coordinates files that denoted 929cm2 regions in the field. Both the manual and automatically generated cropping functions were applied over each frame to calculate the average normalized red color value in the demarcated region. The average normalized red values from the manual and automatically generated cropping functions were then correlated over all frames and planting dates for each video date. A linear model with one term indicating whether the position of the rep (inner or outer) was used to explain the correlation for each video date (across planting dates, plots). An LSD test with Bonferroni correction in the R package agricolae was then used

to assess whether the differences in mean correlation coefficients between the inner and outer reps was significant.

Movement Analysis using the plotfinder generated cropping functions: The second half of the method first uses two matlab scripts (Additional file 12 and Additional file 13) written in MATLAB v2016b followed by two R scripts (Additional file 14, Additional file 15) written in R v3.4.1.

Section 2.1: Obtaining raw waveform data on plant movement. We apply our plot demarcation method to a novel strategy for quantifying plant row canopy movement by analyzing the change in normalized red color values averaged within the demarcated plots of the RGB 360 4k video. While reflectance of plant tissue is low in the red band of visible light due to absorption by chlorophyll, the soil between rows reflects wavelengths in this part of the visible spectrum back to the camera (Huete, 1988). Since the stem oscillations are captured against ground surfaces or large gaps in foliage in this field layout, the red channel of the RGB 360 4k video should be best suited to detecting movement of a cereal row canopy within a fixed region across all frames. These specific regions correspond to a 929cm^2 region at the height of the plant canopy with one edge along the center of the row. These functions were called by a script that was unique to each panel (Additional file 12). This script incorporated the plotfinder generated cropping functions specified for each plot, and calculated the average red value at each frame for every plot. The average red value for each plot was then normalized to the red square on the panel at that frame in the video, so that color values could be compared

across different lighting conditions within a video and across videos. Each waveform script produced a resulting array with the number of rows equaling the number of frames in the video, and the number of columns equaling the number of plots. The arrays for each video are exported as a text file with the same file name as the video analyzed. These steps are then repeated for all the videos. This enables collection of the waveforms in plant row canopies to be quantified and expressed in normalized red color units, as shown in Figure 5A.

Section 2.2: Organizing raw waveform data on plant movement for analysis. We quantify the amount of canopy movement within each of these demarcated regions of the plot using a time domain signal processing approach (Additional file 13). First, we utilized a bandpass filter on each plot's waveform to filter out low frequency changes in red values due to light changes from passing clouds during a video. The bandpass filter centers each waveform at 0, enabling comparisons of canopy movement across different lighting conditions (within and among videos) and across different cereal cultivars, which have different mean red color values. The equiripple bandpass filter implemented in the MATLAB script contained the following filtering parameters as expressed in percentage of analyzable frequencies (0-12 Hz in this case given the 24 fps recording rate). Filtering began with an Fstop1 of 3 %, Fpass1 of 4%, and ended with an Fpass2 of 40%, Fstop2 of 50% to eliminate high frequency (>0.5 Hz) noise due to camera vibrations induced by high winds. The attenuation of the passed versus filtered signal was 100dB, while the Ap

value within the passed signal was 5dB. This filter was applied to each column in input text file of raw plot waveforms from a video.

Following bandpass filtering of each waveform, we obtained the amplitude (in normalized red color units) and time location (in frames) of each local maxima of the waveform color signal with at least a 0.5% red change prominence. Next, we calculated the distance (in frames) between peaks, skipping the first peak. A visualization of the peak identification process is presented in Figure 5B. These distances were used to estimate the frequency between peaks, as the distance in frames was divided by the frame rate (24 fps). Finally, we summed the total (absolute) area under the curve that lies between peaks to estimate the amplitude change in the waveform. The data was then written to a text file for each plot containing one column listing the frequency of a given cycle, and the absolute area encompassed by that cycle. For each video, a subdirectory was written that contained the individual files for each plot.

This frequency and area data was run through an R script (Additional file 14) to organize it for analysis. The user navigates to the directory containing all video dates for one panel. The r script then goes through each subdirectory to read in the individual plot files containing the frequency and area data. Information including cultivar, replicate, video date, and planting date are obtained from the standard naming protocol outlined above. For each file, the pass range (between 0.5 Hz and 4.9 Hz) is used to calculate a mean, median, and standard deviation of the frequency distribution for each plot (Figure 5C). The areas in the plot file are then binned according to their corresponding frequencies into 0.2 Hz bins from 0.5 to 4.7 Hz. Each plot file is condensed to one line

containing these values, with the resulting dataframe for one video date containing a row for each plot. A position vector indicating whether a plot is near or far from the camera track is added last, with the numbers corresponding to the file alphanumeric order in the subdirectories as opposed to how they are physically laid out in the serpentine pattern. Finally, all of the dataframes for each video date are concatenated into a single dataframe for each panel. Dataframes for all panels are then concatenated into a final dataframe for the statistical analysis of plant movement.

Section 2.3: Statistical analysis of plant row movement.

Plant row movement was modeled using the components of a randomized complete block design (Additional file 15). We analyzed two response variables of plant movement: the mean frequency (ω_n) of the peak distribution for each row in a video date, as well as the total (absolute) area between peaks in the 1.1-1.3 Hz frequency band. Each response variable was modeled using the following linear model (Eq. 10):

$$y_{ijkl} = \beta_0 1 + \beta_1 x_{i1} + \beta_2 x_{i2} + \beta_3 x_{i(j)3} + \beta_4 (x_{i1} * x_{i2})_k + \beta_5 \left(x_{i1} * x_{i(j)3}\right)_l + \varepsilon_{ijkl}$$

With *ß1* representing the cultivar effect, *ß2* the planting date effect, *ß3* the effect of a replicate in the *jth* position (inner or outer) nested within the *ith* cultivar, *ß4* the cultivar by planting date interaction effect, and *ß5* the cultivar by *jth* position nested within the *ith* planting date interaction effect. The ANOVA for estimating the significance of each effect was conducted using the expected mean squares and F values presented in the table below (Table 3).

Table 3. Expected Mean Squares and F test calculations for parameters in Eq. 10.

Source of Variation	**Row Effect**	**Expected Mean Squares**	**F value**
Cultivar	K^2_C	$\sigma^2_e + \sigma^2_{CxP(PD)} + K^2_C$	$(\sigma^2_{CxP(PD)} + K^2_C) / \sigma^2_{CxP(PD)}$
Planting Date	K^2_{PD}	$\sigma^2_e + \sigma^2_{P(PD)} + K^2_{PD}$	$(\sigma^2_{P(PD)} + K^2_{PD}) / \sigma^2_{P(PD)}$
Pos(PlantingDate)	$\sigma^2_{P(PD)}$	$\sigma^2_e + \sigma^2_{P(PD)}$	$\sigma^2_{P(PD)} / \sigma^2_e$
Cultivar*PlantingDate	K^2_{CPD}	$\sigma^2_e + \sigma^2_{CxP(PD)} + K^2_{PC}$	$(\sigma^2_{CxP(PD)} + K^2_{CPD}) / \sigma^2_{PxR(C)}$
Cultivar*Pos(PlantingDate)	$\sigma^2_{CxP(PD)}$	$\sigma^2_e + \sigma^2_{CxP(PD)}$	$\sigma^2_{CxP(PD)} / \sigma^2_e$
Residuals	σ^2_e	σ^2_e	

The F values were tested according to the relevant degrees of freedom for each mean square component in the ratio using the probability density function for an F distribution in R. For all of these linear effects, an LSD test with a false discovery rate correction in the R package agricolae was used to quantify the mean value for each level within the response variable and assess significant differences in either mean frequency or total area at alpha = 0.05 (De Mendiburu, 2017). The ANOVA and LSD tests were run separately on movement data obtained at each of the five video dates.

Results

Automatic demarcation of single rows from hemispherical video. An automated camera track system with a 360fly (360fly, Inc.) camera mounted 3 m off the ground, allowed us to capture hemispherical videos of 98 single row plots within a RCB design planted at

four different planting dates (Figure 1) (Table 4) (Chapter 3). The RCB design contained four cereal crop species with 16 cultivars in total (Table 4).

Table 4. Cultivars used in the lodging field design.

Latin Name	**Crop**	**Cultivars**
Avena sativa L.	Oat	'Gopher', IL078721,ND021052, 'Reins'
Hordeum vulgare L.	2-row Barley	'AC Metcalf', 'Conlon', 'ND Genesis', 'Pinnacle'
Hordeum vulgare L.	6-row Barley	'Celebration','Quest','Stellar','Tradition'
Triticum aestivum L.	Wheat	'Linkert',MN113946,'Rollag','Shelly'

The camera track system was specifically designed for quantifying lodging and plant movement under field wind conditions, with open source design plans (Chapter 3). Four replicates were in view of the camera track (two inner and two outer replicates), with 2-minute videos taken at each of the four planting dates on five different windy days in July 2017 for a total of 20 videos capturing cereal movement (Table 5) (Figure 2A).

Table 5. Video date and wind speeds.

Video Date	Average Wind Speed (kph)	Gust (kph)	Direction (°)
10 Jul 2017	10.3	14.6	357
11 Jul 2017	6.7	10.3	112
12 Jul 2017	14	18.6	268
13 Jul 2017	10.2	12.9	345
17 Jul 2017	17.8	26.4	164

Average wind speed, gust, and direction at each video date.

By centering the camera over a series of unique panels at each planting date, we calculated the orientation of the field with respect to the camera axes in a given video and

subsequently rotated the input field design at that panel accordingly (Figure 2A-D). The red square on each panel also served to normalize red color values in the RGB frames for comparing color values at a given plot under different lighting conditions. Following this rotation, we transformed the rotated 2D field coordinates into 3D spherical coordinates (Figure 3). The latitude for a given point was used to obtain the number of pixels in the image out to that point, with the longitude used to calculate the number of indexed rows, columns in the image matrix using a law-of-sines relationship. This created a series of four transformed points for each plot, expressed in indexed pixels, that could then be used in cropping functions. We used the plotfinder matlab script (Additional file 1) to automatically generate both cropped images and cropping functions that used these pixel products of the field design transformation to illustrate demarcations of an entire cultivar row and 929cm^2 regions for quantifying plant movement (Figure 4A-D). Visualized on the first still frame, the cropped image of 'Gopher' oat is seen in two different videos whose rotation in relation to the field panel differs (Figure 4A-B). The 929cm^2 regions at canopy height for plant movement analysis is shown in a replicate adjacent to the camera track (inner reps) (Figure 2A, Figure 4C) and not adjacent to the camera track (outer reps) (Figure 2A, Figure 4D). Regions of the same size in the field become noticeably smaller in outer replicates when demarcated in the 360fly still frames (Figure 4D). Along with a cropped image displaying the polygon region of interest, the cropping function generated using Additional file 1 can then be used to crop 929cm^2 regions at each plot and analyze the color components of these plot segments over all video frames to quantify plant movement.

Accuracy of the automatic plot demarcation. We assessed the accuracy of the plot demarcation method over the 5 video dates by comparing manual rotation angle (Θ_{off}) calculation and cropping with the automatic Θ_{off} calculation and cropping functions generated by the plotfinder script. The small Θ_{off} differences (averaging between 0.66° and 2.42°) between automatic and manual estimation propagated larger transformation errors for outer replicates compared to the inner replicates adjacent to the camera track (Table 3). These differences in combined x,y plot coordinate values averaged 1.78cm at the inner reps and 8.74cm at the far reps due to Θ_{off} calculation error propagation (Table 6).

Table 6. Errors in plot demarcation induced from manual vs. automatic Θ_{off} estimates[1]

	10 Jul 2017	**11 Jul 2017**	**12 Jul 2017**	**13 Jul 2017**	**17 Jul 2017**
Avg. Angle Difference (°)	1.64	2.42	0.66	1.19	1.13
Inner reps (cm)	2.89	3.22	1.34	1.12	0.33
Outer reps (cm)	12.83	16.07	5.51	6.78	2.92

[1]Average Θ_{off} differences and subsequent error propagation (in cm) for combined x and y components of the field coordinates and grouped by replicate position at each video date. Manual vs. automatic (plotfinder) estimations of Θ_{off} were used and averaged across the four panels for each video date.

As another metric of the plot demarcation accuracy, we measured how color signals of plant movement were affected by comparing the average normalized red value from the hand demarcated and plotfinder demarcated regions over all frames in the videos. For the inner replicates, the correlation at each video date across all planting dates

and crop cultivars was significantly higher than in the outer replicates (Table 7). On the windiest day with the most plant movement (17 Jul 2017), the correlations between normalized red color values were 0.92 for inner replicates, and 0.76 for outer replicates (Table 7). Likewise on the least windy day (11 Jul 2017), the correlations between normalized red color values were lower overall (r=0.83 for inner replicates, 0.67 for outer replicates) (Table 7).

Table 7. Average correlation[1] of normalized red color values over frames by video date.

Position	**10 Jul 2017**	**11 Jul 2017**	**12 Jul 2017**	**13 Jul 2017**	**17 Jul 2017**
Inner reps	0.83 a	0.83 a	0.87 a	0.77 a	0.92 a
Outer reps	0.69 b	0.67 b	0.77 b	0.62 b	0.76 b

[1]Correlation coefficients (r) of normalized red values over frames between manual and automatic (plotfinder) demarcation methods, averaged over all plots, and grouped by replicate position at each video date.

Processing signals of plant row movement. With the plotfinder method enabling the systematic cropping and color quantification of 929cm^2 plot canopy regions over each frame in a video, we devised a signal processing pipeline to quantify plant row movement from time-varying changes in color across plot canopies. We visualize a sample of plant movement waveforms by plotting the normalized red color values of four cereal cultivars taken at the panel denoting the 25 Apr. 2017 planting date on 10 Jul 2017 (Figure 5A). The normalized red color values of the 929cm^2 regions over all frames in a video revealed color changes at two major scales. The first scale was low frequency (<0.5 Hz), high amplitude color changes detectable due to changes in sunlight exposure from

passing clouds during a single video, which substantially altered the red color values of the plots relative to the red panel. This is evidenced by the shared low frequency, high amplitude wave movements across all plots shown (Figure 5A). The second color change within each of these waveforms, occurring at higher frequency (1-2 Hz) and lower amplitude, can be seen that represent the plant swaying back and forth, thereby changing the mean normalized red value within the demarcated 929cm^2 region (Figure 5A). Digital bandpass filtering was necessary to remove low frequency color changes (less than 0.5 Hz) due to sunlight changes and high frequency waves (greater than 4.9 Hz) due to camera movements and other noise, leaving only the signal of the individual row movement (Figure 5B). The filtered signals of normalized red values are thus centered at 0 and have distinguishable peaks, which are used to calculate the mean natural frequency (ω_n) for the bandpassed peak distribution (Figure 5C). The movement trends of the plotted waveforms in Figure 5A correspond to the behavior of the cultivars in the supplemental video (Additional file 2), such as low ω_n, high amplitude movement ('Gopher' Oat, 'Pinnacle 2-row Barley) and high ω_n, low amplitude movement ('Linkert' Wheat).

Analysis of plant row movement signals. We finally used the peak detection method on the filtered signals of plant movement to generate a distribution of peaks for each plot per video date (Figure 5C). The mean natural frequency (ω_n) obtained from these distributions, modeled as a response in Eq. 10 with appropriate F-tests (see Methods), revealed differences among cultivars and planting dates that were significant in a ANOVA of the linear model on data from the five video dates (Table 8). The position

effect of replicates nested within planting dates was significant at all video dates in explaining variation in mean ω_n (Table 8). The mean ω_n values across all cultivars was 1.37 Hz, with significant differences detected among cultivar means according to an LSD test on two of the five video dates (Table 9). Grouped in Table 6 by crop, wheat cultivars on average had higher mean ω_n values than the other cereals across the five video dates. Different planting dates also possessed significantly different mean ω_n values, though their rank was not universally consistent across the five video dates (Table 10). Notably, the windiest date (17 Jul 2017) contained almost universally lower observations of ω_n across cultivars and planting dates (Table 9).

Table 8. ANOVA P-value results for mean by ω_n by video date

	10 Jul 2017	**11 Jul 2017**	**12 Jul 2017**	**13 Jul 2017**	**17 Jul 2017**
Cultivar	<0.001*	0.011*	0.002*	0.030*	<0.001*
PlantingDate	0.211	0.100	0.145	0.055	0.039*
Pos(PlantingDate)	<0.001*	<0.001*	<0.001*	<0.001*	0.008*
Cultivar*PlantingDate	0.405	0.369	0.441	0.372	0.448
Cultivar*Pos(PlantingDate)	0.712	0.222	0.964	0.023*	0.989

* significant at alpha = 0.05

Table 9. Mean separations for mean ω_n (Hz) between cultivars by video date

Cultivar	**10 Jul 2017**	**11 Jul 2017**	**12 Jul 2017**	**13 Jul 2017**	**17 Jul 2017**
'AC Metcalf' 2-row	1.41ab	1.46a	1.48a	1.25bc	1.25a
'Conlon' 2-row	1.27b	1.46a	1.47a	1.33abc	1.26a
'ND Genesis' 2-row	1.51ab	1.53a	1.50a	1.44ab	1.16a
'Pinnacle' 2-row	1.43ab	1.41a	1.47a	1.28abc	1.11a
'Celebration' 6-row	1.22b	1.48a	1.54a	1.46ab	1.14a
'Quest' 6-row	1.37ab	1.43a	1.43a	1.30abc	1.40a
'Stellar' 6-row	1.45ab	1.28a	1.54a	1.32abc	1.08a
'Tradition' 6-row	1.45ab	1.31a	1.32a	1.28abc	1.15a
'Gopher' oat	1.31ab	1.29a	1.40a	1.18c	1.03a
'IL078721' oat	1.55ab	1.46a	1.50a	1.41abc	1.06a
ND021052 oat	1.59a	1.36a	1.62a	1.21bc	1.15a
'Reins' oat	1.38ab	1.20a	1.34a	1.35abc	1.06a
'Linkert' wheat	1.60a	1.41a	1.48a	1.43ab	1.07a
MN113946 wheat	1.57ab	1.55a	1.56a	1.35abc	1.39a
'Rollag' wheat	1.39ab	1.52a	1.41a	1.64a	1.48a
'Shelly' wheat	1.59a	1.55a	1.60a	1.52a	1.38a

Values followed by the same letter within a column are not significantly different within a video date at alpha = 0.05

Table 10. Mean separations for ω_n (Hz) between planting dates.

Planting Date	**10 Jul 2017**	**11 Jul 2017**	**12 Jul 2017**	**13 Jul 2017**	**17 Jul 2017**
25 Apr 2017	1.37bc	1.52a	1.44b	1.70a	0.85d
5 May 2017	1.47b	1.41b	1.47b	1.19c	1.01c
15 May 2017	1.62a	1.15c	1.27c	1.06d	1.26b
26 May 2017	1.30c	1.59a	1.71a	1.47b	1.53a

Unique letters indicate significant differences between means within a video date at alpha = 0.05

In addition to analyzing variation in mean frequency, we analyzed the variation in the amount of row movement (amplitude) within a 0.2 Hz frequency interval (bin)

between 1.1 and 1.3 Hz. The amplitude within this frequency bin encompassed many mean natural frequencies of the cultivars in this study varied significantly among cultivars and planting dates across data from the five video dates. When modeled as a response in Eq. 10 and analyzed with an ANOVA, the 1.1-1.3 frequency bin had significant cultivar, planting date, and planting date x cultivar interaction effects (Table 11). The position effect of replicates nested within planting dates was insignificant across four of five video dates on the variation in total amplitude (Table 11). Significant differences in mean amplitude among cultivars were detected at one of the five video dates according to an LSD test (Table 12). Cultivars with a lower ω_n generally had more movement in the 1.1-1.3 Hz interval as measured by the sum of the red area between peaks, while those with a higher ω_n had less movement (Table 12). Near-universal increases in total amplitude were observed for the windiest video date (17 Jul 2019) compared to the other video dates among the cultivars (Table 12). Finally, significant differences in the total amplitude of plant movement among planting dates were detected at each video date (Table 13).

Table 11. ANOVA results for the total amplitude of movement (1.1-1.3 Hz bin) by video date

	10 Jul 2017	**11 Jul 2017**	**12 Jul 2017**	**13 Jul 2017**	**17 Jul 2017**
Cultivar	0.003*	<0.001*	0.027*	0.026*	0.005*
PlantingDate	0.021*	0.055	0.277	0.052	0.017*
Pos(PlantingDate)	0.587	0.022*	0.097	0.405	0.293
Cultivar*PlantingDate	0.018*	0.050*	0.221	0.010*	0.052
Cultivar*Pos(PlantingDate)	0.714	0.514	0.342	0.159	0.511

* significant at alpha = 0.05

Table 12. Cultivar differences for the total amplitude[1] of movement (1.1-1.3 Hz bin) by video date.

Cultivar	**10 Jul 2017**	**11 Jul 2017**	**12 Jul 2017**	**13 Jul 2017**	**17 Jul 2017**
'AC Metcalf' 2-row	1.59a	2.44abc	1.78a	1.46a	3.90a
'Conlon' 2-row	1.29a	2.11bc	2.28a	1.84a	2.18a
'ND Genesis' 2-row	1.88a	2.20abc	1.72a	1.37a	2.46a
'Pinnacle' 2-row	1.17a	2.39abc	1.75a	1.74a	3.22a
'Celebration' 6-row	2.39a	1.48c	1.51a	1.48a	1.56a
'Quest' 6-row	1.50a	3.01ab	2.24a	2.36a	3.94a
'Stellar' 6-row	0.88a	2.23abc	1.06a	1.16a	2.30a
'Tradition' 6-row	1.13a	1.91c	1.96a	2.09a	3.13a
'Gopher' oat	2.16a	3.12a	2.37a	2.67a	3.02a
'IL078721' oat	1.06a	1.48c	0.65a	0.96a	0.85a
ND021052 oat	1.19a	1.58c	1.06a	1.63a	2.35a
'Reins' oat	1.61a	1.53c	1.45a	1.24a	1.60a
'Linkert' wheat	1.29a	1.43c	1.19a	1.37a	1.41a
MN113946 wheat	0.85a	2.26abc	1.18a	1.60a	2.32a
'Rollag' wheat	1.24a	1.90c	1.37a	0.99a	2.18a
'Shelly' wheat	1.39a	1.97c	1.71a	2.13a	1.27a

[1]Total amplitude is expressed in percent normalized red color units. Values followed by the same letter within a column are not significantly different within a video date at alpha = 0.05

Table 13. Mean separations for the total amplitude[1] of movement between planting dates

Planting Date	**10 Jul 2017**	**11 Jul 2017**	**12 Jul 2017**	**13 Jul 2017**	**17 Jul 2017**
25 Apr 2017	1.91a	1.91bc	1.80a	1.21b	0.83c
5 May 2017	1.43a	2.10b	1.54a	1.89a	3.87a
15 May 2017	0.89b	2.70a	1.82a	2.04a	2.95a
26 May 2017	1.63a	1.63c	1.43a	1.61ab	1.96b

[1]Total amplitude is expressed in percent normalized red color units. Unique letters indicate significant differences between means at alpha = 0.05

Discussion

Measurements of cereal crop lodging, while increasingly possible at high throughput through UAVs and image analysis, cannot capture the dynamic response that a cereal crop experiences during high winds or storms. Treating movement as a response variable could improve a breeder's understanding of cereal wind resistance by relating cereal physiology to repeated measures of plant movement under different wind conditions and final lodging outcomes. There are obvious challenges to phenotyping plant movement on a large-scale agricultural experiment using mechanical methods. Manual vibration and timing tests would prove laborious on the scale of common field experimental designs, while mechanical sensors on tens or hundreds of replicates would present data synchronization challenges for large field experiments. Thus, a video analysis method using a colorimetric, signal processing approach to quantify movement offers a non-invasive measure of this dynamic phenotype that is better scaled to agricultural experiments. The desired capabilities of a scalable phenotyping method for plant movement are twofold: the method must be systematic enough to eliminate sources of human or equipment measurement errors under the intermittent winds that excite plant movement, while providing enough data of replicated varieties to elucidate trends in movement that require increased statistical power to discern in the field. The pairing of novel hemispherical image analysis of agricultural plots with the analysis of plant canopy movement in a systematic way enables differentiation of crop movement at the cultivar level. Though the analysis of plant movement from video data predates digital video, we consider our method generalizable to available camera technology and common field

experimental designs for measuring movement as a plant phenotype for breeding or other biological purposes (Finnigan and Mulhearn, 1978).

Demarcating individual crop rows from 360 video is novel with respect to high throughput image analysis of agricultural research plots, which is often performed using UAV captured images. Demarcating plots from a 360 image negates the need for stitching images captured by UAV mounted cameras, though at the cost of a smaller field coverage on a per image basis compared to multiple images stitched into one from a UAV (Shi et al, 2016). In methodological studies of UAV image alignment of agricultural plots, regions of a field are identified through ground control points (GCP) with known GPS coordinates, which can be manually tagged in each image and then used to aid alignment along with shared spectral features in the images being stitched (Bendig et al, 2013). Plot misalignments induced by stitching error depend on the height of the UAV, spectral properties of the image, and number of GCPs. Among published studies, these stitching errors on average range from 1.5 cm to 4.5cm at UAV heights of 30m and 100m respectively, and 8cm to 13cm depending on the spectral band analyzed and the number of GCPs used (Honkavaara et al 2013; Gomez-Candon et al, 2014). Our average plot coordinate misalignment errors of 1.78cm for inner reps (at 2.28m from the camera track) and 8.74cm (at 6.86m from the camera track) for outer reps falls within the errors induced by stitching algorithms using GCPs. In theory, mounting the camera higher would decrease the error due to angle estimation errors by the plotfinder script (Additional File 1) at a given distance, as points would shift towards the center (pole) of the 360 image. While a high image spatial resolution is not critical for the measurement

of plant movement from a time-varying color signal, decreasing this resolution will make subsequent analyses more sensitive to errors in camera system alignment or angle calculation. Despite alterations to camera system dimensions, the final errors will heavily depend on the panel being in alignment with the field design, as any misalignment will propagate at further distances even if the angle of the panel is accurately quantified by the plotfinder script. The plot demarcation method could be adapted to other cropping systems and field designs that desire a large field of view and the possibility for repeated imaging or videos of agricultural plots with careful construction of the camera system (Chapter 3).

The plot demarcation and plant movement quantification methods are well integrated via the use of the panels that enable normalization of color values in RGB video frames and identification of plots within the RCB field design. From this normalization and subsequent bandpass filtering of raw waveforms, we were able to compare parameters of plant movement across videos where different lighting conditions were present. Bandpass filtering also allowed for the removal of higher frequency (>5Hz) color changes due to camera vibrations induced at sufficiently high windspeeds on the camera system, leaving a signal of plant movement for analysis. The ability to treat parameters of plant movement such as natural frequency and amplitude as phenotypes that can be analyzed in common experimental designs such as the RCB represents a rigorous analytical framework for further testing models of plant wind interactions in the field. In the test of the plot demarcation and signal processing pipelines, we analyzed the RCB separately at 5 different dates. Lighting and wind conditions are expected to vary

over different dates, and changes in lighting conditions (due to sun elevation or cloud cover) at the time of imaging will affect the absolute amplitude measurements as they are quantified based on the area under the bandpassed waveforms. However, a variety prone to larger amplitude movements will still be detected relative to those with lower amplitude movements when measured over a constant area of the plant canopy (929cm^2 in our case), even if the magnitude of the absolute amount of movement is less due to lighting conditions in a given video. Thus, a researcher employing this method over an entire growing season to investigate biological questions would be advised to employ a repeated measures ANOVA account for variation due to windspeed and lighting conditions among sampling dates in a final model of plant movement comparing varieties or crops. The RCB field design we used allowed us to statistically test the results from the video and signal processing pipelines by comparing relevant experimental effects and their interactions at separate video dates. The presence of a significant effect of replicate position (inner vs outer) for natural frequency indicates that blocking the experiment with camera distance, as was done here, is critical in minimizing the effect of distance from the camera on mean natural frequency. Such effects on the variation in mean natural frequency are likely manifestations of errors in angle calculation identified in lower correlations between automatic and hand plot demarcation, indicating that there is more error in quantifying color changes at greater distance from the camera. This primarily stems from errors in calculating Θ_{off}, resulting in a shift of the 929cm^2 region to another plot and capturing a color signal that is not representative of the intended plot canopy. While the plots captured in the hemispherical still frames occur at varying latitudes

(viewing angles) in the images that are in theory affected by different lighting conditions, the predominant lack of a significant position effect on plant movement where the total amount of color change over time is directly quantified suggests that this issue is not as critical as improper angle calculation for accurate measurement of plant movement. That said, care should be taken to account for variation in lighting conditions at different viewing angles within hemispherical images for other applications if specific indices (ie ratios of spectral bands) are desired.

Mechanical estimates of plant movement, while useful for theoretical validations, are not as easily scaled to the level of field agricultural experiments compared to video based, colorimetric methods. Manually collected data on crop movement has been used to select for lodging resistance in cereals in the absence of naturally induced lodging, such as the 'snapback' trait in oats and other cereals (Hancock and Smith, 1963). The snapback trait consists of a researcher drawing a cereal row back, and rating (ie 1-10 scale) the strength and springiness of the stem (Grafius and Brown, 1954; Murphy et al, 1958). The low trait heritability of subjective snapback scores spurred the development of a more precise measure of stem displacement through hanging weights at a standard location along cultivar stems, thereby providing an estimate of torque that a stem can resist versus the torque that is applied (Coefficient of Lodging Resistance) (Grafius and Brown, 1954). Nonetheless, both snapback and coefficient of lodging resistance traits are hindered by subjective or cumbersome measurement. Free vibration tests, where a researcher pulls the main cereal stem back a set distance and manually times the subsequent oscillations, represents a standard field measurement technique for stem

frequency for validating models of plant movement (Berry et al, 2000; Berry et al, 2006). Mechanical estimation of plant movement through accelerometer data, while increasingly feasible with compact sensors, poses difficulties in large field experiments such as the RCB design we used given difficulties in scaling materials and synchronizing data across all plots at any given point in time, notwithstanding possible mechanical interferences with plant movement (Flesch and Grant, 1991)**.** Regardless of the method used to obtain plant movement data, any signal of wind induced plant movement will be highly intermittent given the inconsistent nature of wind speeds and direction at canopy level and the low frequency of plant oscillations. Both of these factors make signals of plant movement poor candidates for analysis via standard signal processing techniques such as the fourier transform. While errors might be induced due to physical properties of the camera system used, the ability to analyze multiple replicates of the same varieties provides the statistical power needed to differentiate cultivar differences in plant movement to provide insights for field investigations of plant-wind interactions.

The cultivar mean natural frequency (ω_n) values estimated by our method fall within ω_n values either theoretically or empirically determined for cereal crops. Theoretical natural frequencies of a generic cereal crop range between 1.10 and 5.31 Hz, based on dimensionless parameters while empirical data on in-field wheat stems (cultivar 'Mercia') using a manual free vibration resulted in an average natural frequency of 0.91 Hz (Baker, 1995; Berry et al, 2003). Additional empirical data from free vibration tests in spring barley indicate an average natural frequency of 0.67 and 0.60 for the cultivars Golden promise and Optic, respectively (Berry et al, 2006). While mean ω_n values

calculated for the cultivars in our study were higher on average (1.37 Hz) than those reported for different cultivars of the same cereal crops, barley cultivars in our study generally had lower resonant frequencies than the wheat cultivars, a trend also apparent in (Berry et al, 2006). Observations taken on the video date with the highest average wind speed and gusts were almost universally lower in mean ω_n values for cultivars and planting dates, which is to be expected as the wind moment increases thereby reducing the natural frequency by the square root of the increase in wind moment, all else equal (Flesch and Grant, 1991) (Eq. 2) (Table 6). Considering its generalizability to different field applications, these video and signal processing methods represent good candidates for obtaining more information about the phenomenon of plant movement and its relationship to lodging resistance.

Conclusions

We submit a novel video analysis pipeline that enables the automatic demarcation of agricultural plots from 360 video and a signal processing pipeline for analyzing color signals of plant movement in common field experimental designs. When coupled together, this method can be used to analyze video taken under varying wind speeds, allowing for the quantification of plant natural frequencies of movement under direct wind stress where typical high throughput phenotyping platforms (ie UAVs) are not suitable. When applied over a growing season, this method should amend itself to discerning trends in plant movement over time. These could include the physiological relationships between physiology, movement, and lodging, or even thigmotropic responses of plant tissues to plant movement (Jaffe, 1973). In the broader goal of

improving lodging resistance of cereal crops, the analysis of plant movement from 360 video will expand the quantifiable variation of this complex trait for use in plant improvement.

Figures

Figure 1. Camera track system. The automatable camera track system that to which the 360 Fly camera was mounted.

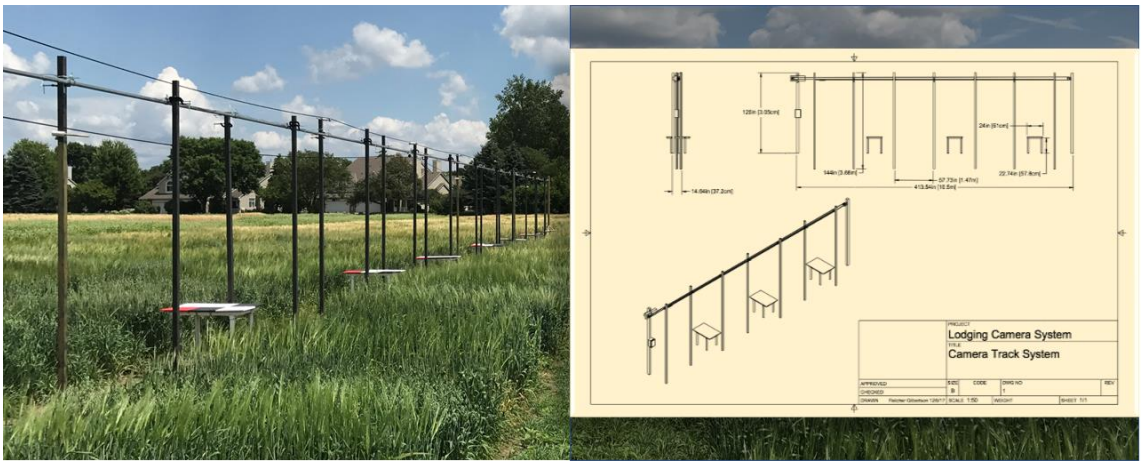

Figure 2. Rotation of field coordinates. The camera orientation is determined from still frames (A). The sample still frame shows the position of the inner (orange dashed rectangles) and outer (blue dashed rectangles) replicates in view with respect to the camera track (A). The red square on the panel is masked out from the rest of the image, and the leftmost corner is identified with the color values +/- 40 pixels from this corner used to determine which way the panel is facing (B). Once the direction and degree in this direction that the image is rotated is quantified (Θ_{off}), the field design coordinates are rotated in that direction such as 45.9 degrees toward the Northeast (C) or 41.9 degrees toward the southwest (D).

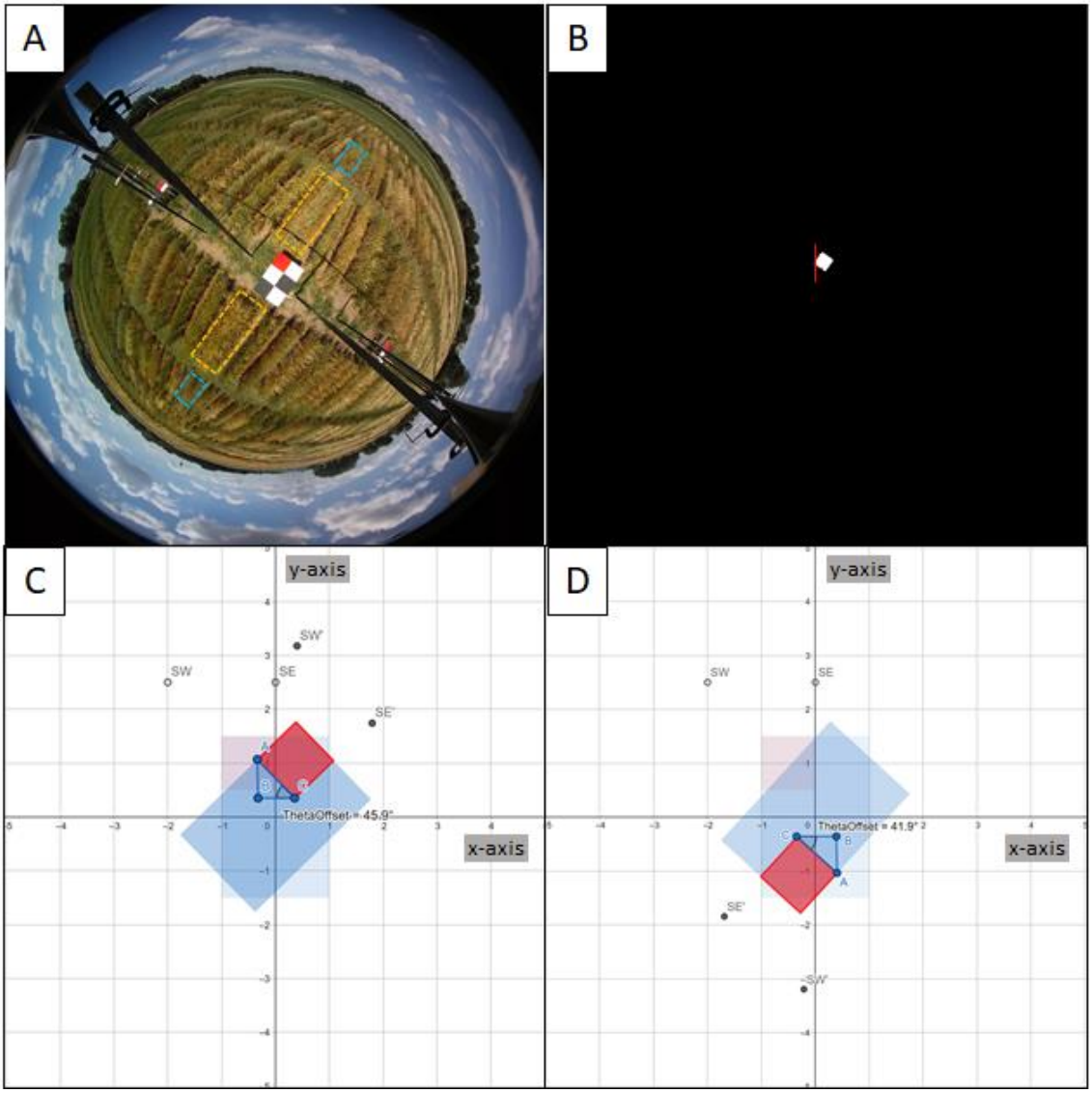
A
B
C
y-axis
x-axis
SW'
SW
SE
SE'
ThetaOffset = 45.9°
D
y-axis
x-axis
SW
SE
ThetaOffset = 41.9°
SE'
SW'

Figure 3. Spherical transformation via triangulation. After accounting for camera rotation using Θ_{off}, distances to the rotated point (x'_n, y'_n) are used to calculate the longitude, and along with height (z_n) the latitude of a point of interest transformed on to a spherical plane.

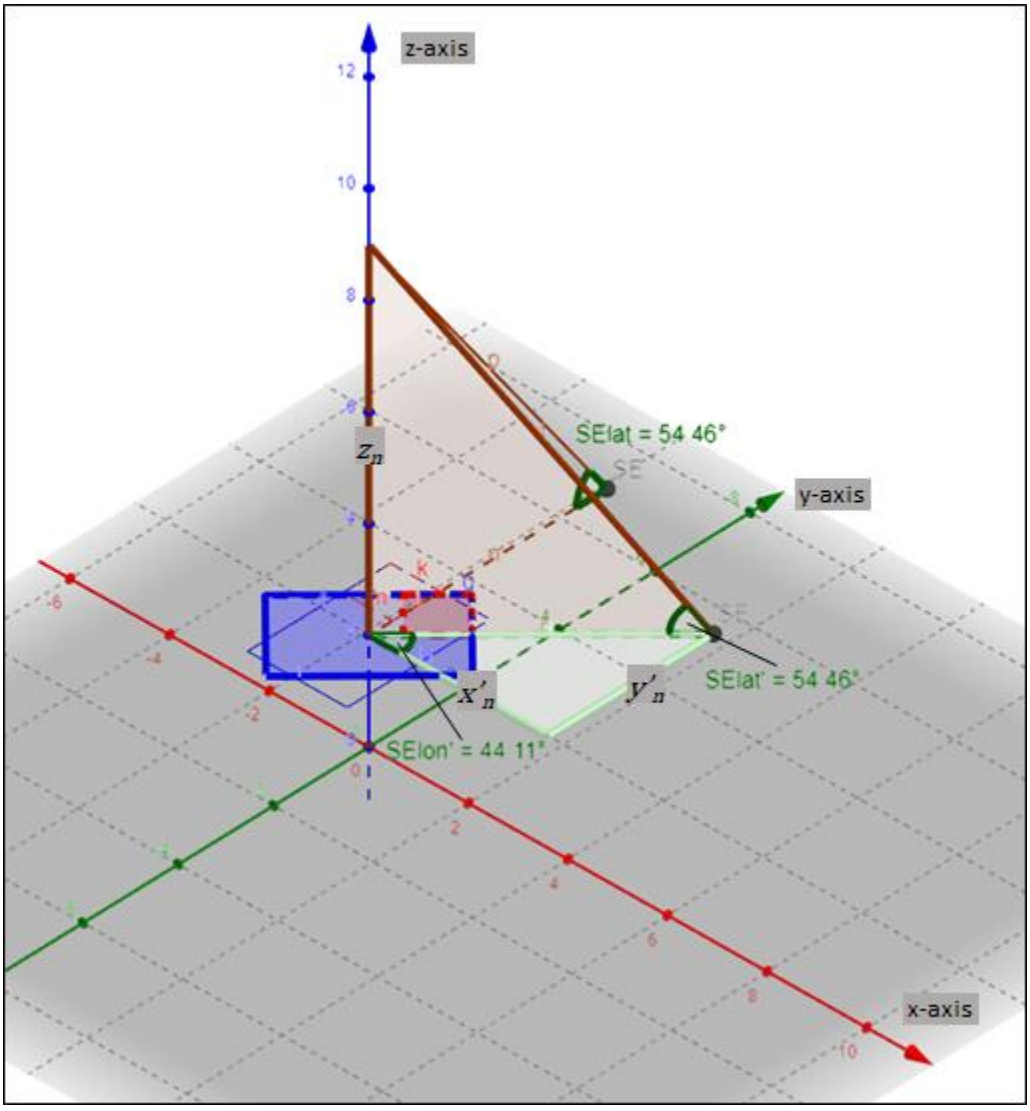

Figure 4. Cropped images showing automated plot identification results. Two still frames from different video dates (A,B) of the same oat plot ('Gopher') demarcated in two different orientations. Two still frames from the same video date below showing the 929cm^2 demarcation for the analysis of plant movement. 'ND021052' Oat as an inner rep (C - green circle highlight) and 'Quest' 6-row Barley as an outer rep (D - green circle highlight).

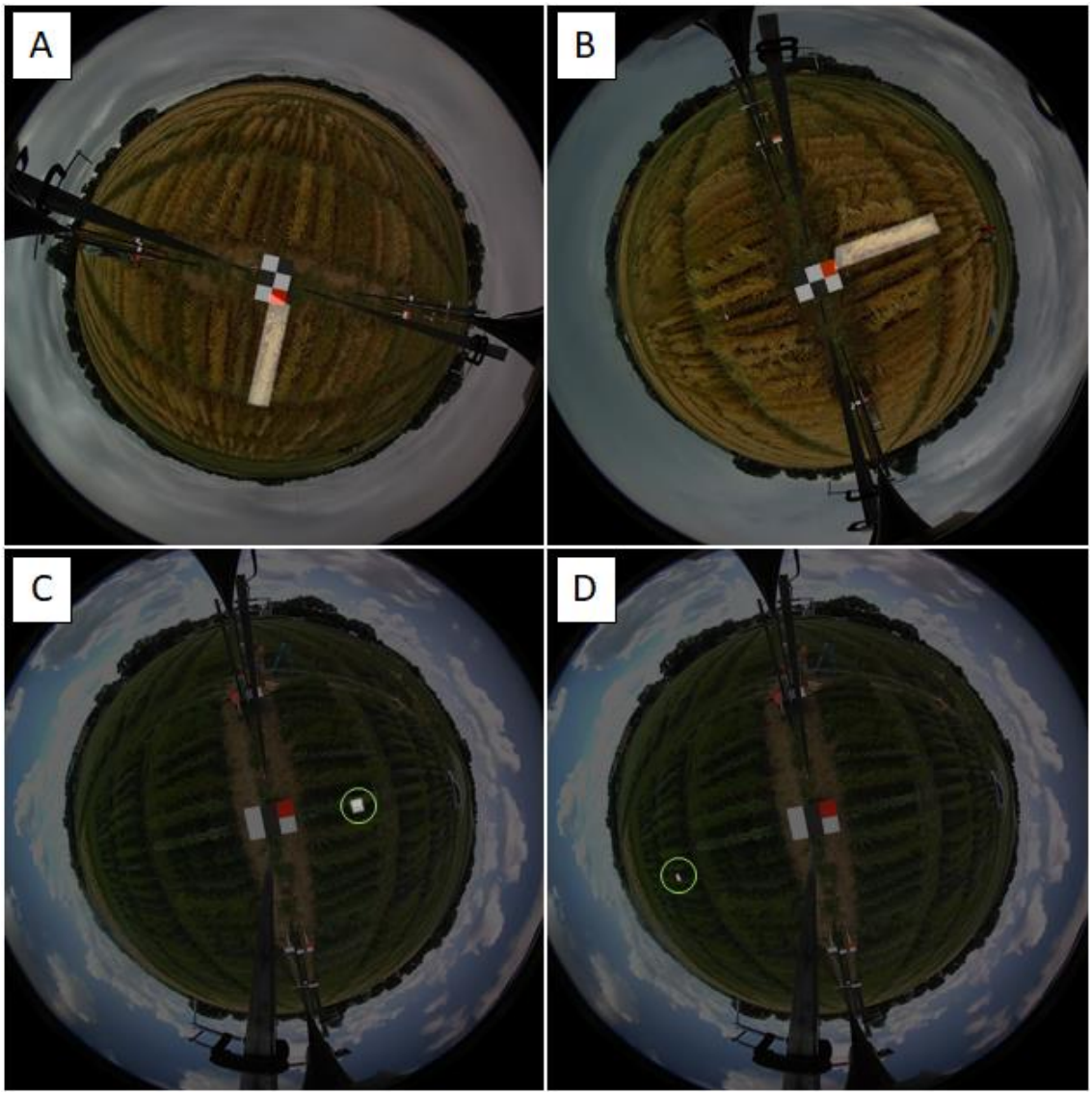

Figure 5. Signal processing visual. The red color value for each frame is normalized to the red color value for the red square on the panel, generating a waveform of both plant movement and outdoor lighting conditions over the video (Column A). The waveforms in column A are then bandpassed, centering the signal at 0 and removing the low frequency (<0.5Hz) components of the signal (Column B). Peaks within the bandpassed signals are identified with a minimum prominence of 0.005 Normalized Red Value, with the distance between each peak (in frames) calculated and divided by the frame rate to estimate the natural frequency (ω_n, in Hz) to the next peak. The mean of the distribution of these frequencies constitutes the ω_n for the plot (Column C- red lines).

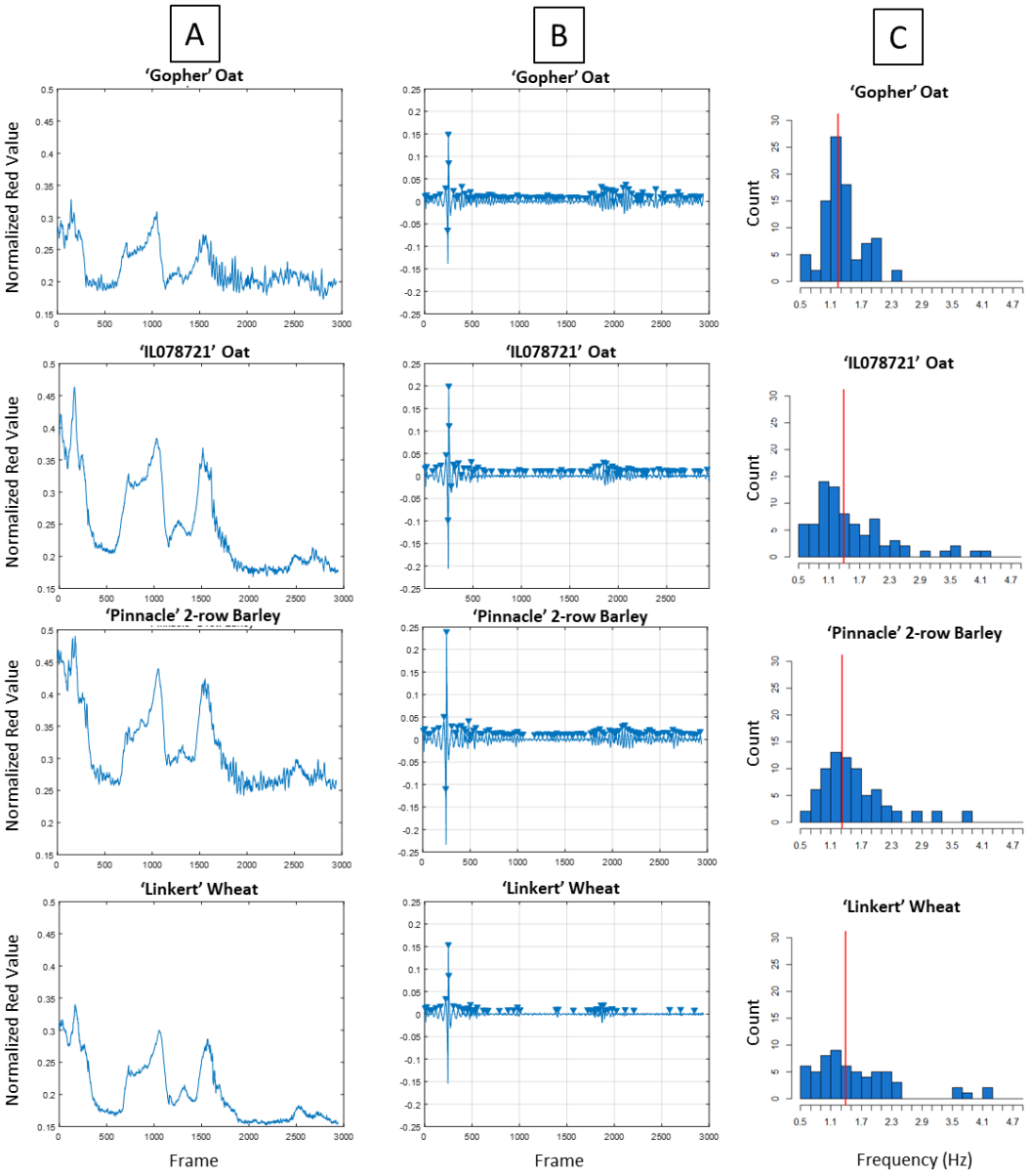
A
B
C
'Gopher' Oat
'IL078721' Oat
'Pinnacle' 2-row Barley
'Linkert' Wheat
Normalized Red Value
Count
Frame
Frequency (Hz)

Chapter 4:

A wind tunnel analysis of cereal crops for insights on lodging resistance.

Alexander Q. Susko[1], Stijn Vandycke[2], D. Jo Heuschele[1], Peter Marchetto[2], Michele Guala[3], and Kevin P. Smith[1].

[1]University of Minnesota Department of Agronomy and Plant Genetics, 411 Borlaug Hall, 1991 Upper Buford Circle, St. Paul, MN 55108

[2]University of Minnesota Department of Bioproducts and Biosystems Engineering, 1390 Eckles Ave., St. Paul, MN 55108

[3]University of Minnesota Department of Civil, Environmental and Geo-Engineering, St. Anthony Falls Laboratory, University of Minnesota. 2 3rd St. SE , Minneapolis, MN 55414

Introduction

Lodging resistance is defined as the resistance to plant stem failure under high winds. This trait is a continuously targeted trait for improvement by breeders of cereal crops. Cool-season cereals such as *Avena sativa* L. (oat), *Hordeum vulgare* L. (2- and 6-row barley), and *Triticum aestivum* L. (wheat) are especially prone to lodging during high winds accompanying severe storms. Root lodging, constituting buckling at the stem base, is particularly detrimental to the cultivation of cool season cereals by causing substantial yield reductions from reduced photosynthesis and difficulties in mechanical harvest (Weibel and Pendleton 1964). While field-based visual severity ratings can be used to identify genes and linked markers for selecting root lodging resistance, field ratings of root lodging are not informative of the plant's direct interaction with the wind (Tumino et al 2017). Plant-wind interactions encompass many physical parameters whose optimization in theory could produce a more lodging resistant cereal (Baker 1995). Superior ideotypes have been proposed that combine such parameters, such as a lower center of gravity on the stem with increased stem diameters, to improve plant wind resistance and reduce the probability of root lodging within narrow ranges of cereal germplasm (Berry et al 2006; Berry et al 2007). However, minimal testing of cereal crops under wind tunnel conditions has been conducted, thus leaving a gap in evaluating variation in stem bending under known drag forces induced by controlled winds. Knowing how a diverse panel of cereal crops vary aerodynamically and bend under

known drag forces could result in new phenotypes for the selection of enhanced lodging resistance.

Root lodging occurs when the force inducing bending (or bending moment) of the stem exceeds a critical bending moment of the stem base, causing the base of the stem to buckle (Baker et al 2014). In addition to gravity, plant stems are subjected to the drag force caused by wind that contributes to stem bending (Zebrowski 1999). Being able to estimate the proportion of force caused by plant structures in a cereal crop in equilibrium in an airstream could be necessary to identify plant structures or stem bending attributes that reduce the probability of wind induced lodging.

The drag coefficient C_d, representing the proportion of forces due to drag acting on the plant, is quantified as

$$c_d = \frac{2F}{\rho_{air} u^2 A}$$

where F is the known force required to achieve a certain deformation in the airstream, A is the frontal area of the plant and u is the velocity uniformly impinging on the plant and ρ is the air density. As the plant changes its shape in a compliant fashion while bending under the wind, both C_d and A decrease. The deformation of grasses at increasing wind speed reduces the drag coefficient, and as such a standard stage and geometry of deformation must be assessed to compare across cultivars and cereal crops (Gillies et al 2002). In tandem with testing whether drag coefficients vary among common cereal crops, the bending behavior of cereal stems under a known drag forces could yield insight into variation in stem bending that could confer lodging resistance. Experimental

assessment of cereal stem bending under known forces include the coefficient of lodging resistance (CL_r), which quantifies the torque resisted to torque applied for a known force at a point on the stem (Grafius and Brown 1954). Early measurements in oat indicate that more lodging resistant genotypes can withstand greater applied torque via a flexible, whip like, stem where bending is distributed along its length (Norden and Frew 1959).

Wind tunnel testing of cereal crops offers the opportunity to obtain detailed phenotypes relevant to lodging resistance that cannot be quantified in the field. By quantifying these phenotypes using video analysis, we can assess variation in plant drag coefficients and cereal stem bending under controlled wind intensities. Wind tunnel testing serves to isolate two aspects of the complicated problem of lodging in cereals: the estimation of wind induced forces on the plant that cause stem bending, and the response of the stems under a known drag force. Wind tunnel research on cereal crops has focused on the model level to calculate the fluctuating airflow at canopy height (I Finnigan and Mulhearn 1978). Early video analysis revealed the frequency of oscillations in a model field (II Finnigan and Mulhearn 1978), describing periodic deformation of the plants in response to the mixing layer structure of turbulence in the canopy. The increased capability of video analysis could allow for the development of methods to better quantify both plant drag coefficients and stem bending under controlled, wind tunnel conditions. These metrics could in turn be used to estimate the forces a cereal is experiencing under known wind velocities, and to better identify genotypes whose stems can ideally deform, possibly contributing to field root lodging resistance.

We present a wind tunnel experiment on a diverse panel of oat, 2- and 6-row barley, and wheat cultivars. Our objectives are to 1) quantify for single cereal plants the drag coefficient and parameters of stem bending, 2) to compare drag coefficients, stem bending among cereal crops, and 3) to relate drag coefficients, stem bending to plant physical traits to better understand plant structures or physiologies that could confer lodging resistance for these major cereal crops.

Methods

Germplasm. We tested 38 cultivars of four different cereal crops (oat, wheat, 2- and 6-row barley), selecting cultivars that were morphologically variable and varied for their lodging resistance in field trials (Table 1). A larger proportion of the cultivars selected were oat given increased records of their field lodging variability in our breeding program.

Table 1. Germplasm used in the study

Latin Name	Crop	Cultivars
Avena sativa L.	oat	'Gopher', IL078721,ND021052, 'Reins',00P28-AN01B1,'BADGER',IL00-1030,MN06203,MN07104,MN09115, MN09230,MN10121,ND060182,ND060342,OA1253-1,OA1342-2,P0216A1-1-45,P0528A1-1,SD041445-119,SD050616,SD090552,SD090882, SD111946,SD120289,'Stout',WIX8791-1
Hordeum vulgare L.	2-row barley	'AC Metcalf', 'Conlon', 'ND Genesis', 'Pinnacle'
Hordeum vulgare L.	6-row barley	'Celebration','Quest','Stellar','Tradition'
Triticum aestivum L.	wheat	'Linkert',MN113946,'Rollag','Shelly'

Plants were seeded into 16.5 cm diameter, 13 cm tall terra-cotta pots in the greenhouse in January 2018 containing LC8-Sunshine mix (Sun Gro Horticulture, Agawam, MA). The potted seedlings were randomly assigned to one of three blocks on the greenhouse bench in a randomized complete block design. Greenhouse temperatures were maintained at 21°C during the day and 18°C at night, with an 18 hour photoperiod. Plants were removed from the greenhouse on the day of their wind tunnel testing at approximately 18 days after heading, with one block tested in the wind tunnel per day.

Table 2. Chapter 4 list of abbreviations

Variable	Definition
A	Projected surface area of plant at time of cd estimation (m^2)
A_{init}	Initial surface area of plant prior to bending (m^2)
A_{leaf}	Area of plant leaves downwind of windward edge (m^2)
a	Point along the x axis where the point on the upright plant (b) would intersect upon complete bending (cm)
b	Point along the y axis on the upright plant (cm)
c	Scaling coefficient in the power curve modeling plant bending
c_d	Drag coefficient
CL_r	Coefficient of lodging resistance
d	Exponential coefficient in the power curve modeling plant bending
F	Force required to bed a plant to 50 degrees (N)
H	Height of plant (m)
h	Length along stem from base (cm)
p_{atm}	Observed atmospheric pressure (mb)
p_{dry}	Pressure of dry air (Pa)
p_{vap}	Pressure of water vapor (Pa)
q	Dynamic pressure
R_{air}	Ideal gas constant of dry air
R_e	Reynolds number
R_{vap}	Ideal gas constant of water vapor
T	Wind tunnel temperature (°K)
T_{dp}	Dew point temperature (°C)
u	Velocity of wind (m/s)

v	Kinematic viscosity of air (m^2/s)
x	Distance along the x axis (downwind) in the wind tunnel from the base of the plant (cm)
x_{min},x_{max}	Minimum and maximum x distances among points on the windward edge (cm)
y	Distance vertically along the y axis in the wind tunnel from the base of the plant (cm)
Θ	Bending angle of the plant in the wind tunnel (°)
ρ_{air}	Density of humid air
ρ_{Hg}	Density of mercury

Physical plant measurements: We took several measurements of plant morphological traits prior to wind tunnel testing. Heading date (anthesis) was recorded in the greenhouse as the number of days since planting when 50% of the first panicle or spike emerged. We measured plant stem strength using a load cell mounted to an aluminum bar the day before subjecting each block to wind tunnel testing and recorded the force (in Kgf) required to bend all stems at the half height point in one pot to an approximate 50° angle with respect to the ground (Wiersma et al 2011). This 50° bending angle is hereafter referred to as the reference stem deformation. Plant height, measured from the base of plant stems to the tip of the tallest panicle or spike (cm), was measured the day before wind tunnel testing. Following the experiment, we destructively sampled each plant's stem and leaf tissue (without panicles or spikes), and weighed them collectively following 3 days in a 60°C dryer to obtain an estimate of leaf and stem biomass (g).

Wind Tunnel Specifications. We subjected each pot to testing in the atmospheric wind tunnel of the St. Anthony Falls Laboratory at the University of Minnesota Twin-Cities. The wind tunnel is a closed-loop of 37.5m in length with a cross-section of 1.7m x 1.7m and a main test section of 16m, equipped with a 149 kW fan (Howard et al. 2016). Tunnel modifications included a pot holder to hold the pot flush with the tunnel surface,

constructed out of 9.5mm thick aluminum sheet metal with a hole matching the diameter of the terra cotta pots and a wooden based beneath that was used to replace one of the floor panels.

The wind tunnel testing protocol consisted of an uninterrupted video of plant bending lasting 3 min 5 sec. Videos of each wind tunnel test were captured with a Canon EOS 5D camera with an Ultrasonic EFS 60 mm lens with a maximum aperture of f/1.5. Each video contained a frame size of 1920 pixels x 1080 pixels at a frame rate of 24 fps, and were written to a Lexar Professional 256GB SD card at a rate of 160 MB/s. Recording was initiated upon starting the airflow, with the fan maintained at 140 rpm (~4 m/s windspeed) for 50 seconds. The fan accelerated to and maintained 270 rpm (~8 m/s windspeed) and 400 rpm (~12 m/s windspeed) in two subsequent 50 sec intervals. At 2 min 30 sec into the test, the fan decelerated to 140 rpm over a 15 sec interval and was stopped at 2 min 50 sec into the test. Camera recording continued until 3 min 5 sec after test initiation, recording approximately 35 seconds of plant recovery as the wind in the tunnel decelerated and stopped.

Video-derived plant measurements: Several phenotypes used to describe plant aerodynamics and bending were obtained from the videos via a Matlab (v 2016b) script TunnelAnalysis_published.m (see Data Availability section). First, each frame of a video (Figure 1.1) was masked to show plant tissue (Figure 1.2), with masked points on the windward edge plotted and fit by a power law curve (Figure 1.3) containing a scaling coefficient (c) and power law exponent (d) coefficient. Second, the corresponding x distance where the half height point for each plant was bent to the reference deformation

was found (Figure 1.4) and used along with the fitted value of the power law at this x distance (Figure 1.5) to estimate the bending angle Θ at any frame (Figure 1.6). The effective frontal area, used in calculating the drag coefficient, was obtained for any Θ as the projection of the plant area exposed to the airflow along the windward edge (Figure 1.7). Equations (Eq 1,2,4,4a-h) describing the method for measuring these phenotypes from videos are found in Supplementary Material, Section 1 (ESM_1.pdf).

The drag coefficient (C_d) was quantified at the reference deformation ($\Theta = 50°$). The force required to bend all stems to this angle was determined from the load cell, and thus was equivalent to the drag force induced by the wind and responsible for the same amount of bending in the wind tunnel. The velocity and pressure values, along with effective frontal area, were obtained at the reference deformation from the pitot tube time history to estimate the C_d. The subsequent range of Reynolds number values, based on the incoming velocity, plant height, and kinematic viscosity of air ($R_e = uH/\nu$), where C_d values were estimated, ranged between $3.5x10^5$ and $1.1x10^6$. For plants that did not reach a Θ of 50° bending during the test, the minimum Θ reached and associated pitot tube data were used to estimate the C_d. Equations (Eq 5a-f) describing velocity estimates from the pitot tube measurements and the plant C_d estimates from both force measurements and the video analysis are included in Supplementary Material, Section 2 (ESM_1.pdf).

We quantified stem bending resistance under the action of the wind drag force using a second metric based on the coefficient of lodging resistance (CL_r) introduced by Grafius and Brown (1954), (see Figure 2A-B). CL_r is a proportional measure of the amount of torque resisted by a cereal stem during bending under a known force: its

estimate is therefore provided for the stem in equilibrium at the moment of known reference force (Θ = 50° or minimum Θ), i.e. at the same instant in the video where the drag coefficient is estimated. Equations (Eq 6, 7a-b,8a-e) describing the estimation of CL_r from videos and are found in Supplementary Material, Section 3 (ESM_1.pdf), along with a supplemental video demonstrating Eq 6, 7a-b,8a-e: the tracking of a fixed point along the stem through bending in the process of CL_r calculation (ESM_2.avi).

We excluded 18 pot videos (14 oat replicates, 4 2-row barley replicates) from analysis due to the pot becoming dislodged during the wind tunnel test or video recording terminating prior to the end of the test, thereby invalidating the angle measurement and derived values.

Data organization and statistical analysis: All video-derived measurements described above were quantified at each frame, with the matlab script producing a tab delimited text file with each trait in unique fields, and a separate text file with bent stem model coefficients (c,d) in unique fields for each pot. Both text files contained a row for each frame in the video analyzed. The pitot tube recording dynamic pressure and temperature data averaged over a 1 second sampling window. Using the windtunnelParse_published.r script (see Data Availability section), measurements performed at each frame of the video recording were averaged every 24 frames to correspond with the pitot tube measurements averaged over the same 1s time interval. The R script quantified the drag coefficient at the reference deformation for the time in the video where the reference bending was met, as well as the CL_r. This script also identified the bending angle at maximum wind

velocity (Θ_{max}) and the power law exponent marking the stem curvature (d) at the time of C_d and CL_r estimation.

We analyzed the crop, cultivar nested within crop, and block effects in an additive linear model for the video derived phenotypes using an analysis of variance (ANOVA) on C_d, Θ_{max}, d, and CL_r response values using the linear model

$$y_{ijk} = \beta_0 1 + \beta_1 x_{i1} + \beta_2 x_{i(j)2} + \beta_3 x_{k3} + \varepsilon_{ijk}$$

With $ß_1$ representing the effect of the *ith* crop, $ß_2$ the effect of the *jth* cultivar nested within the *ith* crop, and $ß_3$ the effect of the *kth* block. , and ε_i the error term. For crop effects, we present the mean separations according to an LSD test with an alpha value of 0.05. Mean values of angle and bending coefficients are also plotted as crop averages every second along with 95% confidence intervals using the Matlab functions boundedline.m. We calculated Pearson correlation coefficients among the linear relationships of the physical and video-derived plant phenotypes using the cultivar averaged values. Finally, we conducted a sensitivity analysis on the drag coefficient and the coefficient of lodging resistance based on an increase of a 25% for the phenotypic parameters Θ_{max}, d, Heading, Strength, Height, and Biomass.

Results

Aerodynamic variation of cereal crops. The experimental mean C_d was 0.71 with a standard error of 0.05 and a 95% confidence interval spanning 0.59 and 0.81. As assessed by the C_d estimates in this experiment at reference deformation conditions,

cereals did not vary aerodynamically at the crop level (p = 0.71) or at the cultivar nested within crop level (p = 0.24) The block effect for Cd was significant (p = 0.01).

Variation in the Coefficient of Lodging Resistance. Video analysis enabled tracking the transit of a fixed mid height point along the modeled stem curve and to estimate the CL_r at the moment of known drag force F (Video 1). The mean CL_r value for each cereal crop species under the known force at the reference deformation was 0.09. The CL_r value at the reference deformation varied significantly among crops ($p<0.001$) and blocks ($p < 0.001$), but not among cultivars nested within crops (p = 0.17). Wheat had a significantly higher mean CL_r than oat, while 2- and 6-row barley was not significantly different from either oat or wheat (Table 3)

Table 3. Mean separation for video estimated parameters by crop species*

Crop	Mean C_d	Mean CL_r	Mean d	Mean Θmax (°)	Mean Θ Recovery (°)
wheat	0.76^{a}	0.18^{a}	0.58^{a}	54.3^{a}	5.2^{a}
6-row barley	0.83^{a}	0.10^{b}	0.63^{a}	46.1^{b}	3.6^{b}
2-row barley	0.68^{a}	0.09^{b}	0.59^{a}	48.2^{ab}	4.4^{ab}
oat	0.61^{a}	0.07^{b}	0.68^{a}	48.2^{b}	4.2^{b}

*Unique letters indicate significant differences between means at alpha = 0.05

The modelled curvature at the reference deformation of the stem via the d power law coefficient in the stem bending equation also varied significantly (p=0.05) among crops, though not among blocks (p = 0.5) or cultivars nested within crops (p = 0.77). According to the LSD test however, mean d coefficients among crops were not significantly differentiated at the time of CL_r, C_d estimation (Table 3).

Variation in Bending Angle (Θ, Θ_{max}) and Recovery. The average bending angle Θ for each crop over the wind tunnel test is shown with 95% confidence intervals at each

second in the video (Figure 3). The bending angle at maximum velocity in the wind tunnel (Θ_{max}) varied significantly by crop (p=0.01). Significant block (p = 0.002) and cultivar nested within crop (p = 0.004) were also significant for $\Theta_{max.}$ Wheat had the highest mean Θ_{max}, though the differences between wheat and other crops were not significant according to an LSD test (Table III). Recovery angle also varied significantly among crops (p = 0.03), blocks (p = 0.02), and cultivars nested within crops (p = 0.03). A significant, positive relationship existed between mean Θ recovery and Θmax (r=0.59, p<0.001), while the relationship between mean Θ recovery and *d* at the reference deformation (r=0.01,p=0.9) was not significant.

Phenotypic Correlations. Correlations across cultivars of major video derived phenotypes (C_d, CL_r, Θ_{max}, and *d*) with plant physical traits are presented in Table 4.

Table 4. Phenotypic correlation matrix of Pearson correlation coefficients*.

	C_d	CL_r	Θ_{max}	*d*	Heading	Strength	Height	Biomass
C_d								
CL_r	0.47***							
Θ_{max}	-0.19	0.49***						
d	0.03	-0.30*	-0.20					
Heading	-0.33	-0.20	-0.20	0.15				
Strength	0.46***	0.91***	0.46**	-0.25	-0.16			
Height	0.13	-0.64***	-0.34*	0.46**	0.20	-0.52***		
Biomass	-0.27	-0.27	-0.13	0.12	0.66***	0.02	0.24	

*Signifiance. codes: 0 ‘***’ 0.001 ‘**’ 0.01 ‘*’ 0.05

Additional correlations emerging from video phenotyping could indicate a morphological basis for plant wind resistance. We detected a significant (p<0.001), positive relationship between total biomass and effective area at drag coefficient estimation (r = 0.54) across cultivars. The drag coefficient was positively correlated with increasing drag force at the

reference deformation ($p = 0.005$, $r = 0.46$). Finally, the sensitivity analysis revealed how a 25% increase in the parameter from its mean results in the following percent change in the response from its intercept value according to the phenotype's linear effect (Table 5).

Table 5. Sensitivity analysis relating a 25% increase in the phenotype of column 1 to changes in C_d and CL_r*

25% increase in phenotype	% Change in C_d	% Change in CL_r
Θ_{max}	-10.3	37.4***
d	-4.1	-15.9*
Heading	-18.5	-18.1
Strength	23.1***	29.8***
Height	-8.3	-19.8***
Biomass	-9.7	-12.8

*Significance Codes of the underlying correlation: 0 '***' 0.001 '**' 0.01 '*' 0.05

Discussion

Drag coefficients among cereal crops did not exhibit any significant variation in this experiment. The lack of significance indicates that the aerodynamic characteristic of individual plants are more significant than the various species, even within cultivars of a given cereal crop. Previous research indicates that grasses possess decreasing drag coefficients under increasing wind velocities as the plant deforms and streamlines its shape, with an additional effect of reducing the frontal area, as seen in fountain grass (Gillies et al 2002). The mean C_d (0.71) that we observed is greater than a previously reported drag coefficient for fountain grass, which ranged between 0.46 and 0.37 over similar Reynolds number values ($5x10^5 < R_e < 13x10^5$) as in our experiment (Gillies et al 2002). Our mean cereal C_d of 0.71 is also higher than those assumed in theoretical studies

on canopy airflow by (Finnigan and Muhlhearn I & II 1978). The significant relationship between increased stem strength and drag coefficient indicates that a higher velocity was required to achieve the reference deformation across the experiment, while increased leaf and stem biomass resulted in a greater effective area at the reference deformation that further increased the drag force. Stronger cereals are more likely to remain upright under wind stress (Berry et al 2003), which explains the positive correlation between stem strength and drag coefficient due to a stronger cereal's ability to be in equilibrium under increasing wind drag. A caveat of the C_d estimates is that not all were performed when the plant reached an equilibrium in the airstream, as the reference deformation was sometimes reached while wind speeds were accelerating in the wind tunnel and the stem angle decreasing. The single plants would have some momentum in this case, and as such forces acting would not be the same as measured using the load cell to obtain the strength measurement. The width of the 95% confidence interval (0.22) suggests that differences in C_d could be detected using our methods in single cereal plants on replicated germplasm. However, wide variation within crops for C_d likely implies physiological (i.e. stem strength or etiolation effects due to block position in the greenhouse) underpinnings rather than major differences in cereal foliage (apart from quantity as measured by biomass) that would alter the drag coefficient at the reference deformation.

While plant stem bending responses (as measured by CL_r and d) exhibited significant variation among the different cereal crops, both C_d and Θ_{max} revealed marked physiological dependency. The inverse relationship between CL_r and the modeled stem bending coefficient d confirms Grafius and Brown's (1954) findings, as more flexible

cereal stems are capable of resisting greater torque from wind induced drag. Additionally, the positive relationship between increased Θ_{max} and CL_r is indicative that more upright plants resist a greater proportion of the drag force on the stems. The positive relationship between CL_r and lodging resistance in the field has been noted previously among oat varieties: varieties resisting greater torque, exhibit lower lodging severity or root lodging angles (Grafius and Brown 1954; Frey and Norden 1959). Furthermore, the CLr was highly sensitive to stem strength and height. Taller cereals are known to lodge more and be weaker due to increased cell elongation and reduced lignin content (Crook and Ennos 1995; Peng et al 2014). Strength derived from stem curvature is optimal as it distributes the strain along the entire stem and not just at the base of the cereal, thereby increasing root lodging resistance (Grafius and Brown 1954). The positive relationship of C_d and *CLr* implies that a plant capable of resisting more torque on the stem will require a higher velocity to achieve a certain level of deformation yet is more capable of withstanding increased drag forces. Cereals with higher CL_r values would be expected to have a faster rate of bending recovery (measured in degrees per second) following wind exposure. Wheat had the highest average recovery of 5.2° at the end of the deceleration from 12 m/s wind speed (Table 4), with this rate of recovery significantly greater than the other cereal crops.

The differences in the observed plant bending parameters likely reflect material properties of the stem that enable resistance to wind stress. Material properties of plant stems include a cellulose-lignin-pectin polymer matrix, where lignin primarily confers flexibility and cellulose strength (Ma, 2009; Wang et al, 2006). In wheat, plots treated

with the gibberellin inhibitor paclobutrazol (reducing cell elongation) had stronger stems than untreated plots, likely due to greater lignin and cellulose concentrations within cells (Peng et al, 2014). In a comparative study across cereal crops, wheat stems were found to have 1% more lignin content than barley stems, while barely stems have 1% greater hemicellulose content (Sun et al 2002). Wheat stems also have 21% more lignin content in stems compared to oat in a separate comparative study (Thiago et al 1982). Among a subset of the varieties used in this experiment, wheat had significantly greater lignin content compared to oat varieties, while differences between wheat and 2- and 6-row barley varieties were not significant (Heuschele 2019, unpublished data). Wheat stems have additionally been shown in comparison to barley stems to have both lower young's moduli (a measurement of material stiffness) and increased breaking load per culm (Neenan and Spencer-Smith 1975), which would indicate a stronger, yet more flexible, stem for wheat relative to barley. Considering the sequential failure of lignin prior to cellulose within cell microfibrils, at which point the more rigid cellulose bears the stress, increasing lignin concentrations will improve flexibility and preserve the cellulose for bearing increased loads (Gangwar and Schillinger, 2019). Since stem strength and flexibility varies under controlled bending tests of stem segments, differences in stem composition and arrangement of microfibrils likely manifest as differences in stem bending under wind stress (Kono and Takahashi, 1964; Wang et al 2006; Gangwar and Schillinger, 2019). Higher lignin concentrations of wheat stems may therefore contribute to increased CL_r values and lower d coefficients that could confer increased root lodging resistance in the field.

Importantly, the single plant tests presented here to not fully correspond to field conditions that induce lodging. Cereal crops in nature are subjected to intermittent winds resulting from storm gusts and wind-canopy interactions, the latter associated with relatively high frequency experienced by oscillating crop as opposed to natural wind gusts (Finnigan 1978). This finding implies that the effective area, the drag coefficient, and the flow velocity vary constantly under field conditions, all contributing to significant temporal variability of the drag force. As stem bending response reveal an elastic behavior the study of crop lodging may require a structural dynamic approach based on the comparison between the natural frequency of the stem and the forcing frequency of the turbulent flow in the canopy mixing layer. Additional loading due to rainfall on the plant is possible and likely contributes to root lodging during severe weather (Zebrowski 1999). However, in the case of direct wind exposure, the standard deformation point (50° stem angle from the ground) examined represents a threshold at which root lodging is likely induced in the field by wind. Thus, the average drag coefficient for the tested cereals determined in this experiment can be assumed to represent a stem under severe, direct wind stress.

Given aerodynamic similarity, lodging resistant cereal ideotypes that are resilient in production environments where high winds and storms represent a serious risk to yields could be realized by improving bending responses under wind stress. Improving the ability of cereal stems to bend along their length as opposed to at the culm confers root lodging resistance by distributing the bending stress over more tissue, as opposed to localizing it at the base, where it is more likely to buckle and fail. The CL_r and d

measurements are reasonable quantifiers of stem deformation, with the former incorporating force measurements that can be approximated using an average drag coefficient measurement and an estimate of exposed area and wind speed. Though C_d values varied widely and are not significant among the major cereal crops tested here, reducing leaf and stem biomass could result in a lower drag force on cereal stems. Additional studies are needed that directly compare these bending phenotypes to stem material properties, whether relying on cereal variation or modification through applications of plant growth regulators to identify stem material compositions that resist known drag forces. A further understanding of stem compositional traits that lead to a flexible, strong stem could enable molecular marker-based selection for stem flexibility in breeding populations without the need for repeated phenotyping. This wind tunnel experiment on the major cereal crops has uncovered substantial variation for phenotypes of stem bending and physiological correlates. That said, breeders should focus on reducing leaf and stem biomass, increasing stem strength, and improving stem bending characteristics to enable cereals to withstand the forces induced by direct wind exposure and improve root lodging resistance.

Figures

Figure 1. Video derived phenotypes. Unmasked frame (1), masked plant (2), windward edge with fitted power curve (3), fixed *x* distance where half length of stem *h* makes a 50° angle with wind tunnel base (4), *f(x)* along the fitted curve (5), bending angle Θ at any frame (6), effective area for drag coefficient estimation (7).

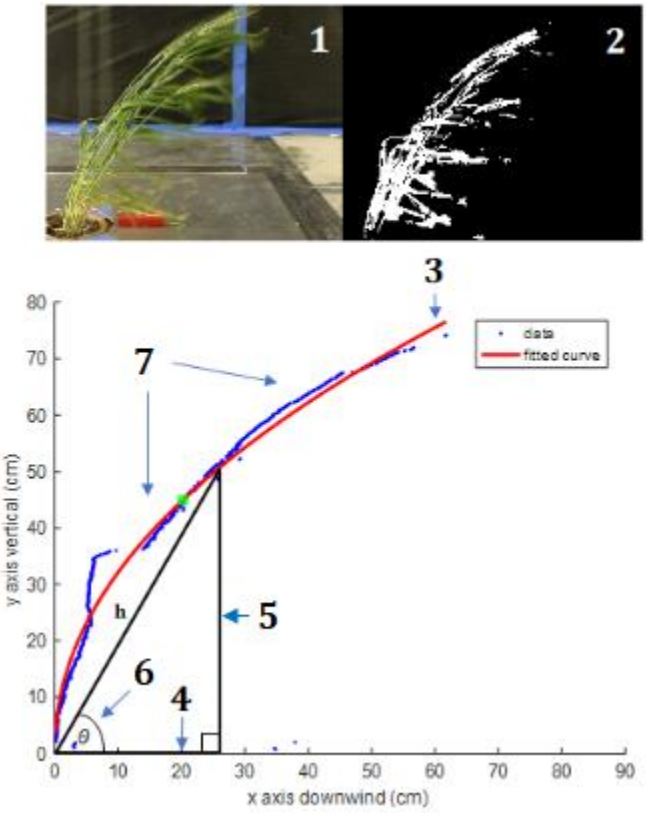

Figure 2. CL_r measurement diagram with schematics outlining components of CL_r estimation at the reference deformation (Θ = 50°) from video frames representing a cereal with a near-zero CL_r (A) and a CL_r that is much greater than 0 (B). Figure adapted from Grafius and Brown (1954).

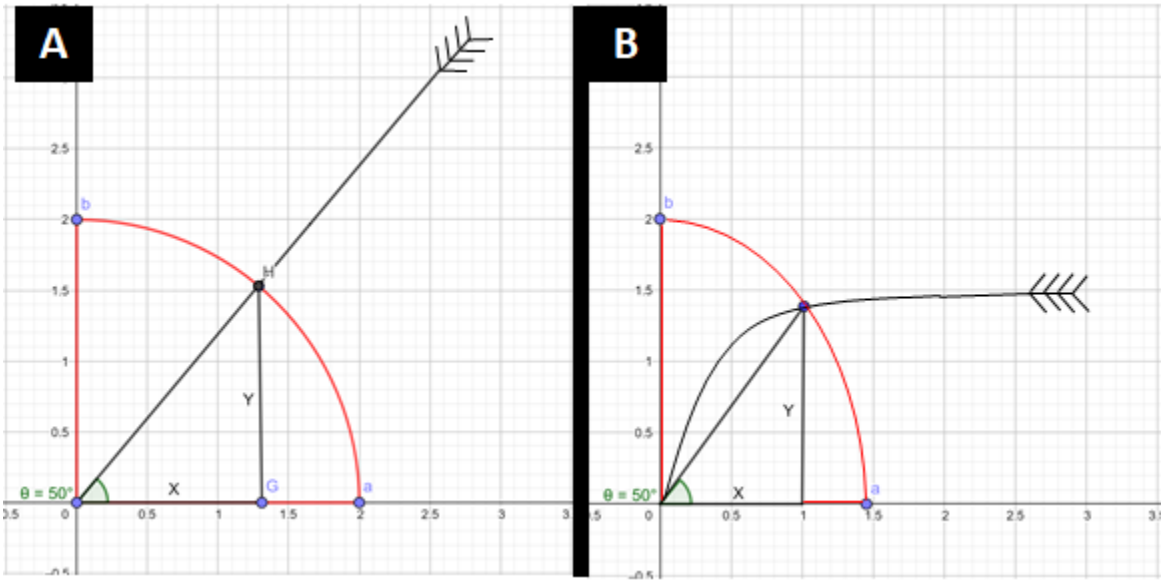

Figure 3. Average Θ by crop over the wind tunnel test. 95% Confidence intervals around the mean are shown.

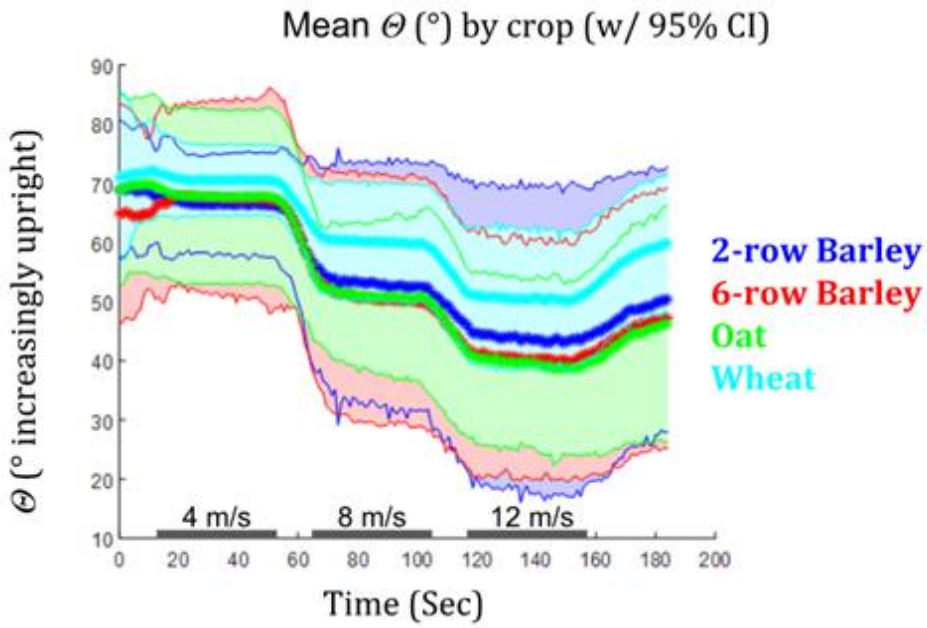

Chapter 5:

Oscillating frequencies of cereal stems, products of windspeed and morphology, are indicative of root lodging resistance[*]

Alexander Q. Susko[1], D. Jo Heuschele[1], and Kevin P. Smith[1]

[1]University of Minnesota Department of Agronomy and Plant Genetics

411 Borlaug Hall, 1991 Upper Buford Circle, St. Paul, MN, USA, 55108

[*] AQS conceived of the research in this chapter, constructed the camera system, obtained the data, performed the analyses, and wrote the manuscript. DJH provided substantial manuscript edits and technical advice. KPS served as the principal investigator

Introduction

Lodging, or the failure of plant stems under high winds, contributes substantial yield losses in cereal crops (Weibel and Pendleton, 1964). Lodging in cereal crops can manifest as either stem breakage, where the stem breaks at the midpoint along the stem or higher, or as root lodging, where the stem buckles at the base of the plant. Prior to lodging, cereal crops experience movement in the wind. There exists variation of cereal crop movement in the wind which is not captured in the final lodging outcome, and thus is of interest to studying over a growing season across the life of a cereal crop (Berry et al, 2006; Chapter 3). Understanding the relationship between plant structures, movement in the wind, and lodging outcomes could provide insights into breeding targets for lodging resistance during the most susceptible phases of cereal growth and development.

Individual plant stems can be physically modeled as a vibrating system that oscillates back and forth at a natural frequency when excited by the wind. This oscillating frequency can be thought of as a consequence of morphological and environmental factors combining to produce a pattern of plant movement. In framing cereal lodging as a vibration problem, morphological or physiological variables that influence plant-wind interactions can be identified to better understand the complex problem of lodging resistance. At a basic level, the natural frequency is equivalent to the square root of the ratio of stem stiffness to stem mass per unit length (Flesch and Grant, 1991). This implies that stronger stems oscillate at a higher frequency, and heavier stems at a lower frequency, with incremental changes to either affecting the natural frequency in a non-linear fashion. Because stems are only fixed at the culm, the movement equation becomes

more complicated, involving structural and aerodynamic damping coefficients, stem area exposed, and other parameters (Flesch and Grant, 1991; Baker, 1995; DeLangre, 2008). An interpretation of the previously cited work is that increasing wind velocity will induce a drag force and effectively the mass per unit length which, holding other parameters constant, will decrease the frequency of oscillation. If the plant stem cannot resist these drag forces, root lodging will occur over multiple oscillations (Baker, 1995). As such, a plant with morphological or physiological properties to counteract these drag forces would be expected to dampen these oscillations and possess a higher frequency of oscillation, even under high winds, and should prove more lodging resistant.

Both theoretical and applied research exists on plant stem oscillations. Original descriptions of interlocking grain waves (honami) theoretically describe the interdependence of gust and plant natural frequencies on sustaining plant movement in uniform cereal canopies (Inoue, 1955). Subsequent empirical work has estimated the gust frequencies needed to induce honami at around 0.35 Hz across a uniform wheat canopy (Finnigan, 1979). Early modeling uniform wheat canopies in a wind tunnel discerned a primary natural frequency for model wheat stems by analyzing acoustic signals obtained from a microphone mounted beneath a synthetic wheat canopy (Finnigan and Mulhearn, 1978). At the individual plant level, models have been developed to determine the lodging tolerances of wheat and barley, namely how changing morphological properties such as stem strength, diameters alter the failure velocity needed to induce lodging (Berry et al, 2006; Berry et al, 2007). Together, such studies

have generated a strong theoretical background on plant movement and lodging resistance.

Development of image-based plant phenotyping methods have enabled quantification of novel plant traits on scales not previously attainable (Araus and Cairns, 2014). Existing methods to determine plant natural frequency consists of manually timing plant oscillations after pulling and releasing cereal stems (Berry et al, 2004). Unlike natural winds, this method applies a similar force to each cereal plant (assuming consistency in pulling by the researcher), but it is not easily scaled to large field experiments. The quantification of plant movement via color changes in a video, including the natural frequency and amplitude of single row plots, is possible and enables systematic quantification of multiple crops, cultivars, or planting dates (Chapter 2, Chapter 3). This method further employs signal processing as a method for systematically estimating plant natural frequencies in the field, allowing for the repeated quantification of plant movement via color changes in video footage of cereal canopies under natural winds. Over a long observation window encompassing varying wind speeds, trends should emerge about the physiology of plant movement that are detectable even in the presence of windspeed changes that also influence the natural stem oscillation.

The primary goal of this study is therefore to elucidate relationships between plant movement, plant structure, and root lodging outcomes over a growing season for cereal crops in standard randomized complete block design with repeated measures over a growing season. We accomplish this via the following objectives: 1) identifying crop and

cultivar level phenotypic differences after accounting for repeated measures in the randomized complete block design within major growth stages 2) relating plant structural traits to movement and lodging outcomes within major growth stages and 3) examining movement, lodging outcomes, and plant structural traits as differentiators of total phenotypic variation across major cereal crops.

Materials and Methods

Field Design. The experiment was carried out on cereal cultivars planted a randomized complete block (RCB) design in summer 2018. The design contained four cultivars of four different cereal grains (Table 1) for a total of 16 cultivars.

Table 1. Cultivars used in the lodging field design.

Latin Name	Crop	Cultivars
Avena sativa L.	oat	'Gopher', IL078721,ND021052, 'Reins'
Hordeum vulgare L.	2-row barley	'AC Metcalf', 'Conlon', 'ND Genesis', 'Pinnacle'
Hordeum vulgare L.	6-row barley	'Celebration','Quest','Stellar','Tradition'
Triticum aestivum L.	wheat	'Linkert',MN113946,'Rollag','Shelly'

Cereal cultivars were planted in single row plots (hereafter referred to as plots) of 3.04m in length with 30cm spacing between rows with a north-south lengthwise orientation. A row of winter wheat separated each cereal plot used in the study. Each cultivar was replicated 8 times in separate blocks, with an automatable camera system bisecting the 4th and 5th blocks down the middle of the field. More details on the automatable camera system construction and camera specifications can be seen (Chapter 2, Chapter 3). Furthermore, this design was planted at four different planting dates (30 Apr, 7 May, 15

May, and 22 May 2018) in adjacent regions of the field. Average wind speed, gust, and direction data were obtained for each video date from the Minnesota DNR Mesonet station located adjacent to the lodging study of the Minnesota Agricultural Experiment Station in St. Paul, MN.

Data Collection. Imaging (video) data of plant movement on each plot was captured on 11 different days during June and July 2018 under varying windspeeds (Table 2).

Table 2. Average wind speeds and directions on each video date†

Video Date	Avg. Wind Speed m s^{-1}	Avg. Wind Gust m s^{-1}	Avg. Direction °
11 Jun 2018	5.6	11.2	122
14 Jun 2018	4.8	9.2	129
15 Jun 2018	3.5	6.1	146
20 Jun 2018	3.6	6.3	58
21 Jun 2018	2.6	4.9	81
25 Jun 2018	4.7	7.7	142
28 Jun 2018	2.6	6.2	190
29 Jun 2018	3.6	7.5	169
2 Jul 2018	3.2	5.4	231
9 Jul 2018	2.1	4	247
16 Jul 2018	2.6	5.2	299

†Wind speed and directions averaged within the 30 minute window of video imaging at each date

The camera system with mounted 360fly 4k hemispherical camera (360fly, Inc) captured 2 min 30 sec videos (at 30 fps) of plant movement at each of the 8 panels, with 2 panels placed in each of the four planting dates (Chapter 2). The camera imaged 64 plots within each planting date (encompassing two videos per planting date) across 4 of the 8 blocks. Briefly, analysis of videos to quantify plant movement was done on a frame by

frame basis, with the panel in view of each video used to orient the field design such that square foot regions of the plot canopy were mapped from cartesian (x,y) coordinates to spherical coordinates (latitude, longitude), and then from spherical coordinates to indexed pixels within the RGB frame. The average color value of the red channel for each plot over all frames were treated as a time varying signal of plant movement, from which we derived mean frequency (Hz) and total amplitude. Amplitude was expressed in decibels (dB min, $10*\log_{10}(n/0.0001)$) in reference to an assigned minimum raw amplitude value (0.0001) substituted for 0 within 0.2 Hz frequency bins for each plot at each of the 11 video dates. More details on the video analysis and measurement of plant movement can be seen (Chapter 3). We collected 2,688 plot observations of plant movement over all of the video dates, as the 11 Jun 2018 video date only contained imaging of the 30 Apr and 7 May planting dates. At each video date-planting date combination, we quantified the spatial autocorrelation of mean frequency and amplitude in the 0.9-1.1 Hz frequency bin over plots via a Moran's I test with a pseudo p-value determined using 999 Monte Carlo simulations implemented in the R package spdep.

Morphological data collection occurred once per week for each planting date, beginning 11 Jun 2018 and ending 16 Jul 2018. We collected plant height measured from the base of the plant to its highest natural point, the diameter of the internode between nodes 2 and 3 (known as internode 23), and the diameter of the internode between nodes 5 and 6 (known as internode 56). If internode 56 was not present in the early growth stages, the diameter of the uppermost available internode was used. A digital caliper was used to quantify diameter measurements. We took 3 measurements of each

morphological trait per plot, and averaged them to get a plot mean. Since video data was taken on dates where specific plots were not measured, we interpolated the morphological trait values for those dates based on the slope between the two nearest measurement times. This trait interpolation and concatenation of values at every video date was accomplished using the interpolation.r script.

Root lodging was naturally induced across the first three planting dates (30 Apr, 7 May, and 15 May) following a thunderstorm on 1 Jul 2018, which briefly sustained 14.6 m/s winds and dropped 3.1 cm of rain in one hour. Root lodging was quantified on 2 Jul 2018 by measuring the angle of the stems (Uprightness angle) with respect to the ground (with 90 degrees being fully upright) at three points per plot and then obtaining a plot average. Autocorrelation of lodging angle values were calculated for the first three planting dates using the Moran's I method described above.

Data analysis. Plot observations were grouped by growth stage (tillering, elongation, heading, dough, and maturity) based on accumulated growing degree days (GDD) above 32°F until a given measurement time for plant movement, physiological trait, or lodging using an online calculator (http://www.nutrien-ekonomics.com/tools-to-calculate-fertilizer-needs/calculators/gdd/). The same GDD defined stages were used for each cereal, which represented an average among oat, wheat, and barley as defined previously (Table 3) (Miller et al, 2001).

Table 3. GDD32 demarcated physiological growth stages

Growth Stage	N observations	Accumulated GDD32 range	Definition
Tillering	124	<940	Tillers visible on seedling
Elongation	743	940 to 1484	1st node visible on stems
Heading	1183	1484 to 2145	Panicle emerges from boot, pollination follows
Dough	562	2145 to 2600	Grain begins filling, endosperm contents transition from liquid to dough
Maturity	188	>2600	Grain contents harden, leaves senesce

Statistical analyses on the relationships between plant movement, plant physiology, and root lodging outcome were conducted within each growth stage. First, we analyzed whether a significant crop effect for mean frequency existed after accounting for the repeated measures at each plot with video date and genotype (cultivar or crop) as fixed effects, position (blocking factor) of the plot from the camera nested within planting date as a random effect, and errors distributed as a standard autoregressive covariance matrix in time. This was accomplished using a mixed effects model with random effects of position from camera nested within an imaging panel and correlation structure corAR1() to account for repeated measures across video dates. Phenotypic means at each growth stage were predicted for each cultivar and crop using the r package predictmeans from the mixed effect model output, with an LSD test using an fdr p-value correction to assess significance.

We visualized the total amount of plant movement (amplitude in dB) at 0.2 Hz frequency bins for each plot in a 3D plot referred to as a resonance landscape. The amplitude of plant movement was plotted in a 3D scatter for each growth stage, with the

mean frequency of the plot on the x axis, the 0.2 Hz frequency bin on the y axis, and the total movement (in dB) on the z axis. Resonance landscapes were generated for observations from each of the five growth stages.

Using an ANOVA on the linear mixed model previously describe, we analyzed the genotypic effect for the morphological traits of height, int23 diameter, and int23.56 diameter ratio and subsequent predicted means. We also analyzed whether morphological variables correlated with movement data within each growth stage. Correlations of mean frequency and lodging angle with morphological traits with each growth stage were performed via a linear model with the morphological trait as the independent variable with a calculated Pearson correlation coefficient. Video date information is provided in the scatterplots as a color coding of points to better visualize a video date effect at specific correlations if present.

The total variation for movement, physiology, and lodging was examined using principal component analysis (PCA) at both the crop and within crop level to examine the relative direction and magnitude of each variable as a differentiator of the total variation. Within crops, PCA analysis were further broken down using additive linear models to examine the relatedness of variables across crops for establishing morphological relationships between plant movement, plant physiology, and root lodging outcomes within oat, wheat, and barley.

Results

Plant Movement Variation. While Morans I values at each planting-video date combination occasionally revealed significant spatial autocorrelation, mean frequency

and amplitude values did not cluster at most planting or video dates with regularity (Appendix VI, Supplemental Tables S1,S2) (Appendix VI, Supplemental Figures S1,S2). Variation from the LME model revealed a significant line effect in the tillering stage (p=0.01) and the elongation stage (p=0.008) (Figure 1, Table 4), while a significant crop effect was observed for the elongation stage as well (p = 0.02) (Figure 1, Table 4).

Table 4. Predicted means of mean frequency (Hz) by line and crop and for each growth stage.

Genotype	Tillering†	Elongation†‡	Heading	Dough	Maturity
'Gopher'	1.21B*	1.63	1.43	1.43	1.64
IL078721	1.29AB	1.50	1.42	1.38	1.43
ND021052	1.52A	1.64	1.43	1.47	1.46
'Reins'	1.26AB	1.67	1.52	1.49	1.58
'AC Metcalf'	1.32AB	1.55	1.49	1.43	1.52
'Conlon'	1.35AB	1.67	1.47	1.45	1.52
'ND Genesis'	1.19B	1.71	1.53	1.44	1.61
'Pinnacle'	1.28AB	1.55	1.48	1.41	1.42
'Celebration'	1.35AB	1.62	1.40	1.39	1.41
'Quest'	1.31AB	1.54	1.47	1.44	1.54
'Stellar ND'	1.23AB	1.58	1.47	1.43	1.57
'Tradition'	1.13B	1.51	1.50	1.49	1.57
'Linkert'	1.37AB	1.62	1.55	1.52	1.47
MN113946	1.36AB	1.71	1.48	1.50	1.58
'Rollag'	1.31AB	1.65	1.44	1.47	1.53
'Shelly'	1.33AB	1.71	1.49	1.46	1.39
Oat	1.32	1.61AB	1.45	1.45	1.53
2-row Barley	1.29	1.61AB	1.50	1.43	1.51
6-row Barley	1.27	1.57B	1.46	1.44	1.53
Wheat	1.34	1.68A	1.49	1.49	1.49

†indicates a that the cultivar genotypic effect was observed in the growth stage according to the LME model

‡indicates a that the crop genotypic effect was observed in the growth stage according to the LME model

*Unique letters indicate significantly different means at alpha = 0.05

Video date effects were significant ($p < 0.001$) across all growth stages except at maturity ($p = 0.96$) (Figure 1). Generally, video dates with the lowest mean frequencies across plots possessed the highest windspeeds (Figure 1, Table 2). The amount of movement at each plot in a given frequency bin varied over all observations at each of the five growth stages. The resonance landscapes; 3D plots of the mean frequency (x axis), 0.2 Hz frequency bins (y axis), and the amount of movement within each frequency bin in dB (z axis) for each cereal growth stage, revealed a shift towards plots of higher frequency and lower amplitude with increasing maturity, as well as peak movement at the heading and dough stages (Figure 2).

Plant Morphology, Lodging Variation. An ANOVA of LME variation revealed significant crop, video date, and crop by video date interaction effects across all growth stages ($p < 0.001$) for height, internode 23 diameter, and internode23:56 ratio. Height was maximized in all cereals by the dough stage, while oat contained the most variation in height while also having the highest mean height of the cereal crops at the dough and maturity stages (Figure 3A, Appendix VI Supplemental Table 3). Internode 23 diameter was maximized in the elongation stage for all cereals, with 6 row barley containing stems with the widest internode 23 diameters through the heading stage (Figure 3B, Supplemental Table S4). Wheat stem internode 23 diameters were the lowest throughout the growth stages on average (Appendix VI, Supplemental Table S4). Internode 23.56

ratios were higher in 2row, 6row, and oat compared to wheat, which possessed less stem tapering on average (Figure 3C) (Appendix VI, Supplemental Table S5). Internode 23.56 ratios remained close to 1 through the heading stage, when the diameter of internode 5-6 remained large prior to the panicle emerging from the boot (Appendix VI, Supplemental Table S5). Additionally, there was a significant positive relationship ($R^2 = 0.36$, $p<0.001$) between int23 diameter and and stem wet mass during a measurement on planting dates 1 and 2 on 27 Jun 2018. An increase in stem diameter of 1mm conferred 7.2g of additional stem mass on average.

The storm on 1 Jul 2018 induced a variable amount of lodging in the first three planting dates. Average lodging angles in each plot were not spatially autocorrelated at any planting date according to a Moran's I test (Appendix VI, Supplemental Figure S3). ANOVAs of both Crop and line variation were significant ($p <0.001$), with wheat being significantly more upright than the other cereal crops on average (Table 5)

Table 5. Average root lodging uprightness angle by cultivar and crop

Genotype	Uprightness Angle
'Gopher'	74.01^{fghi*}
IL078721	82.14^{bcd}
ND021052	80.76^{cde}
'Reins'	78.07^{defg}
'AC Metcalf'	70.68^{ij}
'Conlon'	66.93^{j}
'ND Genesis'	72.97^{ghi}
'Pinnacle'	79.38^{def}
'Celebration'	71.39^{hij}
'Quest'	69.69^{ij}
'Stellar ND'	76.41^{efgh}
'Tradition'	73.28^{ghi}

‘Linkert’	88.89[a]
MN113946	86.09[abc]
‘Rollag’	88.07[a]
‘Shelly’	86.46[ab]
Oat	78.74[b]
2-row Barley	72.48[c]
6-row Barley	72.69[c]
Wheat	87.37[a]

*Unique letters indicate significantly different means at alpha = 0.05

Relationships of lodging, plant movement, and morphology

Correlations of physical traits with movement were most significant in the elongation phase, while only heading was significant in the heading phase (Table 6).

Table 6. Pearson correlation coefficients for movement or lodging and morphology relationships by growth stage †

Relationship	Tillering	Elongation	Heading	Dough	Maturity
Freq~Height	-0.04	-0.095*	-0.044	-0.01	0.02
Freq~Heading	-0.044	0.134***	0.25***	0.077	-0.02
log(Freq)~Int23	-0.02	-0.03*	-0.02	-0.02	-0.01
log(Freq)~Int23:56	-0.02	-0.11***	0.03	0.06	0.02
Angle~Height	NA	-0.61***	-0.44***	NA	NA
Angle~Heading	NA	0.42***	0.35***	NA	NA
Angle~Int23	NA	-0.33***	-0.17***	NA	NA
Angle~Int23:56	NA	-0.03*	-0.28***	NA	NA
Angle~Freq	NA	0.14***	0.1***	NA	NA

†Significance. codes: 0 ‘***’ 0.001 ‘**’ 0.01 ‘*’ 0.05

Correlations of physical traits with uprightness angle in the elongation, heading phases where lodging was measured were stronger than for mean frequency (Table 6). Correlations are shown with points color coded by the average windspeed on the video

date where they were taken (Appendix VI, Supplemental Figure S4). For elongation and heading phases where root lodging was observed, uprightness angle was a strong differentiator of total crop variation and remained orthogonal to height for both stages (Figure 4 A-B). For dough and maturity stages where root lodging was not observed, height remained orthogonal to heading, with amplitude at 0.9 Hz increasing in magnitude at maturity and paralleling heading (Figure 4 C-D).

Movement as a differentiator of total variation within crops. The significant correlation between heading date and mean frequency in both the elongation and heading stages across cereals implies a physiological underpinning to mean frequency (Table 4). Furthermore, the significant positive relationship between mean frequency and lodging angle, as well as heading date and uprightness angle, could be partially explained by a physiological change that occurs with increased heading date that manifests as a higher frequency of stem oscillation. And while uprightness angle is consistently orthogonal to height within crops in the elongation stage, the heading date loading parallels lodging angle strongly in wheat and to a lesser extent in 2- and 6-row barley, while these loadings opposite in oat (Appendix VI, Supplemental Figure S5).

This led to further examination of the relationship between mean frequency and heading date in the different cereal crops over a narrower range heights encompassing the elongation and heading phases, or observations in the 25th-50th percentiles for height within each crop. Across all crops and growth stages in general, increased heading date had a significant negative correlation ($r = -0.51$) with plant height at the last time of measurement (measured 16 Jul 2018), with each additional day until heading decreasing

height by 0.22 cm on average. This height variation was included in a linear model along with heading date with the response variable of mean frequency for each plot. There was a significant positive correlation between heading and mean frequency within each cereal crop, with each day of heading date conferring mean frequency increases of 0.04 Hz in oat, 0.02 Hz in wheat, and 0.03 Hz in 2- and 6- row barley (Figure 5A-D). Unlike mean frequency and heading date, the dependence of mean frequency on height variation was not consistent among cereal crops. In oat, there was no relationship between height and mean frequency in this range, while in wheat each centimeter of height decreased the mean frequency by 0.02 Hz (Figure 5A-B). This relationship was significant for 6-row barley as well where each centimeter of height decreased mean frequency by 0.015 Hz, while the negative relationship between height and mean frequency was insignificant for 2-row Barley (Figure 5C-D). These trends were observed despite differences in average windspeeds on these dates where frequency data was obtained, and point to crop-specific mechanisms that increase the mean frequency of a stem as a consequence of later heading dates.

Discussion

Root lodging in cereal crops is a complex problem that stems from plant-wind interactions. A clear challenge to elucidating a physiological basis for plant-wind interactions are the environmental components: namely the dependence of plant movement on wind speed and the tendency of moving plants interacting with gusts to generate and amplify air currents (Inhoue, 1955; Finnigan 1979; Flesh and Grant, 1991). While plant movement depends both on plant structures and the wind, the

randomization of cereal plots in this experiment in theory produces a layer of varying windspeeds at canopy height that is less likely amplify over cereals of varying heights and natural frequencies. Thus, this experimental design is well suited to elucidating physiology-movement relationships, as the prevailing windspeeds on a given date would have a large effect on movement patterns observed at an individual plot level without inducing neighbor effects. This is evidenced in the lack of significant spatial autocorrelation for mean frequency and 0.9-1.1 Hz amplitude values at most video dates, indicating that movement patterns were not correlated within planting dates. Exceptions to this trend appear to be instances where wind speed varied among the two videos taken at each planting date, producing spatial autocorrelation of mean frequency and amplitude values (video dates 9 Jul, 16 Jul 2018). The video date effect was universally significant on the mean frequency of plant movement and also for the amplitude due to the higher drag forces induced on the plant tissues that reduced the frequency of oscillation (Flesh and Grant, 1991; Zebrowski, 1999). Despite the strong video date effect, the significance of a cultivar and crop effect existence of trends within growth stages points to a physiological basis for plant movement as well, and the relationship between increased oscillation frequency and lodging resistance indicates that stems with higher frequency manifest traits that are important to root lodging resistance in cereals.

Another challenge to elucidating plant-wind interactions is that lodging resistance varies (presumably along with movement-morphology relationships) depending on cereal growth stages. Cereals are not equally susceptible to root lodging at all times in growth, with the most yield losses and lack of recovery occurring early in the dough stage

following complete heading and anthesis (Jedel and Helm, 1991; Kelbert et al, 2004). Thus, separating by growth stage reveals important differences in both plant movement and lodging susceptibility over time. Amounts of plant movement were maximized in the 0.9 - 1.1 Hz frequency bin at the heading stage and to a similar degree in the dough stage despite the aggregation of data from multiple video dates. The maximized amplitude of oscillations across cereal cultivars and crops in this experiment is indicative of increased fatigue at the base of the stem via, contributing increased stressed that can lead to root lodging (Baker, 1995). Stem sway periods in cereals have been shown to increase exponentially with incremental increases in mass on the stem tip, and as such post anthesis depression of the natural frequency and increase in amplitude is consistent (Zebrowski, 1999). Similarly, the mass of the stem, proximally measured via the internode 23 diameter, weakly decreased the mean frequency in the elongation stage but more substantially decreased the uprightness angle. A study focusing on wheat cultivars identified stem diameters (1mm) had a much greater root lodging risk (99%) compared to large stem diameters (3mm) (3%), the look across crops within this study suggests that stem width is not universally affecting natural frequency or lodging outcome across cereals (Baker et al, 1998). Increased stem mass, without changes in stem composition that confer additional strength or flexibility, could contribute to reduced natural frequencies and worse lodging outcomes in the elongation and heading stages.

Weak correlations of morphology with movement are expected given the large video date effect observed, principally stemming from varying windspeeds and drag forces that influence stem natural frequencies (Flesch and Grant, 1991). Relationships

between morphology and uprightness angle were much stronger than those for movement in the elongation and heading stages. The strength of the correlations between morphological variables and uprightness angle in the elongation and heading stages are notable also in their direction with respect to mean oscillating frequency: increasing plant height led to both decreased mean frequency and lower uprightness angles, while increasing the heading date led to an increase in mean frequency and uprightness angle. Height has been observed by many cereal studies to increase the root lodging angle or severity (cite agronomic sources), with a raised center of gravity depressing frequency of oscillation drag (Berry et al, 2000). Furthermore, taller cereals that cannot bend along their length will both be exposed to higher drag forces and greater leverage for those forces, further straining the culm and base of the stem (Grafius and Brown, 1954; Baker 1995).

Controlling for variation in height for observations in the elongation and heading stages for each cereal crop revealed differences in the dependency of height on mean frequency across observations from the different planting dates. Given that later planting dates were shorter on average across all cereals, there existed a physiological impact of later planting. This height reduction is likely due to increased high temperature stress, which results in reduced height in cool season cereals (Irfan et al, 2005). But given that natural frequency is a manifestation of height and other stem properties, controlling for height in the elongation and heading stages can hint at whether a stem material change, separate from height, manifested at a later planting date. The lack of dependence on height in oat for observations in the elongation and heading stages on mean frequency

indicates that mean frequency is not dependent on height in oat at these growth stages, but rather the heading date (planting date) conferring some change to the stem. Conversely, the significant dependence of height and mean frequency in wheat for the elongation and heading stages implies that the same mechanisms of later planting that reduce height are present, but that the mechanism that increases mean oscillating frequency while controlling for variation in height is not present in wheat. Barley fell between oat and wheat for this phenomenon, with 6-row possessing this significant dependence of height and mean frequency over these growth stages while 2-row did not. Within crops, frequency observations did not cluster by video date, indicating that these changes were strong enough to be detected regardless of windspeed (Figure 5). This implies a stem physiological change in oat whereby a stem of the same height, planted later, is different enough to influence the oscillating frequency, while this mechanism is absent in wheat. Shorter wheat stems have a reduced center of gravity and thus a higher natural frequency (Berry et al, 2000). Thus, the mechanism by which oat increases its natural frequency can happen in spite of an unaltered center of gravity, likely by altering stem stiffness through a physiological change.

Cereals that oscillated at a higher frequency had greater uprightness angles on average in the elongation and heading stages, encompassing data collected over varying windspeeds and planting dates. A high frequency of oscillation indicates increased stem stiffness, and an ability to better resist torque applied due to drag forces (Grafius and Brown, 1954; Flesch and Grant, 1991). In a parametric analysis of wheat lodging parameters, an increase in the natural frequency from 0.5Hz to 1.5Hz in wheat

corresponded to a wheat lodging reduction from 93% to 11% (Baker et al, 1998). Similarly, a reduction in the plants center of gravity (height proxy) from 80 cm to 20cm above the ground resulted in a reduced lodging risk from 70% to 3 % (Baker et al, 1998). In comparing the natural frequencies of wheat and barley cultivars, the winter wheat cultivars had natural frequencies of 1 and 1.01 Hz, while spring barley cultivars had 0.67 and 0.60 Hz following anthesis (Berry et al, 2006). In the cited study, winter wheat cultivars had a flexural rigidity (force required to bend a stem to a predefined curvature) that was nearly 5 times that of the spring barley, indicating a greater resistance by wheat stems to the bending forces. In a separate study, the authors quantified the coefficient of lodging resistance CLr (Grafius and Brown, 1954) for the cereal cultivars used in this study in a wind tunnel, with wheat cultivars possessing significantly greater CLr values than barley or oat (Chapter 4). The ability of wheat stems to better resist bending forces could lead to their increased natural frequencies in prior studies and in the elongation stage here, as well as to the increased uprightness angles observed in this study.

While genotypic differences exist for mean frequency, the phenomenon can be altered through the application of plant growth regulators (PGRs) or through management practices. Both reduced nitrogen conditions and applications of the PGRS Cycocel and Terpal reduced plant height and increased the natural frequency in wheat (Berry et al, 2000). Increased nitrogen has been shown to both increase the height and decrease strength of wheat, while application of the PGRs chlormequat and mepiquat chloride did not affect stem strength (Crook and Ennos, 1995). Hormonal regulation of stem elongation prior to heading is likely affected at later planting dates through some amount

of heat stress (Irfan et al, 2005). The tendency of oat stems to possess increased mean frequency while experiencing increased heat intensity via a later planting date at the critical elongation and heading growth stages could therefore have a hormonal basis. The induction of a higher natural frequency in oat by a later planting should be better understood, so as to induce it in other cereals without using later planting dates that reduce yields.

Despite the large effect of video date on aspects of plant movement, the emergent trends discovered in this season-long study capture trends in the relationships between morphological variables, plant movement and root lodging. These trends are consistent with the physical models of crop lodging and continue to offer targets for developing cereal ideotypes that are resistant to root lodging. A cereal with increased root lodging resistance necessitates having shorter, lighter stems and stem material properties that confer a higher oscillating frequency to minimize excitation by gusts in the field.

Figures

Figure 1. Boxplots of cultivar (A) and video date (B) variation in mean frequency. Cultivar boxplots are colored by cereal crop: cyan (oat), salmon (2-row), green (6-row), and purple (wheat).

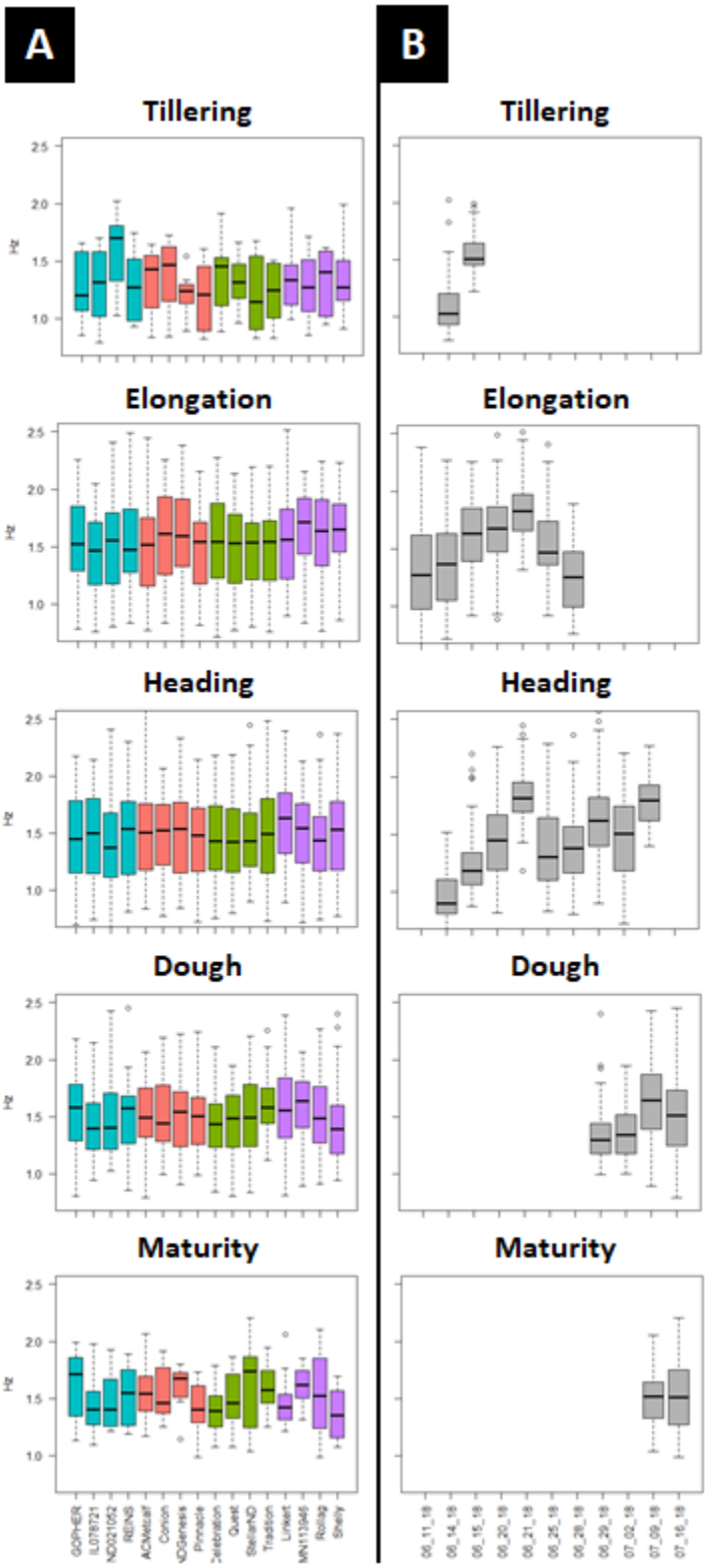
A
B
Tillering
Elongation
Heading
Dough
Maturity
Hz
2.5
2.0
1.5
1.0
GDPHER
IL0787121
ND0221052
REINS
ACNetcarf
Conon
KDGeneers
Pinnacle
Celebration
Quest
StellarND
Tradition
Linkert
MN1133446
Rollag
Shelly
06_11_18
06_14_18
06_15_18
06_20_18
06_21_18
06_25_18
06_28_18
06_29_18
07_02_18
07_09_18
07_16_18

Figure 2. Resonance landscapes of cereal movement by growth stage.

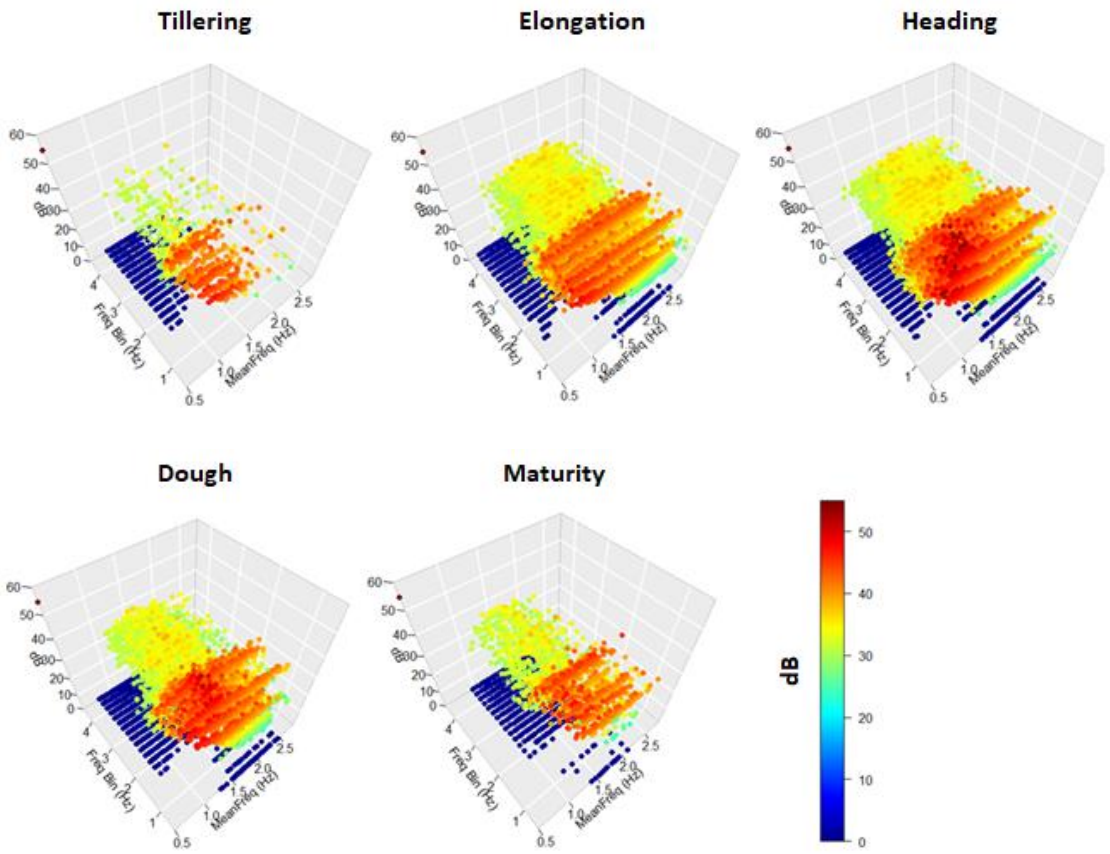

Figure 3. Lattice boxpots by crop, growth stage for height (A), internode 23 diameter (B), and internode 23:56 diameter ratio (C).

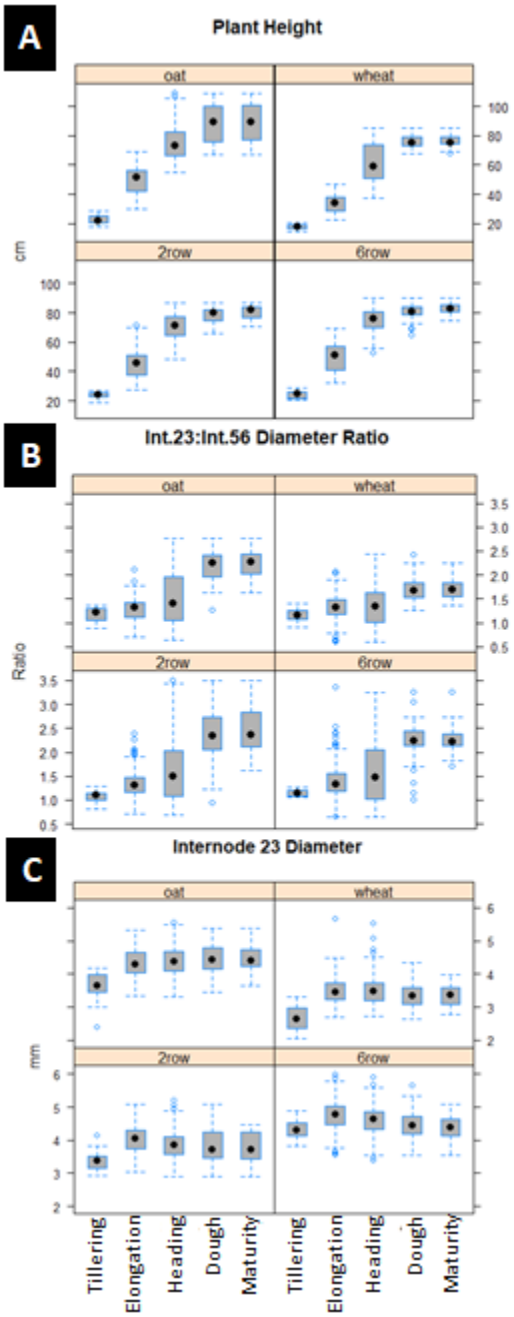

Figure 4. PCA plots by growth stage showing the magnitude and direction of variables, with points color coded by crop: cyan (oat), salmon (2-row barley), green (6-row barley), and purple (wheat).

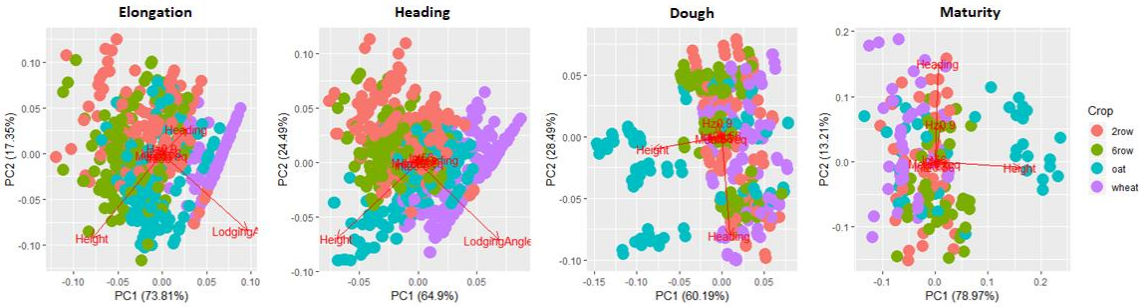

Figure 5. Scatterplots of heading, height, mean frequency relationships by crop between plots of 25-50th height percentile. Points are color coded by the wind speed on the date of each observation, with a trendline shown if the correlation is significant at alpha = 0.05.

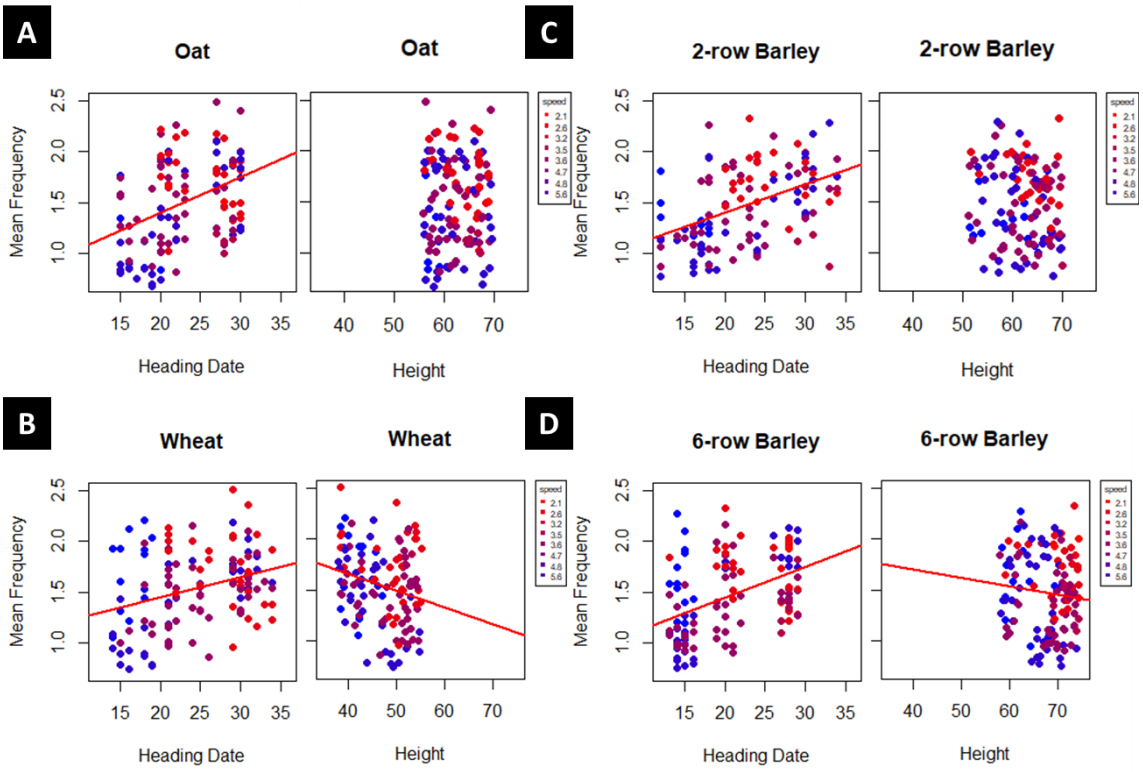

Chapter 6:

The genetics of oat lodging resistance and related agronomic traits[*]

Alexander Q. Susko[1], D. Jo Heuschele[1], Ian McNish[1], and Kevin P. Smith[1].

[1]University of Minnesota Department of Agronomy and Plant Genetics, 411 Borlaug Hall, 1991 Upper Buford Circle, St. Paul, MN 55108

[*] AQS conceived of the research in this chapter, collected the field data, conducted the analyses and wrote the manuscript. DJH and IM contributed technical expertise towards data analysis, while KPS served as principal investigator.

Introduction

Oat (Avena sativa L.) is an allohexaploid, self-pollinating cereal grain. The genus Avena contains five cultivated species and 17 wild species, whose center of diversity spans the Mediterranean basin east to Asia Minor (Moore-Colyer, 1995). Prior to domestication of A. sativa, humans in the Jordan River Valley were cultivating wild oat (Avena sterilis L.) as early as 11,400 years before present (BP) (Weiss et al, 2006). The modern, hexaploid A. sativa contains three subgenomes (referred to as A,C,D) as a result of introgression from wild species, including Avena insularis, Avena maroccana and Avena murphyi, which are hypothesized to impart non-shattering and reduced awn traits in domesticated oat (Ladizinsky, 1995; Yan et al, 2016). Modern oat cultivars in the 20th and 21st centuries are inbred lines that are derived from segregating populations with selection for traits of interest (Fehr, 1987). Most traits of interest to oat breeders are highly quantitative. Grain yield is an important trait in oat and is highly responsive to selection, with average annual yield gains of 0.8% from 1923-1980 measured in Minnesota germplasm (Wych, 1983). Traits phenotypically correlated with greater yield in oat include above ground dry mass, increased time to heading, and reduced lodging (Payne et al, 1986; Wych 1983). Management of lodging in oat via agronomic practices can be accomplished through the use of plant growth regulators to increase stem strength and reduce height (Leitch and Hayes, 1990). Though management and genetics of lodging having been improved over time, lodging resistance continues to be a major focus for breeding and improvement in oat as even resistant cultivars lag behind the

lodging resistance of other cool season cereals, such as ‘Linkert’ wheat (Anderson et al, 2018).

Lodging in oat can manifest in two general categories: by buckling near the stem base of culm (root lodging) resulting in the entire stem being lodged at an angle, or through breakage in the upper internodes beneath the panicle (stem lodging). Oat cultivars are most susceptible to root lodging following heading through the soft dough stage (Z5-Z8; Zadoks et al 1974), where lodged plants cast shade on each other and minimize photosynthesis, reducing yields by up to 30% in additional to lack of mechanical harvestability (Weibel and Pendleton 1964; Zadoks et al 1974). Stem lodging typically occurs closer to maturity (Z9; Zadoks et al 1974) as the stems become brittle, resulting in yield loss due to lack of mechanical harvestability. In breeding and genetic studies of lodging resistance in oat, both root and stem lodging are both combined into a single visual lodging severity score that encompasses the severity and incidence of lodging in a plot, typically on a 0-9 or similar ordinal scale. Visual scoring of lodging has been successful in identifying genetic markers linked to quantitative trait loci (QTL) for use in marker assisted breeding to improve lodging resistance in oat. Linkage mapping studies for lodging resistance using SSR, DArT, AFLP markers in oat have identified unique QTL for lodging visual scoring (Tanhaunpaa et al, 2012; Hizbai et al, 2012) and visual scoring co-localized with height and heading date (Tanhaunpaa et al, 2012). QTL by environment interaction has also been found to be significant for lodging score QTL in oat, as lodging pressures can vary significantly across environments (De Koeyer et al, 2004). With the substantial variation in both lodging phenotypes and environmental

pressures that induce lodging, conducting genetic mapping on a finer scale using a large number of markers could identify new marker trait associations on more detailed lodging phenotypes.

Association mapping approaches in large populations genotyped at thousands of loci are well suited to identifying fine-scale trait genetic architecture in line with the phenotypes that make up lodging resistance in oat. Sequence based genotyping (SBG) of the oat genome has resulted in 10s of thousands of SNP loci for use in oat genetic studies (Huang et al, 2014). The availability of numerous SNP markers in oat have enabled marker trait associations and population genetic analyses among diverse oat landraces that were not previously possible (Chaffin et al, 2016; Winkler et al, 2016). As a breeding resource, the diverse panel of elite oat cultivars and breeding (Founder Panel) at the University of Minnesota constitutes a representative sample of North American elite oat germplasm, which is genotyped at over 13,000 SNP loci (McNish et al, 2019). Investigation of the detailed phenotypes (ie stem strength, root vs stem lodging, etc.) that underlie oat lodging resistance is well suited to this group of germplasm for identifying SNP markers linked to QTL for deployment in marker-assisted breeding programs to systematically improve aspects lodging resistance.

We present an association mapping study of detailed phenotypes underlying oat lodging resistance in North American germplasm. Our objectives are to 1) examine the phenotypic correlations among various lodging phenotypes, 2) identify marker-trait associations at SBG-derived loci in the UMN Oat Founder Population for lodging and

related agronomic traits, and 3) validate SNPs linked to QTL in derived biparental crosses and supplement with biparental linkage mapping.

Materials and Methods

Germplasm. We assessed a panel of 242 diverse oat lines (hereafter known as the 'Founder population') possessing both phenotypic data on lodging related traits and SNP genotypic data derived from sequence-based genotyping (SBS). The Founder panel, planted as an augmented design with the replicated check 'Deon', was grown in two environments in 2017 (Lamberton MN and Morris MN), and then again in three environments in 2018 (Lamberton MN, Morris MN, and Crookston MN). Founder panel plots were managed according to standard agronomic practices. Sites were fertilized at a rate of approximately 44.7kg of N/hectare (No P or K added). Each line was planted once in each environment at 2.5cm depth in 6.5m^2 plots measuring approximately 1.5m by 1.5m. Row spacing was approximately 15cm in each environment. The amount of seed sown in each plot was sufficient to produce an approximate plant density of 301 plants/m^2. Alleys were planted between plots with winter wheat or ryegrass and mowed to a height of 15cm to prevent the growth of weeds. Broadleaf control was regularly achieved using one of the following herbicides: Bronate (Bayer), Bronate Advanced (Bayer, NC), Bromac (Loveland Products, Inc), or Weld (Winfield Solutions, LLC) following the manufacturer's instructions. Additional weed control was achieved by manual cultivation in some cases. No insecticides were applied. Crown rust, caused by the fungus *Puccinia coronata* f. sp. *Avenae* P.Syd. & Syd, was controlled by the use of

one of the following fungicides at flag leaf stage (Zadok's 47): Tilt (Syngenta) or Stategо (Bayer) following the manufacturer's instructions.

Two biparental populations were derived from Founder panel lines to validate the effect of QTL identified by GWAS and to conduct additional linkage mapping for lodging and related agronomic traits. One lodging resistant parent with high strength per meter (SPM) values in 2017 (P0528A1-1) was crossed to SD090880, a low SPM line susceptible to root lodging (Cross A), and to SD111736, a low SPM line susceptible to stem lodging (Cross B). Parental selection was based on phenotypic phenotypic data from the 2017 environments (Lamberton MN and Morris MN). Crosses were made in Fall 2017 with progeny advanced in the greenhouse and growth chambers via single seed descent until the F_5 generation. Seed was bulked from multiple F_6 plants per line in the greenhouse, with field testing of validation populations commencing in summer 2019 on $F_{5:7}$ lines. Cross A contained 193 lines while Cross B contained 191 lines planted in four environments with a single replicate: Saint Paul MN early (planted 29 Apr 2019) and late (planted 14 May 2019), Crookston MN early (planted 1 May 2019) and late (planted 16 May 2019). Validation populations were planted in single row plots of 1.5m in length with 30 cm row spacing. Additional agronomic practices were the same as for the founder panel mentioned above.

Phenotyping. We phenotypted the Founder population for several lodging traits as well as agronomic traits closely related to lodging. The lodging traits included the lodging visual severity score (LVSS), strength per meter (SPM), root lodging incidence (RLI), stem lodging incidence (SLI), uprightness angle (UA), plant height (PH), and heading date

(HD). We define root lodging as a buckling of the stem at or near the culm (Figure 1A), and shoot lodging as stem buckling at least midway along the stem towards the panicle (Figure 1B). LVSS encompassed both root and stem lodging and was measured at maturity on a 0-9 visual rating scale, with 0 indicating a fully upright plot and 9 indicating the entire plot was nearly flat on the ground. SPM was measured approximately two-weeks after the average heading date for each location (early-mid July). SPM was measured using a LC703 Series miniature load cell (Omega Engineering) with a calibrated measurement range of 0-10 lbs. of force mounted to a hinged aluminum frame (push force meter), with the force recorded in pounds to bend a meter's worth of stems at half height to a 45-50° angle with respect to the ground (Figure 2A)(Spinks et al, 2003). UA was recorded at maturity by measuring the angle of a root-lodged stem with respect to the ground (with 90° indicating a fully upright stem) at three locations within a plot and then taking an average. RLI and SLI were recorded at maturity as a presence or absence (0 indicating the type of lodging was not present, 1 indicating that it was present). No plots contained both root or stem lodging in equal amounts, and if two were observed, one type of lodging was more prominent within a plot than the other. PH was measured at maturity in cm from the base of the plant to the highest point on the plant, with one measurement per plot. HD was recorded continuously as the date when 50% panicle emergence was observed on at least 50% of the plot. Linear models in the form of

$$y = g + E + gxE + e$$

Were used to estimate trait variance components. From these, broad sense heritabilities were measured for each trait as follows:

$$H^2 = \frac{V_g}{V_g + \frac{V_{gxE}}{n} + \frac{V_e}{r}}$$

With V_g the genetic variance (MS genotype – MS genotype x environment), V_{gxE} the genotype x environment interaction variance (MS genotype – (MS environment - MS 'Deon' checks) divided by the number of check replications (r) minus the number of environments (n)), and V_e the pooled error variation (MS 'Deon' checks).

Genotyping. Genotypes were obtained via short read sequencing of the 242 lines in the Founder population. Lines within the Founder population were genotyped as part of the broader Public Oat Genotyping Initiative, with a SNP calling pipeline developed in the lab of Dr. Nick Tinker and colleagues (Huang et al, 2014). Genotyping data for founder lines is available online via T3/Oat (The Triticeae Toolbox, 2019). For Founder population lines, missing genotypes were imputed using the EM method at SNPs with less than 10% missing data. Briefly, filtering of SNP markers for trait mapping comprised keeping only SNPs that were genetically mapped to one of 21 consensus linkage groups, had less than 10% missing data across lines, and had a minor allele frequency of 5% or greater. This resulted in 13,519 SNPs for further analyses. More details on the SNP marker filtering protocol for the Founder population can be seen (McNish et al, 2019).

Validation populations (Cross A and Cross B), as well as the Founder population in a separate genotyping protocol, were genotyped with the Illumina oat 6k Infinium SNP chip as F5 lines (A SNP Genotyping Array for Hexaploid Oat). Initial SNP calls were made using Genome Studio v2.0, with markers possessing a mean intensity below 0.1 (AA or BB) or clustering poorly (cluster score below 0.15) removed immediately.

Individuals possessing more than 5% missing data were also removed immediately. After calling SNPs, SNP markers were filtered separately in each biparental population. Monomorphic SNPs, markers with more than 5% missing data, markers with more than 10% heterozygous calls, and markers with greater than a 70:30 segregation ratio were removed.

Association and Linkage Mapping. Association mapping in the founder panel was conducted using the rrBLUP R package at the 13,519 SBG SNPs for each trait. Population structure was accounted for using the first three principal components fit as a fixed effect based on the clustering of the founder panel into three distinct subpopulations (McNish et al, 2019). Two significance thresholds based on log(p) values were used in detecting QTL. The log(p) significance threshold at alpha = 0.05 for declaring a significant association (at the "Bonferroni" level) was determined using a Bonferroni correction with the total number of markers (13,519) used as the number of independent tests. The log(p) significance threshold for a significant association at the "modified Bonferroni" level at alpha = 0.05 was determined via an eigenvalue decomposition of linkage group genetic correlation matrices to reduce the number of independent tests (Li and Ji, 2005). Briefly, correlation matrices of marker data for each linkage group were generated followed by eigenvalue decomposition, with the number of effective markers equivalent to the number of eigenvalues greater than one plus the fractional value of each eigenvalue summed for all linkage groups (Li and Ji, 2005; McNish et al., 2019). The total number of effective markers (2,231) resulted in substantially fewer independent tests

for the declaration of a significant marker trait association for lodging and related agronomic traits to entertain the possibility of linkage with a smaller effect QTL.

Genomic prediction cross validations were carried out using a mixed model approach implemented in the r package rrBLUP. Within the founder panel, 60% of the lines were randomly assigned as part of the training line set and the remaining 40% constituted the validation line set. First, Marker effects were predicted for using the linear mixed effect model (Bernardo, 2002):

$$y = X\beta + Zu + e$$

With *y* a vector of phenotypic observations averaged over all five environments, *X* the design matrix for the vector of estimated fixed effects β, *Z* the design matrix for the vector of predicted random effects *u*. Following the estimation of β and the prediction of *u*, predicted trait values y_{pred} were calculated based on the genotypes of the lines Z_{valid} in the validation set:

$$y_{pred} = Z_{valid}u + \beta$$

With cross prediction accuracy determined by correlating the predicted phenotypic values with the observed phenotypic values within the validation line set. This sampling procedure was carried out 500 times for each phenotypic trait to obtain a mean and 95% confidence interval around the correlation.

Separate biparental linkage maps for the two validation populations (Cross A and Cross B) were created and refined using the R packages qtl and ASMap (Broman et al 2003; Taylor and Butler, 2017). The linkage maps were not merged, as only 39% of markers were shared between the two. Filtered SNP markers in each population were

assigned to linkage groups based on markers having a recombination frequency of 0.35 or lower, and a LOD score of 8 or higher. A genotyping error rate of 0.0075 was estimated for both populations based on the maximum likelihood of the error rate across all linkage groups (Broman et al, 2003). Markers were ordered along linkage groups using a sliding window approach, with the optimal order determined for the case that minimized obligate crossovers. Linkage maps in both populations were further condensed by dropping one marker at a time recording the change in linkage group length and LOD likelihood. The marker (not at the end) with the most length change per linkage group was identified and removed from the dataset. Furthermore, markers mapped to linkage groups in each cross were compared with the position of the markers on the oat consensus map (Chaffin et al, 2016; Bekele et al, 2018). Additional markers were removed if they originated on a different linkage group within a set of otherwise consecutive markers on the consensus map, and linkage groups in each cross were split up if they contained segments from different consensus map linkage groups (Chaffin et al, 2016; Bekele et al, 2018). Linkage groups in each cross were re-named according to the originating linkage group of their markers on the oat consensus map. We report the linkage group name, mapping statistics, and R^2 value comparing the positions in the cross-linkage map with those in the oat consensus map (Appendix VII, Supplemental Tables S1-2; Appendix VII, Supplemental Figures S1-2). In all, the linkage map for cross A contained 594 SNP markers, encompassing 2590.6 cM with an average distance of 4.8 cM on 54 linkage groups. The linkage map for cross B contained 464 SNP markers, encompassing 2614.4 cM with an average distance of 6.2 cM on 45 linkage groups. QTL were mapped using a composite

interval mapping approach using the “em” method with a mapping window of 10 cM (Broman et al, 2003). LOD thresholds for declaring a major QTL were set using a Bonferroni correction on the LOD values, using the number of markers mapped for each cross as the number of independent tests. We considered QTLs to be the same if markers exceeding the Bonferroni LOD threshold were within 30 cM.

Table 1. Chapter 6 list of abbreviations

Abbreviation	Definition
H^2	Broad Sense Heritability
LVSS	Lodging Visual Severity Score
UA	Uprightness Angle (°)
RLI	Root Lodging Incidence
SLI	Stem Lodging Incidence
SPM	Strength Per Meter (lbs/m)

Results

Phenotypic Data. Means for lodging and related agronomic traits varied across environments (Table 2). Significant differences as determined by an LSD test were often present between environments, with mean LSS, UA, and PH significantly different across all environments tested (Table 2). Root lodging was not observed in Morris 2017, resulting in a mean RLI of 0 and a mean UA of 90°.

Table 2. Environmental means for lodging and related agronomic traits by environment

Environment	LVSS	SPM	RLI	SLI	UA	PH	HD
Lamberton 2017	3.0c	4.6a	0.70b	0.06c	77.5c	83.9e	165.8d
Lamberton 2018	2.5d	3.9b	0.74b	0.03c	74.2d	85.7d	177.4b
Morris 2017	4.6b	3.2c	0.00d	0.16b	90.0a	93.7b	164.8d
Morris 2018	5.2a	3.8b	0.99a	0.01c	56.3e	109.9a	184.5a
Crookston 2018	1.0e	4.8a	0.33c	0.34a	86.1b	92.4c	168.6c

Unique letters indicate significant differences between means at alpha =0.05

Broad sense heritabilities were lower for lodging traits than for the related agronomic traits (Table 3). Significant genotype and environment effects were observed for each trait, while Genotype by environment interactions were significant for all traits except SPM.

Table 3. Broad sense heritability values for lodging and related agronomic traits

Trait	Broad Sense Heritability
Lodging Visual Severity Score	0.18
Strength Per Meter	0.23
Root Lodging Incidence	0.04
Stem Lodging Incidence	0.05
Uprightness Angle	0.10
Plant Height	0.37
Heading Date	0.42

Numerous significant Pearson correlations existed between phenotypic traits (excluding RLI and SLI) (Table 4). Strength Per Meter was negatively correlated with LVSS and PH, while UA was negatively correlated with HD. Apart from the incidence traits RLI and SLI, UA and LVSS values were both less normally distributed in relation to SPM, HD, and PH (Figure 3).

Table 4. Pearson correlation coefficients for SPM, UA, LVSS, HD, and PH

	SPM	UA	LVSS	HD	PH
SPM	1				
UA	0.08**	1			
LVSS	-0.30***	-0.51***	1		
HD	-0.07*	-0.68***	0.19***	1	
PH	-0.18***	-0.34***	0.38***	0.50***	1

Significance codes * 0.01 **0.001 ***<0.001

Association Mapping. Manhattan plots of each trait are presented for the lodging traits (Figure 1). Among the lodging traits, only SLI possessed SNPs in significant association at the Bonferroni level (Figure 1F). The SLI associations on Mrg08 does not colocalize with any other lodging related traits. A marker associated at the modified Bonferroni level for UA on Mrg06, while prominent though not meeting the modified Bonferroni threshold appeared on linkage groups 1 and 2 (Figure 1G). RLI possessed a marker associated at the modified Bonferroni level on Mrg28 (Figure 1E). The lodging traits LVSS and SPM did not possess any discernible patterns of significant associations. Lodging trait associations were not detectable in separate associations for each

environment's data, with only SLI associating at the Bonferroni level on Mrg08 in three of the five environments tested, and one environment with the Mrg08 associations completely absent in Crookston 2018 (Supplemental Figure 4E). All other lodging traits showed variable detection of marker-trait associations in individual environments (Supplemental Figures S3-S7). QQ plots of lodging and related agronomic traits demonstrated that for traits with associations at the Bonferroni level, true associations departed from a normal distribution of expected log(p) values (Supplemental Figures S8-S9).

At the marker-trait associations on Mrg02, four SNPs (avgbs_95303.1.18, avgbs2_112468.1.57, avgbs2_112468.1.58,avgbs2_112468.1.59) colocalized for both HD and PH respectively (Table 5). The SNP avgbs_95303.1.18 possessed an effect size of -0.02 days for heading and -0.03cm for height, with the three other SNPs each possessing effect sizes of 0.02 days for HD and 0.03 cm for PH. Furthermore, on Mrg02, three SNPs (avgbs2_165506.1.17, avgbs2_165506.1.20, avgbs2_165506.1.51) met the Bonferroni level for association with HD, while they were nearly significant at the modified Bonferroni level for PH (alpha = 0.08) and UA. (alpha = 0.11) (Table 5). The effect sizes for all three of these snps were 0.01 days for HD, 0.02 cm for PH, and -0.004° for UA.

Table 5. SNP log(p) values at markers exceeding the Bonferroni (5.43) and modified Bonferroni (4.65) thresholds for each phenotype.

Marker	Linkage Group	Position (cM)	LVSS	SPM	RLI	SLI	UA	PH	HD
avgbs_95303.1.18	Mrg02	33.6	2.13	0.77	2.06	0.91	2.67	5.55	5.63
avgbs2_112468.1.57	Mrg02	34.1	1.27	0.11	2.77	2.04	3.37	5.47	6.33
avgbs2_112468.1.58	Mrg02	34.1	1.27	0.11	2.77	2.04	3.37	5.47	6.33
avgbs2_112468.1.59	Mrg02	34.1	1.27	0.11	2.77	2.04	3.37	5.47	6.33
avgbs2_165506.1.17	Mrg02	34.1	2.2	0.13	3.62	2.38	4.27	4.4	5.72
avgbs2_165506.1.20	Mrg02	34.1	2.2	0.13	3.62	2.38	4.27	4.4	5.72
avgbs2_165506.1.51	Mrg02	34.1	2.2	0.13	3.62	2.38	4.27	4.4	5.72
avgbs2_6837.2.14	Mrg02	34.1	1.58	0.19	2.83	2.83	3.15	3.87	6.88
avgbs2_6837.2.50	Mrg02	34.1	1.58	0.19	2.83	2.83	3.15	3.87	6.88
avgbs2_151393.1.58	Mrg06	116	3.84	2.12	1.76	1.55	4.64	0.55	0.55
avgbs_cluster_10508.1.24	Mrg08	125.3	0.1	0.36	0.57	5.05	0.24	0.07	0.52
avgbs_cluster_10508.1.32	Mrg08	125.3	0.1	0.36	0.57	5.05	0.24	0.07	0.52
avgbs_cluster_37536.1.61	Mrg08	125.3	0.04	0.47	1	5.69	0.58	0.34	1.48
avgbs2_183736.1.61	Mrg08	125.3	0.04	0.47	1	5.69	0.58	0.34	1.48
avgbs2_193093.1.28	Mrg08	129.6	0.53	1.18	0.42	4.86	0.03	0.24	0.06
avgbs2_193093.1.63	Mrg08	129.6	0.53	1.18	0.42	4.86	0.03	0.24	0.06
avgbs_cluster_19179.1.6	Mrg08	142	0.18	0.88	0.56	5.29	0.94	0.88	1.53
avgbs2_91402.1.6	Mrg08	142	0.18	0.88	0.56	5.29	0.94	0.88	1.53
avgbs_cluster_14153.1.60	Mrg08	142.3	0.09	0.95	0.56	5.92	0.74	0.9	1.43
avgbs_cluster_41221.1.36	Mrg08	142.3	0.92	0.63	1.24	5.04	1.81	0.76	1.15
avgbs_7327.1.6	Mrg08	151.9	0.2	0.44	0.58	4.73	0.2	0.2	0.04
avgbs_cluster_39973.1.43	Mrg28	32.6	2.08	3.14	4.62	0.55	3.05	0.08	0.64

Genomic Prediction. Prediction accuracies using the founder panel training line set were lower for lodging traits than the related agronomic traits of PH and HD (Table 6). RLI

and SLI possessed the lowest prediction accuracies of the lodging traits as well as the lowest H^2 values. Similarly, PH and HD both had high prediction accuracies and the highest H^2 values.

Table 6. Resampled cross validation prediction accuracies for lodging and related agronomic traits

Trait	Cross validation prediction accuracy
Lodging Visual Severity Score	0.47 ± 0.002
Strength Per Meter	0.40 ± 0.1
Root Lodging Incidence	0.16 ± 0.005
Stem Lodging Incidence	0.24 ± 0.006
Uprightness Angle	0.41 ± 0.005
Plant Height	0.66 ± 0.16
Heading Date	0.63 ± 0.004

Numbers following the ± symbol indicate the half-width of the 95% confidence interval

Analysis of variance for traits measured in biparental populations. Histograms of biparental population phenotypes and parental means are presented (Figure 4). While cross effects were significant for all phenotypic traits quantified in the biparental populations, the genotypic (lines nested within crosses), environmental, and genotypic by environmental effects varied in their degrees of significance (Appendix VII, Supplemental Table S3). Notably, all effects except for cross were insignificant ($p > 0.05$) for SPM (Appendix VII, Supplemental Table S3). The traits HD and PH had much

more significant effects than the remaining lodging related traits of UA and LVSS (Appendix VII, Supplemental Table S3).

SNP Validation in biparental populations. The 6k array SNP GMI_ES01_c15144_154, mapped on the consensus map to linkage group 2 at position 30.1 cM, was detected significant at the level of a major QTL based on the number of 6k markers for HD and PH. In the Founder population, individuals (n= 85) with the resistant allele had a mean heading date of 171.2 days, while individuals (n = 118) with the susceptible allele have a mean heading date of 172.7 days, which is significantly greater ($p < 0.001$) according to a t-test of the susceptible mean against the resistant mean. Individuals with the resistant allele had a mean height of 90 cm, while individuals with the susceptible allele had a mean height of 95.2 cm, which is significantly greater ($p < 0.001$) according to a t-test of the susceptible mean against the resistant mean. The SNP (A/G) GMI_ES01_c15144_154 segregated in both mapping populations, with means aggregated from individuals in both crosses. F5:7 lines with the allele (A) from the lodging resistant parent at GMI_ES01_c15144_154 headed significantly earlier and were significantly shorter in all four environments than those with the susceptible allele (G) (Table 7).

Table 7. HD (days) and PH (cm) means for individuals with resistant, susceptible alleles at SNP GMI_ES01_c15144_154

2019 Environment	Res. allele individuals (HD)	Sus. allele individuals (HD)	Res. allele individuals (PH)	Sus. allele individuals (PH)
St Paul Early	176.6a	181.1b	87.7a	93.7b
St Paul Late	184.9a	188.5b	88.2a	93.1b
Crookston Early	181.3a	185.5b	80.3a	86.7b
Crookston Late	184.8a	190.5b	82.3a	85.0b

Unique letters indicate significantly different means according to a t-test at alpha = 0.05

The 6k array snp GMI_ES15_c17486_204 mapped on the consensus map to linkage group 12 at position 63.5 cM was prominent in its association with LVSS (alpha = 0.17), though not significant at the level of a minor QTL in based on the number of 6k eigenvalues. In the founder population, individuals (n= 94) with the resistant allele have a mean severity score of 2.87, while individuals (n = 111) with the susceptible allele have a mean severity score of 3.59, which is significantly greater ($p < 0.001$) according to a t-test of the susceptible mean against the resistant mean. However this effect was unable to be validated in the two environments where lodging was observed in summer 2019, where differences in means between resistant and susceptible individuals were not significant (Table 8).

Table 8. LVSS means for individuals with resistant, susceptible alleles at SNP GMI_ES15_c17486_204

2019 Environment	Resistant allele individuals	Susceptible allele individuals
St Paul Early	3.7	3.9
St Paul Late	1.9	1.7
Crookston Early	NA	NA
Crookston Late	NA	NA

Unique letters indicate significantly different means according to a t-test

Biparental linkage mapping. Cross A and Cross B were phenotyped in summer 2019 in all four environments for PH and HD, while SPM was only quantified in mid-July 2019 in two environments (Crookston Early and Crookston Late) due to lodging in St Paul at the time of measurement. A storm on 15 Jul 2019 in St Paul enabled LVSS, UA, RLI, and SLI to be scored in two environments (St Paul Early and St Paul Late). SLI was additionally quantified in the Crookston Late environment.

Markers for HD were identified that exceeded the LOD threshold in all four environments in crosses A and B (Appendix VII, Supplemental Tables S4-S5). Markers with the highest LOD scores had consensus map positions on Mrg02 between 30 and 34.1 cM, which matched those GBS markers on Mrg02 between 33.6 and 34.1 cM significantly associated with HD in the founder population. PH was also mapped in crosses A and B to these same markers, though this co localized region for PH was not detected in the Crookston Late environment (Appendix VII, Supplemental Tables S6-S7).

No markers were mapped above the Bonferroni correction threshold for SPM in both the Crookston Early and Late environments.

Mapping LVSS in crosses A and B for the two St Paul environments failed to detect any QTL above the LOD threshold. Mapping UA only revealed significant markers in cross B grown in the St Paul Late environment, with several distributed across linkage groups Mrg01a, Mrg02a, and others (Appendix VII, Supplemental Table S8). Similarly, mapping SLI in crosses A and B failed to detect and QTL above the LOD correction threshold in any environment where SLI was observed.

Discussion

Lodging in cereal crops is a complex trait with many physical, environmental, and physiological components (Berry, 2019). As such lodging in cereal crops can be broken down into component traits such as the type of lodging (root vs stem), root lodging angles, and related traits of height and heading date. Doing so could ideally allow a better understanding of lodging phenotypes and their degree of genetic control. Though visual scoring (ie 0-9) of lodging has been successful in identifying genetic markers linked to QTL for use in marker assisted breeding of oat (De Koeyer et al, 2004; Hizbai et al, 2012; Tanhuanpää et al, 2012), the lack of consistent lodging pressure and the imprecision in quantifying lodging has long been noticed as not encompassing the underlying phenomena of stem failure under high winds (Grafius and Brown, 1954). Quantifying physical parameters of oat stems, such as the coefficient of lodging resistance measuring stem displacement under a known torque force, have higher

heritabilities in oat breeding populations than visual scoring despite taking longer to quantify (Norden and Frey, 1959; Frey et al, 1960). Aspects of oat stem strength are appealing for selecting lodging resistance as they can be measured in the absence of unpredictable lodging pressure, and can be measured quantitatively via load cells mounted on a bending meter (Wiersma et al, 2011). In this experiment, we observed a moderate negative correlation between SPM and LVSS, indicating that stronger stems lodged less as consistent with findings in previous studies (Hess and Shands, 1966; Wiersma et al, 1986; Wiersma et al, 2011). Stronger correlations however were observed between the traits LVSS, UA and HD, PH. Other oat studies have observed the tendency for early heading and or shorter lines to lodge less (Berry et al, 2015; Tumino et al 2017), and the relative strength of these correlations with PH and HD but not SPM could be due to measurement issues with SPM (discussed below). Nonetheless, the phenotypes of oat lodging exhibit correlations that could be used to select for lodging resistance when lodging events do not reliably occur year-to-year.

Though phenotypic traits were correlated with each other, genome-wide association analysis of the founder panel revealed both distinct and shared genetic architectures underlying each phenotype. Importantly, phenotypes measured did not universally display a defined genetic architecture via markers identified at the level of the Bonferroni and modified Bonferroni tests in the founder panel. The SBG markers mapped to the oat consensus map (Huang et al, 2014) exceeded the Bonferroni threshold for only the traits HD, PH, and SLI. PH and HD have been previously mapped to Mrg02 (Zimmer et al, 2018), as well as PH and crown rust resistance though markers for stem

snapping on Mrg08 have not (Sunstrum et al, 2019). Mrg08 contains known markers associated with crown rust resistance genes (Pc53) at 82.4 cM (Admassu-Yimmer et al, 2018), as well as two other loci associated with crown rust resistance (QPc.CORE.08.2 and QPc.CORE.08.3) at positions 131.3 cM and 151.9 cM, respectively (Klos et al, 2017). Apart from the SLI marker avgbs_7327.1.6 which maps to 151.9 cM on Mrg08, the GWAS results suggests two QTL for SLI on Mrg08 between positions 125.3 and 129 cM and between 142 and 142.3 cM. Though other loci at the level of modified Bonferroni were detected for UA and RLI of Mrg06 and Mrg28, no other loci associated with aspects of oat lodging have been detected except for marker GMI_GBS_4542 at 60 cM on Mrg28 in association with lodging visual scores (Tumino et al, 2017). Given the lower prominence of the markers in our study on Mrg06 and Mrg28, it is likely that they are of small effect on UA and RLI respectively if they exist at all.

While validation of the genetic effect and co-localized locus for HD and PH was successful in the mapping populations, lodging traits were not. QTLs in oat biparental mapping studies using similar numbers of markers (400-600) have been considered distinct at distances between 20 and 30 cM (Tinker et al, 2009; Hizbai et al 2012, Tanaupaa et al 2012). QTL are thus considered to be colocalized if two or more phenotypes map to the same 30 cM region on a linkage group in this experiment. Notably, the phenotypic means of F5:7 biparental lines with alleles from the lodging resistant and susceptible parents at GMI_ES01_c15144_154 co-localized with HD and PH were amplified relative to the founder population. This is likely due to the more limited genetic variation at other loci controlling HD and PH in the biparental

populations relative to the founder population that could enhance the effect of this single locus on these two traits. It could also be that the larger recombination blocks in the biparental populations relative to the diverse founder population put this locus in closer genetic linkage with the gene or genes directly controlling the trait. Unsurprisingly given its lack of meeting the Bonferroni correction threshold, the 6k array SNP GMI_ES15_c17486_204 on Mrg12 between F5:7 lines with alleles from the lodging resistant parent (P0528A1-1) vs susceptible (SD111736 vs SD090880) parents were not significant for mean LVSS. Other linkage mapping studies for lodging resistance using SSR, DArT, AFLP markers in oat have been more successful in identifying QTL for lodging visual scores (Tanhaunpaa et al, 2012; Hizbai et al, 2012) and visual scores co-localized with height and heading date (Tanhaunpaa et al, 2012). The lodging visual score QTL on linkage group 25 in Tanhaunpaa et al (2012) explained 12% of lodging visual score phenotypic variation, while three QTL on linkage groups 14,15, and 30 described in Hizbai et al (2012) explained 68% of lodging visual score phenotypic variation. Strong signals of the height and heading date co-localized QTL on Mrg02, coupled with significant differences in phenotypic means for individuals segregating at the GMI_ES01_c15144_154 SNP within this QTL indicate that the cross A and B biparental maps are sound, but that the phenotypic data on lodging was not sufficient enough to validate or detect QTL suggested in the GWAS of the founder panel.

While this study validated a co-localized QTL for two traits related to lodging outcomes, heading date and plant height, more validation will be necessary for lodging traits to confirm their existence prior to marker assisted selection schemes using markers

linked to QTL. The trait SLI was not detected in the biparental populations, with the environmental conditions leading to stem snapping less easily induced than those for root lodging. Validating SLI under environmental conditions where the trait is common will be important to validate the seemingly major associations on Mrg08 revealed in the GWAS of the founder panel. Furthermore, greater marker density than what was achieved via 6k array genotyping could improve the ability to detect QTL on Mrg08 in biparental populations. All lodging trait mapping (UA, LVSS, RLI, SLI) would likely be improved by a universal lodging pressure, i.e. automatic wind generation, that would enable lodging to be induced consistently across different environments. This would serve to improve lodging trait heritabilities by reducing environmental effects and thus the ability to identify the underlying genetics. Until such a selection pressure can be reliably induced, lodging resistance can be improved by selecting earlier heading and shorter lines at the colocalized QTL linked to SNP GMI_ES01_c15144_154, which tended to be more upright and have improved LVSS values.

Figures

Figure 1. Manhattan plots for lodging traits. Red lines indicate the p-value correction for the Bonferroni threshold at alpha = 0.05, while blue lines indicate the p-value correction for the modified Bonferroni threshold at alpha = 0.05.

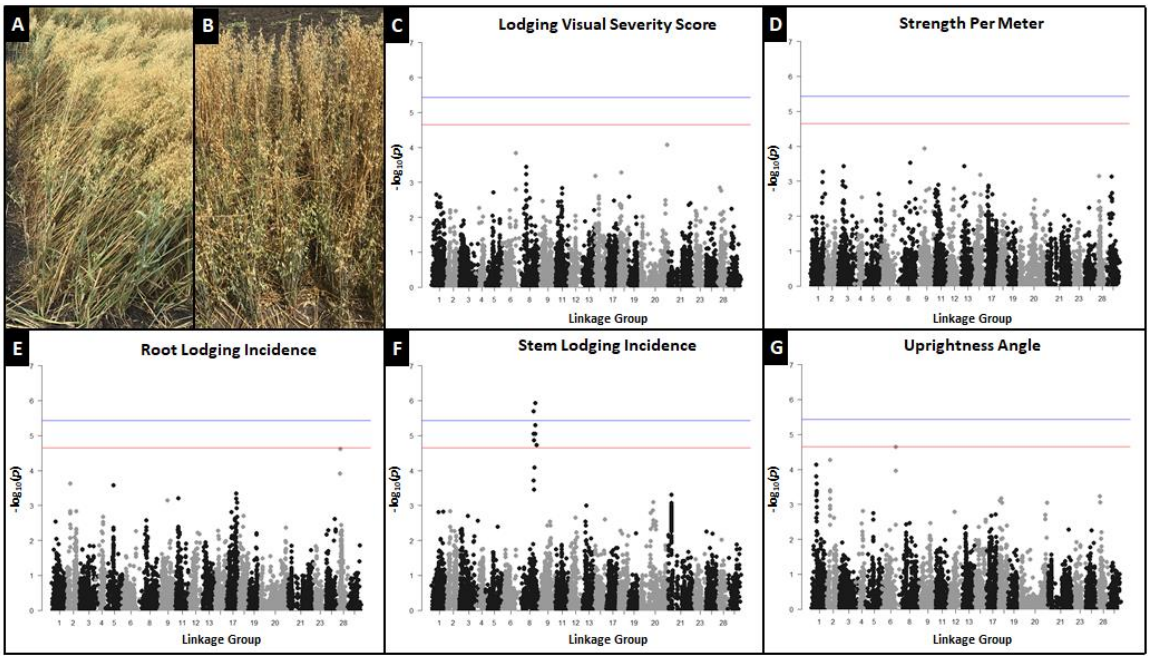

Figure 2. Manhattan plots for related agronomic traits. Red lines indicate the p-value correction for the Bonferroni threshold at alpha = 0.05, while blue lines indicate the p-value correction for the modified Bonferroni threshold at alpha = 0.05.

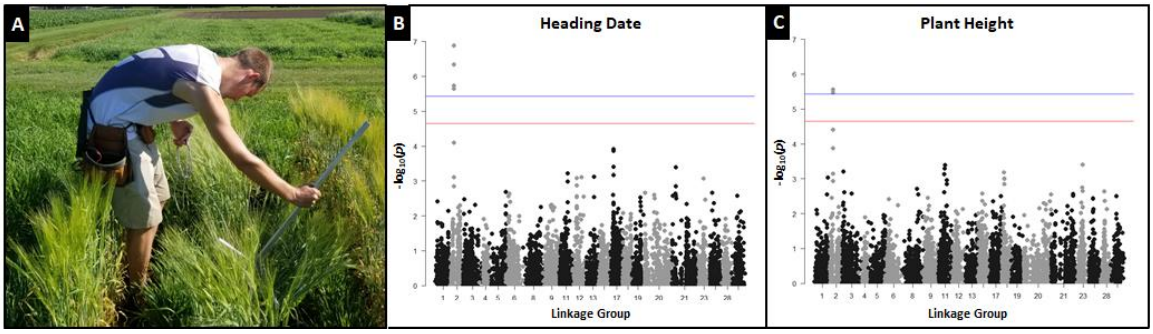

Figure 3. Correlation plot of non-incidence lodging traits and related agronomic traits

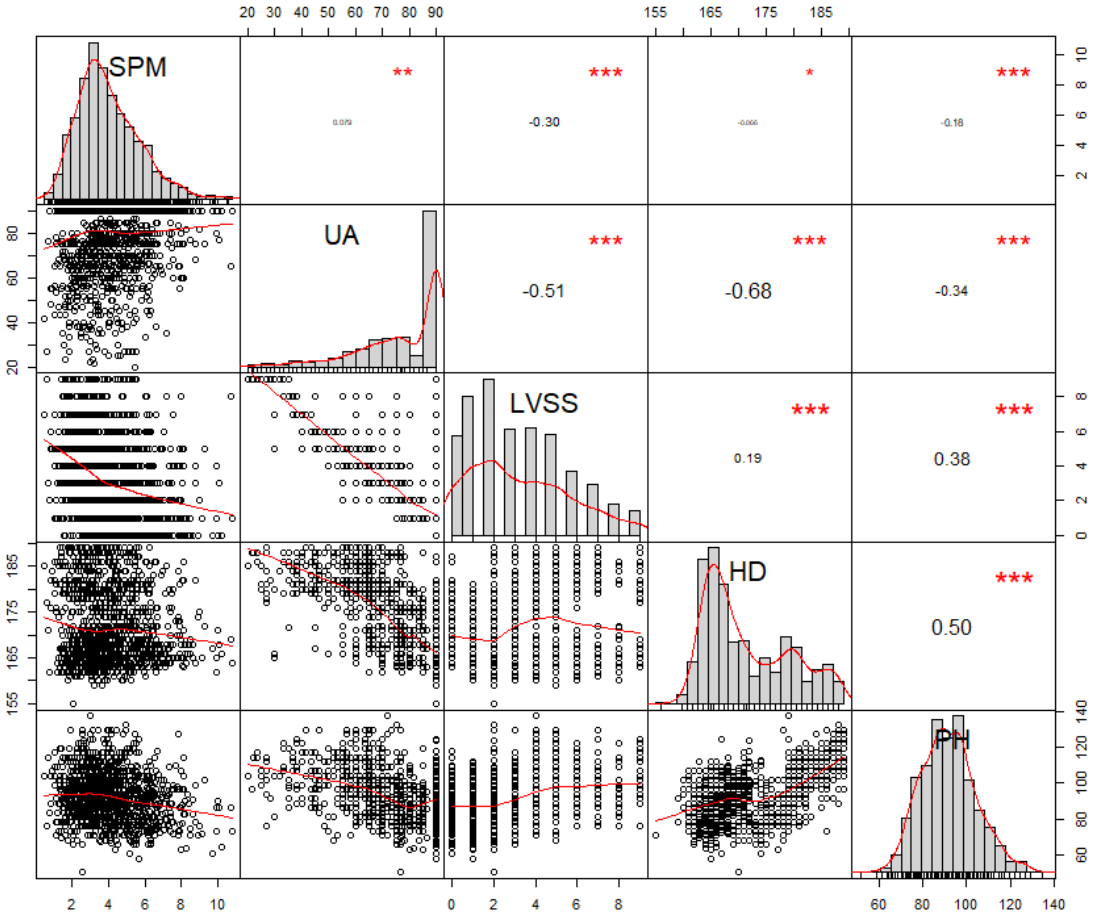

Figure 4. Histograms of phenotypic traits measured on F5:7 biparental lines in summer 2019. Cross A is represented in blue, with the mean of lodging susceptible parent SD090880 indicated by a blue triangle. Cross B is represented in red, with the mean of lodging susceptible parent SD111736 indicated by a red triangle. The mean of lodging resistant parent P0528A1-1 is indicated by a black triangle.

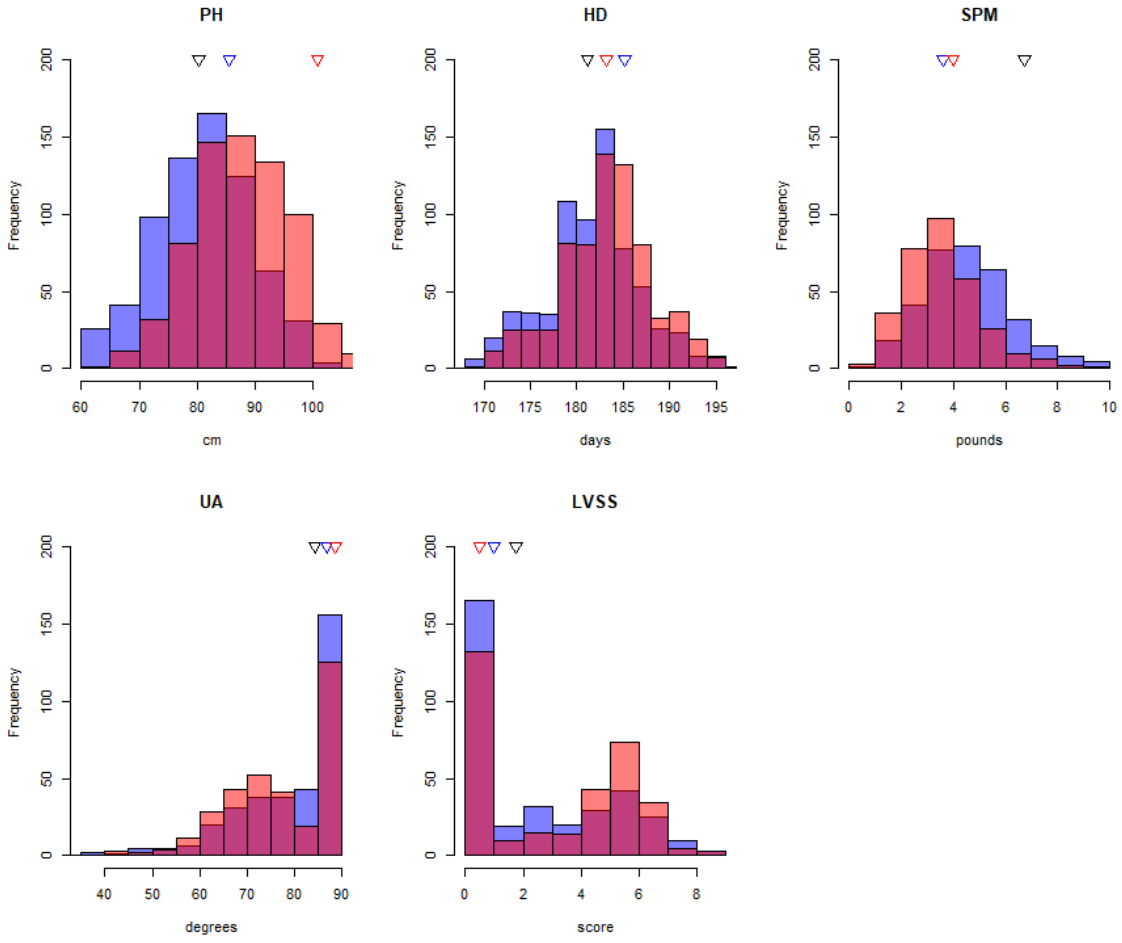

Chapter 7:

Future Directions

Alexander Q. Susko[1]

[1]University of Minnesota Dept. of Agronomy and Plant Genetics, 411 Borlaug Hall, 1991 Upper Buford Cir. St. Paul MN 55108

I view several aspects of this research as worth pursuing further or extending into other aspects of the plant sciences. Priority should be given to elucidating better genetic loci that underlie stem strength and other lodging traits in oat. Given the plentiful marker datasets and lines whose genotypes are public, I believe that a better understanding of lodging genetics is still limited by phenotyping technology. As stated in Chapter 6, a machine to induce lodging would solve the problem of environmental variability inherent to lodging events: the same storm conditions that induce lodging could finally be brought to each field experiment. We have found that the design of such a machine is more involved than initially planned, as more wind needs to be created to induce lodging in the absence of rainfall accompanying severe storms. The windspeeds required are beyond what commercially available equipment, such as leaf blowers or exhaust fans, can produce. A gas-powered hot air balloon inflator fan is one powerful piece of equipment that was not tested to induce lodging but could be a possible solution.

Though the evidence in this dissertation is inconclusive, it is my suspicion that the trait of stem strength is more heritable than these data reflect. The 'snapback' trait reported by oat breeders is itself heritable, and researchers who go to the field and beginning pulling back or pushing oats can quickly discover variation between varieties. My guess is that human errors in measurement are the culprit: any bending test in the field requires the researcher to bend over hundreds of times a day in ways that are not ergonomic, leading to the body to shift slightly and add or subtract forces from the load cell. Furthermore, it is very hard to collect stem strength data at precisely the same time relative to the planting date in each environment due to weather, logistics, etc. Even on

the same day, turgidity of plant stems likely plays a contributing role to stem strength. A method to collect this data automatically and at high throughput could enable averaging over multiple collection timepoints within one week to average over environmental variation contributing to strength differences such a turgidity and provide higher quality data not subject to the limitations of human ergonomics. I envision a bar attached perpendicular to a utility vehicle that can record the torque experienced as it drives over plots at a fixed speed. There would then be a signal of changing torques that, at a constant speed, will correspond to different plots over time. This device could be further advanced by affixing an ultrasonic height sensor (like those commonly mounted on sprayer booms) to give height data of the next plot, so that height adjustments could be made automatically to the torque bar. Such a device would be useful to cereal breeders and could be extended to other short crops, such as canola or flax.

The camera system developed and applied in this research is complex, and likely best used for basic research on plant-wind interactions as opposed to make selections in a breeding program. However, the 360° field of view camera could be mounted to single posts in the field and could take image data multiple times a day. This could be useful in quantifying rapidly changing phenotypes, such as hypersensitive wilt responses or rapidly manifesting nutrient deficiencies that have substantial environmental components. The image analysis pipeline proposed in Chapter 4 is well suited to quantifying data from individual plots given a field design and reference point, enabling automated data collection and real time data analysis.

Finally, a better understanding of cereal stem material properties is warranted. Significant steps are being made in this area by collaborators on the lodging projects at the University of Minnesota in looking at the material properties (young's modulus, other complex material models) of oat stems to understand the optimal stem structures at the microscopic level to improve lodging resistance. Additional testing, such as the amount of lignin relative to cellulose in cereal stems, might explain some of the radically different stem bending profiles observed in the wind tunnel (Chapter 4) and in field stem oscillating frequencies (Chapters 3,5) between oat and wheat. The development of a lignin-cellulose assay for cereals could be another screening method for lodging resistance if the relative amounts of these polymers is revealed to be relevant to plant stem bending and lodging outcomes.

Based upon the research in this dissertation, I recommend that oat breeders us marker assisted selection at GMI_ES01_c15144_154, selecting individuals with the A allele for both early heading and shorter height. Then evaluate among those selected lines for high yield, disease resistance, and field lodging resistance. Furthermore, be mindful of the stems during selection, and focus selection on lines with whip like stem bending pattern as displayed in the wind tunnel experiment in Chapter 4. These stems should resist greater drag forces caused by wind and recover to full height in the event of severe weather. Finally, continue to develop the markers that can be genotyped for the detection of stem snapping, and the phenotyping technologies to better quantify stem strength in the field and a machine to reliably induce lodging.

Bibliography

Admassu-Yimer, B., Bonman, J.M. and Klos, K.E., 2018. Mapping of crown rust resistance gene Pc53 in oat (Avena sativa). PloS one, 13(12):e0209105.

Anderson, J.A., Wiersma, J.J., Linkert, G.L., Reynolds, S.K., Kolmer, J.A., Jin, Y., Rouse, M., Dill-Macky, R., Hareland, G.A. and Ohm, J.B., 2018. Registration of 'Linkert'spring wheat with good straw strength and adult plant resistance to the Ug99 family of stem rust races. Journal of Plant Registrations, 12(2): 208-214.

Araus, J.L. and J.E. Cairns. 2014. Field high-throughput phenotyping: the new crop breeding frontier. Trends in Plant Science, 19(1):52-61.

Baker CJ. 1995. The development of a theoretical model for the windthrow of plants. Journal of Theoretical Biology, 175(3):355-72.

Baker, C.J., Berry, P.M., Spink, J.H., Sylvester-Bradley, R., Griffin, J.M., Scott, R.K. and Clare, R.W., 1998. A method for the assessment of the risk of wheat lodging. Journal of Theoretical Biology, 194(4):587-603.

Baker, C.J., Sterling, M. and Berry, P., 2014. A generalised model of crop lodging. Journal of Theoretical Biology, 363:1-12.

Bekele, W.A., Wight, C.P., Chao, S., Howarth, C.J. and Tinker, N.A., 2018. Haplotype-based genotyping-by-sequencing in oat genome research. Plant biotechnology journal, 16(8):1452-1463.

Bendig J, Bolten A, Bareth G. 2013. UAV-based imaging for multi-temporal, very high Resolution Crop Surface Models to monitor Crop Growth Variability. Photogrammetrie-Fernerkundung-Geoinformation, (6):551-62.

Bernardo, R., 2002. Breeding for quantitative traits in plants (Vol. 1, p. 369). Woodbury: Stemma Press.

Berry P.M. 2019. Lodging Resistance in Cereals. In: Savin R., Slafer G. (eds) Crop Science. Encyclopedia of Sustainability Science and Technology Series. Springer, New York, NY

Berry, P.M., Griffin, J.M., Sylvester-Bradley, R., Scott, R.K., Spink, J.H., Baker, C.J. and Clare, R.W., 2000. Controlling plant form through husbandry to minimise lodging in wheat. Field Crops Research, 67(1):59-81.

Berry, P.M., Kendall, S., Rutterford, Z., Orford, S. and Griffiths, S., 2015. Historical analysis of the effects of breeding on the height of winter wheat (Triticum aestivum) and consequences for lodging. Euphytica, 203(2):375-383.

Berry PM, Sterling M, Baker CJ, Spink J, Sparkes DL. 2003. A calibrated model of wheat lodging compared with field measurements. Agricultural and Forest Meteorology, 119(3-4):167-80.

Berry, P.M., Sterling, M., Spink, J.H., Baker, C.J., Sylvester-Bradley, R., Mooney, S.J., Tams, A.R. and Ennos, A.R., 2004. Understanding and reducing lodging in cereals. Advances in Agronomy, 84(04):215-269.

Berry, P.M., Sterling, M. and Mooney, S.J., 2006. Development of a model of lodging for barley. Journal of Agronomy and Crop Science, 192(2):151-158.

Berry PM, Sylvester-Bradley R, and Berry S. 2007. Ideotype design for lodging-resistant wheat. Euphytica, 154:165-179.

Braaten, J.T., Wood, P.J., Scott, F.W., Wolynetz, M.S., Lowe, M.K., Bradley-White, P. and Collins, M.W., 1994. Oat beta-glucan reduces blood cholesterol concentration in hypercholesterolemic subjects. European journal of clinical nutrition, 48(7):465-474.

Broman, K.W., Wu, H., Sen, Ś. and Churchill, G.A., 2003. R/qtl: QTL mapping in experimental crosses. Bioinformatics, 19(7):889-890.

Chaffin, A.S., Huang, Y.F., Smith, S., Bekele, W.A., Babiker, E., Gnanesh, B.N., Foresman, B.J., Blanchard, S.G., Jay, J.J., Reid, R.W. and Wight, C.P., 2016. A consensus map in cultivated hexaploid oat reveals conserved grass synteny with substantial subgenome rearrangement. The plant genome, 9(2).

Chapman, S.C., T. Merz, A. Chan, P. Jackway, S. Hrabar, M.F. Dreccer, E. Holland, B. Zheng, T.J. Ling, J. 2014. Jimenez-Berni, Pheno-copter: a low-altitude, autonomous remote-sensing robotic helicopter for high-throughput field-based phenotyping. Agronomy, 4(2): 279-301.

Chu T, Starek MJ, Brewer MJ, Masiane T, Murray SC. 2017. UAS imaging for automated crop lodging detection: a case study over an experimental maize field. In Autonomous Air and Ground Sensing Systems for Agricultural Optimization

and Phenotyping II. International Society for Optics and Photonics, 10218:102180E

Coffman, F.A., 1961. Oats and oat improvement. Oats and oat improvement. Agronomy 8:15-40.

Crook MJ, Ennos AR. 1995. The effect of nitrogen and growth regulators on stem and root characteristics associated with lodging in two cultivars of winter wheat. J of Exp Bot 46:931-938.

De Koeyer, D.L., Tinker, N.A., Wight, C.P., Deyl, J., Burrows, V.D., O'Donoughue, L.S., Lybaert, A., Molnar, S.J., Armstrong, K.C., Fedak, G. and Wesenberg, D.M., 2004. A molecular linkage map with associated QTLs from a hulless× covered spring oat population. Theoretical and applied genetics, 108(7):1285-1298.

De Langre E. 2008. Effects of wind on plants. Annual Reviews Fluid Mechanics 21(40):141-68.

De Mendiburu, F. 2017. Agricolae: statistical procedures for agricultural research. R package. version 1, 1-6.

Doaré O, Moulia B, De Langre E. 2004. Effect of plant interaction on wind-induced crop motion. Journal of biomechanical engineering. 126(2):146-51.

Fehr, W.R. 1987. Principles of cultivar development. Volume 2. Crop Species. Macmillan publishing company.

Finnigan JJ. 1978. Turbulence in Waving Wheat. Boundary Layer Met, 16:181-211.

Finnigan JJ, Mulhearn PJ. 1978. Modelling waving crops in a wind tunnel. Boundary-Layer Meteorology, 14(2):253-77.

Flesch TK, Grant RH. 1991. The translation of turbulent wind energy to individual corn plant motion during senescense. Boundary-Layer Meteorology. 55(1-2):161-76.

Flesch TK, Grant RH. 1992. Corn Motion in the Wind during Senescence: 11-Effect of Dynamic Plant Characteristics. Agronomy Journal, 84(4):748-51.

Frey, K.J., Murphy, H.C., Petr, F. and Norden, A.J., 1960. Lodging Resistance Studies in Oats. III. Optimum Number of Plots and Samples for cLr and Snap Scores 1. Agronomy Journal, 52(5):289-291.

Frey KJ, Norden AJ. 1959. Lodging Resistance Studies in Oats. II. Inheritance and Heritability 1. Agro J, 51:535-537.

Gardiner B, Berry P, Moulia B. 2016. Wind impacts on plant growth, mechanics and damage. Plant Science. 245:94-118.

Gangwar T, Schillinger D. 2019. Microimaging-informed continuum micromechanics accurately predicts macroscopic stiffness and strength properties of hierarchical plant culm materials. Mechanics of Materials, 130:39-57.

Gillies JA, Nickling WG, King, J. 2002. Drag coefficient and plant form response to wind speed in three plant species: Burning Bush (Euonymus alatus), Colorado Blue Spruce (Picea pungens glauca.), and Fountain Grass (Pennisetum setaceum). J of Geophys Res: Atmospheres, 107:1-10.

Glade, M.J., 1983. Nutrition and performance of racing Thoroughbreds. Equine Veterinary Journal, 15(1):31-36.

Gómez-Candón D, De Castro AI, López-Granados F. 2014. Assessing the accuracy of mosaics from unmanned aerial vehicle (UAV) imagery for precision agriculture purposes in wheat. Precision Agriculture, 15(1):44-56.

Grafius, J.E. and Brown, H.M. 1954. Lodging Resistance in Oats 1. Agronomy Journal, 46(9):414-418.

Hancock NI, Smith EL. Lodging in small grains. The University of Tennessee Extension. 1963. Bulletin 361.

Hess, D.C. and Shands, H.L. 1966. Lodging Response of Certain Selections of Oats, Avena sativa L., and Their Hybrid Progenies 1. Crop Science, 6(6):574-577.

Hizbai, B.T., Gardner, K.M., Wight, C.P., Dhanda, R.K., Molnar, S.J., Johnson, D., Frégeau-Reid, J., Yan, W., Rossnagel, B.G., Holland, J.B. and Tinker, N.A., 2012. Quantitative trait loci affecting oil content, oil composition, and other agronomically important traits in oat. The Plant Genome, 5(3):164-175.

Honkavaara E, Saari H, Kaivosoja J, Pölönen I, Hakala T, Litkey P, Mäkynen J, Pesonen L. 2013. Processing and assessment of spectrometric, stereoscopic imagery collected using a lightweight UAV spectral camera for precision agriculture. Remote Sensing, 5(10):5006-39.

Howard KB, Chamorro LP, Guala M. 2016. A comparative analysis on the response of a wind-turbine model to atmospheric and terrain effects. Boundary-layer meteorology, 158(2):229-255.

Huang, Y.F., Poland, J.A., Wight, C.P., Jackson, E.W. and Tinker, N.A., 2014. Using genotyping-by-sequencing (GBS) for genomic discovery in cultivated oat. PloS one, 9(7):102448.

Huete AR., 1988. A soil-adjusted vegetation index (SAVI). Remote sensing of environment, 25(3):295-309.

Inoue, E. 1955. Studies of the phenomena of Waving plants ("HONAMI") caused by wind. Journal of Agricultural Meteorology, 11(3):87-90.

Irfan, M., Muhammad, T., Amin, M. and A. Jabbar. 2005. Performance of yield and other agronomic characters of four wheat (Triticum aestivum L.) genotypes under natural heat stress. Int. J. Bot 1(2):124-127.

Jaffe MJ. 1973. Thigmomorphogenesis: the response of plant growth and development to mechanical stimulation. Planta. 114(2):143-57.

Jedel, P.E. and J.H. Helm. 1991. Lodging effects on a semidwarf and two standard barley cultivars. Agronomy Journal, 83(1):158-161.

Kelbert, A.J., Spaner, D., Briggs, K.G. and J.R. King. 2004. Screening for lodging resistance in spring wheat breeding programmes. Plant Breeding, 123(4):349-354.

Klos, K.E., Yimer, B.A., Babiker, E.M., Beattie, A.D., Bonman, J.M., Carson, M.L., Chong, J., Harrison, S.A., Ibrahim, A.M., Kolb, F.L. and McCartney, C.A., 2017. Genome-Wide Association Mapping of Crown Rust Resistance in Oat Elite Germplasm. The Plant Genome, 10(2):1-13.

Kono M, Takahashi J. 1964. Study on the mechanical properties of paddy culm with reference to lodging. Soil Sci and Plant Nutrition, 10:239-249.

Kunkel, K. E. et al., 2013: Monitoring and understanding trends in extreme storms: State of knowledge. Bulletin of the American Meteorological Society, 94(4):499-514

Ladizinsky, G., 1995. Domestication via hybridization of the wild tetraploid oats Avena magna and A. murphyi. TAG Theoretical and Applied Genetics, 91(4):639-646.

Leitch, M.H. and Hayes, J.D., 1990. Effects of single and repeated applications of chlormequat on early crop development, lodging resistance and yield of winter oats. The Journal of Agricultural Science, 115(1):11-14.

Li, J. and Ji, L., 2005. Adjusting multiple testing in multilocus analyses using the eigenvalues of a correlation matrix. Heredity, 95(3):221-227

Liu T, Li R, Zhong X, Jiang M, Jin X, Zhou P, Liu S, Sun C, Guo W. 2018. Estimates of rice lodging using indices derived from UAV visible and thermal infrared images. Agricultural and Forest Meteorology. 252:144-54.

Ma QH. 2009. The expression of caffeic acid 3-O-methyltransferase in two wheat genotypes differing in lodging resistance. J of Exp Bot, 60:2763-2771.

Madec S, Baret F, De Solan B, Thomas S, Dutartre D, Jezequel S, Hemmerlé M, Colombeau G, Comar A. 2017. High-throughput phenotyping of plant height: comparing unmanned aerial vehicles and ground LiDAR estimates. Frontiers in plant science, 8

McFerso, J.K. and Frey, K.J., 1991. Recurrent selection for protein yield of oat. Crop science, 31(1):1-8.

McNish, I.G., Zimmer, C.M., Susko, A.Q., Heuschele, J.D., Tiede, T., Case. A.J., and Smith, K.P. 2019. Multi-temporal genome-wide association mapping of crown rust resistance in elite oat germplasm. The Plant Genome, submitted

Minnesota Report 247. 2000. Agronomy and Plant Genetics at the University of Minnesota. Minnesota Agricultural Experiment Station, 111-122.

Moore-Colyer, R.J., 1995. Oats and oat production in history and pre-history. In The oat crop (pp. 1-33). Springer Netherlands.

Moore JR, Maguire DA. 2004. Natural sway frequencies and damping ratios of trees: concepts, review and synthesis of previous studies. Trees, 18(2):195-203.

Murphy HC, Petr F, Frey KJ. 1958. Lodging Resistance Studies in Oats. I. Comparing Methods of Testing and Sources for Straw Strength 1. Agronomy Journal, 50(10):609-11.

National Oceanic and Atmospheric Administration (NOAA). 2017. National Centers for Environmental Information: Billion-Dollar Weather and Climate Distasters. https://www.ncdc.noaa.gov/billions/events/MN/1980-2017

Neenan, M. and Spencer-Smith, J.L., 1975. An analysis of the problem of lodging with particular reference to wheat and barley. The Journal of agricultural science, 85(3):495-507.

Norden AJ, Frey KJ. 1959. Factors Associated with Lodging Resistance in Oats 1. Agro J, 51:335-338.

Oliver, R.E., Jellen, E.N., Ladizinsky, G., Korol, A.B., Kilian, A., Beard, J.L., Dumlupinar, Z., Wisniewski-Morehead, N.H., Svedin, E., Coon, M. and Redman, R.R., 2011. New Diversity Arrays Technology (DArT) markers for tetraploid oat (Avena magna Murphy et Terrell) provide the first complete oat linkage map and markers linked to domestication genes from hexaploid A. sativa L. Theoretical and applied genetics, 123(7):1159.

Payne, T.S., Stuthman, D.D., McGraw, R.L. and Bregitzer, P.P., 1986. Physiological changes associated with three cycles of recurrent selection for grain yield improvement in oats. Crop science, 26(4):734-736.

Pendleton JW. 1954. The Effect of Lodging on Spring Oat Yields and Test Weight 1. Agronomy Journal. 46(6):265-267.

Peng D, Chen X, Yin Y, Lu K, Yang W, Tang Y, Wang, Z. 2014. Lodging resistance of winter wheat (Triticum aestivum L.): Lignin accumulation and its related

enzymes activities due to the application of paclobutrazol or gibberellin acid. Field Crops Res, 157:1-7.

Peterson, D.M., 1998. Malting oats: Effects on chemical composition of hull-less and hulled genotypes. Cereal Chemistry, 75(2):230-234.

Potter, R.C., Castro, J.M. and Moffatt, L.C., Nurture, Inc., 1997. Oat oil compositions with useful cosmetic and dermatological properties. U.S. Patent 5,620,692.

Py C, De Langre E, Moulia B, Hémon P. 2005. Measurement of wind-induced motion of crop canopies from digital video images. Agricultural and forest meteorology, 130(3-4):223-36.

Shi Y, Thomasson JA, Murray SC, Pugh NA, Rooney WL, Shafian S, Rajan N, Rouze G, Morgan CL, Neely HL, Rana A. 2016. Unmanned aerial vehicles for high-throughput phenotyping and agronomic research. PloS one, 11(7):e0159781.

Simko,I., and H.P. Piepho. 2011. Combining phenotypic data from ordinal rating scales in multiple plant experiments. Trends in plant science, 16(5):235-237.

Singh, A., Ganapathysubramanian, B., Singh, A.K. and Sarkar, S., 2016. Machine learning for high-throughput stress phenotyping in plants. Trends in plant science, 21(2):110-124.

Spinks, J., Berry, P.M., Fenwick, R. and Gay, A., 2003. To establish separate power ratings for stem and root lodging in the UK Recommended Lists for wheat: HGCA Project No. 2213 Final Report.

Stuthman, D.D. and Marten, G.C., 1972. Genetic variation in yield and quality of oat forage. Crop science, 12(6):831-833.

Sugden, M.J., 1962. Tree sway period—a possible new parameter for crown classification and stand competition. The Forestry Chronicle, 38(3):336-344.

Sun R, Sun XF, Wang SQ, Zhu W, Wang XY (2002) Ester and ether linkages between hydroxycinnamic acids and lignins from wheat, rice, rye, and barley straws, maize stems, and fast-growing poplar wood. Industrial Crops and Products 15:179-188.

Sunstrum, F.G., Bekele, W.A., Wight, C.P., Yan, W., Chen, Y. and Tinker, N.A., 2019. A genetic linkage map in southern-by-spring oat identifies multiple quantitative trait loci for adaptation and rust resistance. Plant breeding, 138(1):82-94.

Susko AQ. 2018a. Online repositories for Chapter 2. Available at https://github.com/Hortus/CameraTrack

Susko AQ. 2018b. Online repositories for Chapter 3. Available at https://github.com/Hortus/PlantMovementReadme

Susko AQ. 2019a. Online repositories for Chapter 4. Available at https://github.com/Hortus/windtunnel_video_analysis

Susko AQ, Gilbertson F, Heuschele DJ, Smith K, Marchetto P. 2018. An automatable, field camera track system for phenotyping crop lodging and crop movement. HardwareX. 2018 4.

Susko, A.Q., Marchetto, P., Heuschele, D.J. and K.P. Smith. 2019. Quantifying cereal crop movement through hemispherical video analysis of agricultural plots. Plant Methods, 15(1):55.

Tanhuanpää, P., Manninen, O., Beattie, A., Eckstein, P., Scoles, G., Rossnagel, B. and Kiviharju, E., 2012. An updated doubled haploid oat linkage map and QTL mapping of agronomic and grain quality traits from Canadian field trials. Genome, 55(4):289-301.

Taylor, J. and Butler, D., 2017. R package ASMap: efficient genetic linkage map construction and diagnosis. arXiv preprint arXiv:1705.06916.

The Triticaceae Toolbox. 2019. Available at https://triticeaetoolbox.org/oat/

Thiago LRLDS, Kellaway RC (1982) Botanical composition and extent of lignification affecting digestibility of wheat and oat straw and paspalum hay. Animal Feed Sci and Tech, 7:71-81.

Thirsk, J. ed., 1967. The agrarian history of England and Wales (Vol. 2). CUP Archive.

Tinker, N.A., Kilian, A., Wight, C.P., Heller-Uszynska, K., Wenzl, P., Rines, H.W., Bjørnstad, Å., Howarth, C.J., Jannink, J.L., Anderson, J.M. and Rossnagel, B.G., 2009. New DArT markers for oat provide enhanced map coverage and global germplasm characterization. BMC genomics, 10(1):39.

Tumino, G., Voorrips, R.E., Morcia, C., Ghizzoni, R., Germeier, C.U., Paulo, M.J., Terzi, V. and Smulders, M.J., 2017. Genome-wide association analysis for lodging tolerance and plant height in a diverse European hexaploid oat collection. Euphytica, 213(8):163.

University of Minnesota DNR Mesonet Weather Station. https://mesowest.utah.edu/cgi-bin/droman/meso_base_dyn.cgi?stn=UMGM5&unit=0&timetype=LOCAL. Accessed 12 Dec. 2017.

Verma V, Worland AJ, Savers EJ, Fish L, Caligari PDS, Snape JW (2005) Identification and characterization of quantitative trait loci related to lodging resistance and associated traits in bread wheat. Plant Breeding, 124:234-241.

Wang J, Jinmai Z, Quinquin L, Nianjun T, Zhensheng L, Bin L, Aimin Z, Jinxing L 2006. Effects of stem structure and cell wall components on bending strength in wheat. Chinese Sci Bulletin, 51:815-823.

Weibel, R.O. and Pendleton, J.W., 1964. Effect of Artificial Lodging on Winter Wheat Grain Yield and Quality 1. Agronomy Journal, 56(5):487-488.

Weiss, E., Kislev, M.E. and Hartmann, A., 2006. Autonomous cultivation before domestication. Science, 312:1608.

Wiersma JJ, Dai J, Durgan BR. 2011. Optimum timing and rate of trinexapac-ethyl to reduce lodging in spring wheat. Agro. J, 103:864-870.

Wiersma DW, Oplinger ES, Guy SO (1986) Environment and Cultivar Effects on Winter Wheat Response to Ethephon Plant Growth Regulator 1. Agro J, 78:761-764.

Winkler, L.R., Michael Bonman, J., Chao, S., Admassu Yimer, B., Bockelman, H. and Esvelt Klos, K., 2016. Population structure and genotype–phenotype associations in a collection of oat landraces and historic cultivars. Frontiers in plant science, 7:1077.

Wych, R.D. and Stuthman, D.D., 1983. Genetic improvement in Minnesota-adapted oat cultivars released since 1923. Crop Science, 23(5):879-881.

Yan, H., Bekele, W.A., Wight, C.P., Peng, Y., Langdon, T., Latta, R.G., Fu, Y.B., Diederichsen, A., Howarth, C.J., Jellen, E.N. and Boyle, B., 2016. High-density marker profiling confirms ancestral genomes of Avena species and identifies D-genome chromosomes of hexaploid oat. Theoretical and Applied Genetics, 129(11):2133-2149.

Yang MD, Huang KS, Kuo YH, Tsai HP, Lin LM. 2017. Spatial and spectral hybrid image classification for rice lodging assessment through UAV imagery. Remote Sensing, 9(6):583.

Zadoks, J.C., Chang, T.T. and Konzak, C.F., 1974. A decimal code for the growth stages of cereals. Weed research, 14(6):415-421.

Żebrowski, J., 1999. Dynamic behaviour of inflorescence-bearing Triticale and Triticum stems. Planta, 207(3):410-417.

Zimmer, C.M., Ubert, I.P., Pacheco, M.T. and Federizzi, L.C., 2018. Molecular and comparative mapping for heading date and plant height in oat. Euphytica, 214(6):101.

Zohary, D., Hopf, M. and Weiss, E., 2012. Domestication of Plants in the Old World: The origin and spread of domesticated plants in Southwest Asia, Europe, and the Mediterranean Basin. Oxford University Press on Demand.

Appendices

Appendix I: Chapter 2 Design Files Table

Design file name	File type	Open source license	Location of the file
End Post Mounting System	STL	CC BY-SA	*https://github.com/Hortus/CameraTrack*
Motor Box	STL	CC BY-SA	*https://github.com/Hortus/CameraTrack*
Motor shaft_wood spacer	STL	CC BY-SA	*https://github.com/Hortus/CameraTrack*g
Timing Belt Pulley	STL	CC BY-SA	*https://github.com/Hortus/CameraTrack*
Motor Post End Assembly	STL	CC BY-SA	*https://github.com/Hortus/CameraTrack*
Wood Corner Bracket	STL	CC BY-SA	*https://github.com/Hortus/CameraTrack*
End Post	STL	CC BY-SA	*https://github.com/Hortus/CameraTrack*
Motor Bearing	STL	CC BY-SA	*https://github.com/Hortus/CameraTrack*
Main assembly	STL	CC BY-SA	*https://github.com/Hortus/CameraTrack*
QR Code	STL	CC BY-SA	*https://github.com/Hortus/CameraTrack*
Trolley Bracket	STL	CC BY-SA	*https://github.com/Hortus/CameraTrack*
Steel Post	STL	CC BY-SA	*https://github.com/Hortus/CameraTrack*

Timing Belt	STL	CC BY-SA	*https://github.com/Hortus/CameraTrack*
Non-motor pulley end post	STL	CC BY-SA	*https://github.com/Hortus/CameraTrack*
L-Bracket	STL	CC BY-SA	*https://github.com/Hortus/CameraTrack*
End Pulley	STL	CC BY-SA	*https://github.com/Hortus/CameraTrack*
Stillframe1	tif	CC BY-SA	*https://github.com/Hortus/CameraTrack*
Stillframe2	tif	CC BY-SA	*https://github.com/Hortus/CameraTrack*
motorRun	sh	CC BY-SA	*https://github.com/Hortus/CameraTrack*
motorForward	sh	CC BY-SA	*https://github.com/Hortus/CameraTrack*
motorReverse	sh	CC BY-SA	*https://github.com/Hortus/CameraTrack*
STOP	sh	CC BY-SA	*https://github.com/Hortus/CameraTrack*

Appendix II. Chapter 2 Bill of Materials Table

Designator	Component	Number	Cost per unit	Total cost	Source of materials	Material type
Control Box						
Control box	Nice Box NE-OOO-2919 290X190X140mm	1	$15	$15	Hi Box	Polymer
Pocket Chip	Pocket C.H.I.P	1	$69	$69	Next Thing Co.	Other
Rasbperry Pi	Raspberry Pi 3 Model B V1.2	1	$35.20	$35.20	Raspberry Pi Foundation	Other

Relay switch	SRD-05VDC-SL-C	5	$5.25	$26.25	Songle	Other
WiFi router	N300 WiFi range extender	1	$29.99	$29.99	Netgear	Other
Voltage Regulator	LM2596S DC-DC voltage reduction module	1	$2.64	$2.64	Alloet	Other
Solar Panel	HQST - 100W solar panel	2	$156.47	$312.94	HQST Solar Power	Other
Limit Switch	a11021800ux0120 Micro Limit Switch Long Straight Hinge Lever Arm SPDT Snap Action LOT	2	$5.40	$10.80	Uxcell	Other
Battery	Bluetop Marine Dual Purpose Battery	1	$330.99	$330.99	Optima	Other
Battery Box	Moeller battery box 24 series	1	$14.99	$14.99	Moeller	Other
Motor Mount						
End Pulley	Rotary 12427 Idler Pulley	1	$12.99	$12.99	Mower Partsman	Metal
Timing Belt Pulley	Aluminum Alloy XL Type 40 Teeth 8mm Pilot Bore Screwed Timing Belt Pulley	1	$9.86	$9.86	Uxcell	Metal
Motor	12 VDC Gear Motor	1	$20.00	$20.00	Ax-Man Surplus Stores (Equivalent motor)	Other
Motor Shaft	Eowpower 5Pcs Linear Motion Shaft 8mm X 100mm Round Hardened Lathe Bar Rod	1	$1.90	$9.49	Eowpower	Metal
Shaft Coupler	Motor Shaft 8mm to 8mm Joint Helical Beam Coupler Coupling D18L25	1	$7.98	$7.98	Uxcell	Metal
Motor Housing	Waterproof Rectangle Project Enclosure Case Junction Box (200x120x75 mm)	1	$13.99	$13.99	Ocharzy	Polymer

Shaft Bearing	KFL08 8mm Zinc Alloy Self Aligning Pillow Block Flange Bearing	2	$2.92	$5.85	Uxcell	Metal
Wood Corner Bracket	3” Reinforcing L-Angle	2	$8.00	$16.00	Siwek Lumber (Equivalent bracket)	Metal
Trolley Modification / Roller Base						
360FLY Camera	360fly 4K Hemispherical Video Camera	1	$474.96	$474.96	360fly Inc.	Other
Polyethylene	1/4" x 24" x 48" HDPE Sheet	1 sq ft	$31.39	$31.39	United States Plastic Corp.	Polymer
Timing Belt Clamp	XL Belt Mount A	2	$7.98	$7.98	Actobotics	Metal
Camera Nut	¼-20 coarse zinc-plated lock nut	1	$0.37	$0.37	Everbilt	Other
Camera Spacer	1/4 in. Inner Diameter - 9/16 in. Outer Diameter Rubber Grommet	2	$0.33	$0.66	The Hillman Group	Polymer
Camera Bolt	1/4 -20 x 1.5” zinc plated hex bolt	1	$0.61	$0.61	Everbilt	Metal
Camera Washer	¼ x ¾ galvanized steel flat washer	1	$0.12	$0.12	Everbilt	Metal
Roller axle	5/32 steel rod	2 ft	$2.21	$2.21	MSC Industrial Direct Co, Inc.	Metal
Roller Dowel	⅜ inch wooden dowel	4 ft	$3.99	$3.99	Home Depot	Organic
QR Codes						
Black Paint	Black Flat Exterior Paint	1 gallon	$25.98/gal	$25.98	Behr	polymer
White Paint	White Flat Exterior Paint	1 gallon	$25.98/gal	$25.98	Behr	polymer
Red Paint	Red Flat Exterior Paint	1 gallon	$25.98/gal	$25.98	Behr	polymer
Plywood	Pressure treated plywood, 0.5”	54 sq feet	$0.82/sq foot	$44.28	Georgia Pacific	Organic
Tee joint	PVC Hub x Hub x Hub Tee joint, 1.5”	36	$1.30	$46.80	NIBCO	Polymer

Elbow Joint	PVC 90 degree spigot x hub elbow, 1.5”	36	$1.86	$66.96	NIBCO	Polymer
PVC Pipe	PVC Pipe, 1.5”	162 ft	$0.54/ft	$86.83	NIBCO	Polymer
Quarter Hex Bolt	USS Hex bolt, stainless, 0.25”	200	$0.09	$19.36	Everbilt	Metal
Quarter Wingnut	Wing nut, zinc, 0.25”	200	$0.23	$46.8	Everbilt	Metal
Quarter Washer	SAE Washer, zinc, 0.25”	200	$0.04	$9.10	Everbilt	Metal
Pipe Clip	Galvanized pipe clip, 1.5”	72	$0.87	$62.64	Cramik Enterprises	Metal
Barium Sulfate	Barium sulfate, technical grade powder	2.5 kg	$18.93/kg	$47.33	Aqua Solutions	Inorganic
Track Construction						
End Post	4x4 pressure treated lumber	20 ft	$1.5/ft	$30	Siwek Lumber & Millwork, Inc (Equivalent lumber)	Organic
Box Lumber	2x4 pressure treated lumber	8 ft	$0.62/ft	$4.99	Siwek Lumber & Millwork, Inc (Equivalent lumber)	Organic
Trolley	4-bearing trolley, galvanized steel	1	$25.00	$25.00	AmCraft Manufacturing, Inc	Metal
2.5”-C Clamp	2.5” C Clamp	8	$5.79	$46.32	Bessey	Metal
Support Pulley	2x5/8” Pulley	8	$7.99	$63.92	Chicago Die Casting Manufacturing Co	Metal
Dowel	⅝” Wooden dowel	4 ft	$0.67/ft	$2.69	Home Depot	Organic
Bearing	⅝ bearing	8	$5.00	$32.00	MSC	Metal
Variable Costs (Depending on desired system length)						
Designator	Component	Total Number	Cost per 5’ (1.52 m) *	Total cost **	Source of materials	Material type
Cable	14 Ga, 3 Conductor 15 Amp 600 V 90	140 ft	$14.85	$74.26	Southwire Co.	Other

	Deg C 250 ' White Electrical wire					
Timing Belt	XL Timing Belt	300 ft	$30	$299.99	Actobotics	Polymer
Form Tube	8” Concrete form tube	13 tubes	$7.25	$94.25	Sakrete	Organic
Concrete	Quikrete Gray High Strength Concrete Mix	2,400 lbs	$0.92 (18 lb/post)	$129	Quickcrete	Composite
L-Bracket	L bracket, zinc, 5”	27	$2.15	$58.05	Everbilt	Metal
Steel Post	Square Steel Tube 2x2x12 14 gauge	27	$31.69	$823.80	Discount Steel	Metal
3” C-Clamp	3” C Clamp	54	$9.94	$268.38	Husky	Metal
U-Bolt	#320 U-Bolt zinc	28	$1.30	$36.40	Everbilt	Metal
Camera track	Camera track, galvanized steel	130 ft	$15.25	$396.5	AmCraft Manufacturing, Inc	Metal
Track Connector	Beam flange connector, galvanized steel	12	$25.50	$306	AmCraft Manufacturing, Inc	Metal
Track Support	Beam flange split support, galvanized steel	14	$25.50	$357	AmCraft Manufacturing, Inc	Metal

*costs per each additional 5’ (1.52m) of track section added.
**Total cost for the 130’ (39.62m) design presented.

Appendix III. Chapter 2 Step-by-Step Build and Safety Instructions

Control box for providing power and commands to the motor.

Tools: Soldering iron, cordless drill w/ hole saw bits, phillips head screwdrivers.

1. **Wiring (Supplemental Figure 1).** In the control box, Attach male-to-female jumpers to the 4-pin connector for the limit switches. Attach control lines for the two relays and the limit switches to the GPIOs of the Raspberry Pi. See motorRun.sh for the specific GPIO configuration used. Attach two large wires (~18 AWG) to the 2-pin connector for the motor. Attach two large wires (~18 AWG) to the 2-pin connector for power. Attach the voltage regulator to the 12 V power lines, along with the common pins of the relays as in Fig. 1. The 12 V power lines are then connected to the Battery, housed in the waterproof Battery Box. Attach the NC and NO terminals of each of the relays respectively to one of the two wires for the motor connector, and the NO and NC terminals for the other wire, as in Fig. 1. Connect the Raspberry Pi to the output of the voltage regulator through a USB hub. Connect a USB cable to charge the Pocket Chip to the USB hub as well. Finally, connect the router to the 12 V power bus. All 12 V connections may be made by terminal strips. To prevent dust and moisture from entering the control box, ensure that all connectors to outside wires have an International Protection (IP) rating of 67 or higher.
2. **Solar Panels/ battery.** Attach the charge controller to the inside of the lid of the battery box. Insert the battery into the battery box. Attach a piece of 14-18 AWG wire between the positive battery terminal and the positive battery screw on the charge controller. Repeat for the negative terminal and screw. Attach the loose connectors for the solar panel to their respective screws on the charge controller. Attach the other sides of these connector to the solar panel. Attach the load side of the charge controller to the 12 V connections inside the control box.

Motor mount for waterproofing and mounting the motor

Tools: Miter saw, cordless drill, allen wrenches, phillips head screw driver

1. **Motorbox assembly (Supplemental Figure 2) .** The motor and timing belt pulley are mounted to a rectangular assembly made out of 2x4 treated lumber (Supplemental Figure 2). The motor used is a 12 VDC gear motor with a 42.3 mm (⅙") flattened shaft. Mount the motor in a 20 cm (7⅞") by 11.43 cm (4½") plastic enclosure (motor housing). The gear motor shaft is extended to 5 inches from the base of the waterproof motor box using a 5.08 cm (2") long metal shaft coupler. The shaft coupler is produced by boring a 42.33 mm (⅙") hole along the length of a solid metal rod. Drill two holes on the side of the coupler for the set screws. Once the motor housing is mounted to the wooden motorbox assembly, mount a wood spacer to the base of the motor shaft. The 42.33 mm (⅙") diameter bearing is then mounted to the wood spacer concentric with the motor shaft. Lastly, mount the timing belt pulley 1.27cm (½") from the end of motor shaft.
2. **Motorbox mounting on End Post (Supplemental Figure 3).** The motorbox assembly is mounted horizontally 11.43 cm (4½") from the top of the 3.05 m (10') wooden end post (Supplemental Figure 3). The plastic motor housing sits

square against the side of wooden end post with two metal corner brackets attached on the top and bottom of the motorbox assembly.

Trolley modifications for attaching the 360FLY camera and belt

Tools: Bandsaw, miter saw, drill press, phillips head screwdriver,

1. **Building the roller base.** Cut one 22.86 cm (9") by 5.40 cm (2⅛") rectangle out of polyethylene using a bandsaw. In the center of this rectangle, drill a 64 mm (¼") diameter hole for the camera bolt to pass through. Center the timing belt clamps at 1.59 cm (⅝") from both 5.40 cm (2⅛") ends of the polyethylene rectangle, and mark holes for the timing belt clamp bolts. Drill 32 mm (⅛") holes at these locations, and insert four timing belt clamp bolts fastened with four timing belt clamp nuts at each timing belt clamp, with the top of the bolt oriented on the opposite side of the rectangle as the timing belt clamp.
2. **Installing the rollers on the roller base.** Cut four, 2.22 cm (⅞") by 95 mm (⅜") rectangles from the polyethylene, rounding the edges on one 2.22 cm (⅞") inch side with a belt sander. Offset from the center of each rectangle, drill a 39 mm (5/32") hole. On the top of each rectangle, drill a ⅛" inch hole that does not intersect the 39 mm (5/32") hole. Next cut four, 3.81 cm (1½") segments of the roller dowel. For each segment of roller dowel, drill a 47 mm (3/16") hole lengthwise down the cylinder. Mark two, 5.72 cm (2¼") segments along the rod used for the roller axel and cut. Assemble the rollers by bolting down the small rectangles on one side of the roller base by pre-drilling 32 mm (⅛") holes 5.4 cm (2⅛") from both 5.40 cm (2⅛") roller base ends. Place the roller axles through each holes, ensuring a tight fit, epoxying if necessary. Then attach the drilled dowels, ensuring they roll freely. Finally, attach and fasten the other 2.22 cm (⅞") by 95 mm (⅜") rectangles to the other side of the roller base complete the rollers.
3. **Modifying the trolley to hold the camera.** Remove the existing hook on the trolley. In its place, place the camera bolt with the top side on the top of the trolley. On the camera bolt beneath the trolley, slide two camera spacers followed by a camera nut. Shave the outer edge of each camera spacer so that they fit between the bottom opening of the camera track. Then, slide on the assembled roller base. Fasten loosley with a camera nut and camera washer.

QR codes for field plot recognition in videos

Tools: Circular saw, palm sander, miter saw, cordless drill, paint roller and tray, masking tape

1. **Cutting the Plywood Panel.** Using a circular saw, cut one 60.96 cm (2') by 91.44 cm (3') panel out of plywood. Make sure that there are no imperfections on the board, and sand the plywood if necessary. Place weight on the board for a few days to minimize warping after cutting.
2. **Cutting the PVC Pipe.** Cut from the PVC pipe two, 76.2 cm (2½') PVC segments for use on the sides of the panel, and two 45.72 cm (1½') PVC segments for the short sides of the QR panel. Additionally cut four, 91.44 cm (3') segments for use as QR code legs from the PVC pipe.

3. **Assembling the PVC frame.** Insert two tee joints on both ends of each 60.96 cm (2½‘) PVC segment. Insert two elbow joints (Hub side) on both ends of the 45.72 cm (1½‘) PVC segments. Insert the spigot ends of the two elbow joints along one 45.72 cm (1½’) foot PVC segment into the hub ends of the tee Joints. Finally, insert the spigot ends on the elbow Joints of the remaining 45.72 cm (1½‘) PVC segment in the hub end of the T joints on the other end of the 60.96 cm (2½’) PVC segments.
4. **Installing the Plywood panel.** Place the assembled PVC frame on top of the plywood panel after it has been flattened, use eight pipe clips fastened with quarter hex bolts and quarter hex nuts, quarter washers to secure frame to panel. Fasten the PVC frame at two points along each side. Attach the four QR code legs to the exposed tee joints.
5. **Painting the QR pattern to create the final QR code.** Flip over the plywood panel with PVC frame and legs attached. Mark off six, 30.48 cm (1’) by 30.48 cm (1’) square sections on the plywood panel with painters tape. First paint one corner square on the plywood panel red to aid downstream image analyses. Mix the red paint with barium sulfate (50% by weight). Once the red square on the panel is dry, paint the other squares in checkered pattern using black and white paint. Mix the black and white paint separately with 50% barium sulfate by weight. The black and white squares will serve as the unique identifying pattern for each QR code.
6. **Repeat steps 1-5 for the remaining 7 QR codes**

Track Construction for installing the camera system in the field (Supplemental Figure 4)

Tools: Laser level, survey line, spray paint, survey flags, gas powered/bobcat mounted auger, magnetic post level, magnetic bubble level, ladders, wrenches, bracing wood, plumbob, rubber mallet, grease, phillips head screwdrivers.

1. **Marking the Steel Post locations.** Use a laser level and survey line to set a straight line across the center of the research field. Mark the endpoints of a 39.62 m (130’) line. This line represents the length of the 39.62 m (130’) of camera track, and serves to center construction of the camera system. At one of these endpoints, make a mark (paint or flag) that is 6.35 cm (2.5”) in a direction perpendicular to the center line for the first steel post. Make an additional marking 1.52 m (5’) down the line,on the side opposite the first 6.35 cm (2.5”) perpendicular mark from the center line. This mark is where the next steel post will be placed. Continue these markings every 1.52 m (5’), alternating sides of the center line for the steel posts.
2. **Installing the Steel Posts.** Prior to setting each steel post in the ground, attach an L-bracket with two, 7.62 (3”) C-clamps to the top of the steel post. Orient the C-clamp so that the tightening screw is on the side of the post opposite the L-bracket. Mark with masking tape two feet from the base of the steel post as a guide when setting the post in the ground. Once the locations for the end posts and steel posts have been marked, use an 20.32 cm (8”) diameter auger to drill a

hole two feet deep into the ground centered at each location marked along the camera track line. Place form tubes within each hole. Set the steel post into the first steel post hole with a form tube. Make sure that the face of the steel post is square with the center line, and 6.35 cm (2.5") from the center line. Using a magnetic post level to keep the steel post plumb, pour in dry concrete and add water simultaneously, mixing with a stick. Once mixed into the for tube, place bracing wood to keep the steel post level while the concrete sets. Set the next steel post in the same manner, 6.35 cm (2.5") from the center line on the opposite side. Continue this for the remaining 25 posts, ideally using a wooden jig to ensure post alignment.

3. **Suspending the camera track.** Suspend each 3.04 m (10') camera track section by first attaching a track connector on one end and a track support in the middle. Adjust the height of the L-brackets with the 7.62 cm (3") C-clamps on the posts so that the bottom of the camera track is 2.74 m (9') above the ground. Make sure the 3.04 m (10') section of camera track is level by using a bubble (spirit) level. Once the camera track is leveled, tighten the clamps on top of the track connector and track support pieces so they are secured to the L-brackets. Continue this process for the remaining track sections until 39.62 m (130') of track is laid.
4. **Installing the End Posts.** Mark end post holes at each end of the camera track, 60.96 cm (2') away from the last steel posts in line with the center of the camera track. Use an 20.32 cm (8") auger to drill a hole 60.96 cm (2') deep at the center of each marking. Place a form tube within each hole. Set the end post with the motor mount attached into one of the holes at the end of the center line. Align the end post so that the timing belt pulley of the motor mount is centered on the track centerline. Set the other end post with the end pulley mounted in the other hole at the end of the center line. Align this end post so that the end pulley is centered on the track center line. Once the end posts are set, attach the control box to the end post with the attached motor mount.
5. **Installing QR codes.** Insert the Trolley into the camera track with Use a plumbob suspended from the trolley to ensure that the QR code center is in line with the track center. Space a QR code every 4.95 m (16'¼") along the camera track. Use the suspended plumbob to ensure that the center of the QR code is directly underneath the camera track at each QR code location. Once centered, use a rubber mallet to set the PVC legs into the ground. Ensure that the QR code panel (top) is 76.2 cm (2.5') above ground level.
6. **Cleaning and greasing the camera track interior.** Dirt will likely have entered the camera track interior during the installation process. Clean the track of dirt by inserting rags into the track interior, followed by the trolley. Pull the trolley along the length of the camera track from below using a string, pushing the wad of rags along to remove dirt from the interior track surface. After removing dirt, apply large amounts of grease (White Lightning is recommended) to the trolley wheels. Pull the trolley along the length of the track, spreading the grease along the interior track surface. Once finished, slide the finished camera trolley assembly

with roller base into the camera track, and tighten the camera nut so that the roller base is tight against the spacers.

7. **Installing the Timing Belt.** In the field, attach one end of the belt (toothed-side facing towards the camera track) to the timing belt clamp on the roller base. Thread the other end down the camera track and around the timing belt pulley of the motor mount. Thread the belt back along the 39.62 m (130') camera track span and around the end pulley, reattaching to the other side of the roller base using the other Timing Belt Clamp. Prior to tightening the Timing Belt Clamp, cut the Timing Belt to size.
8. **Tensioning the Timing Belt.** Place a 20.32 cm (8") dowel segment through the support pulley bore. Cut a 10.16 cm (4") segment of PVC pipe and insert a bearing so that it is flush with one end of the pipe segment. Insert the dowel segment with pulley attached through the bearing bore. Above the camera track, space 5 support pulleys at regular intervals using 6.35 cm (2.5") C-clamps. Adjust height as necessary to tension the timing belt. Construct belt rollers in the same fashion, except use a 40.64 cm (16") dowel segment without a support pulley attached. Space 3 belt rollers approximately 12.19 m (40') from each other and 60.96 cm (2') below the camera track on the steel posts with 6.35 cm (2.5") C-clamps to the PVC pipe.

Wiring Limit Switches for optional automated use

Tools: phillips head screwdrivers, zip ties.

1. Connect one end of the cable to the relays in the control box
2. Run the short end of the cable to the first Steel Post from the end post with mounted control box.
3. Attach the limit switch to the end section of the camera track, so that it will be tripped when the roller base approaches the switch.
4. Run the long end of the cable down the entire span of the camera track, attaching using zip ties to the top of the steel posts. Make sure that the cable does not fall below the top of the camera track, as it will interfere with field imaging by the camera.
5. On the other end post with the end pulley, attach the other limit switch to the opposite end section of the camera track, so that it will be tripped when the roller base approaches the switch.
6. Wire the Cable to these limit switches.

Operation Instructions

1. View the help page on the Raspberry Pi Foundation website if unfamiliar with setting up a Raspberry Pi computer.
2. Connect to wifi of the control box and open a linux terminal on a laptop or Pocket Chip.
3. SSH into the raspberry pi using name of the Raspberry Pi as the username, and specified password as the password.
4. Once a connection with the Raspberry Pi is established, turn on the camera and start recording using the 360 FLY app.

5. Once the camera is on and recording, execute the `motorRun.sh` script in the linux terminal.
6. The camera will begin moving forward. Trolley will reverse direction once a limit switch on the other end of the track is tripped. When the limit switch on the control box end is triggered the trolley attached the camera will stop.
7. To stop the camera at any point during this script execution, hold control ^c. This will halt the shell script execution. However, the motor will still be running. To stop the motor, execute `STOP.sh`. This will stop the motor.
8. The camera can also be run without the limit switches. Execute `motorForward.sh` and `motorReverse.sh` to move the camera in opposite directions along the track. After executing either of these scripts, stop the motor by executing `STOP.sh` (there is no need to press control ^c). The limit switches will not function if using these scripts.
9. Once a camera run has stopped, use the 360 FLY app to stop camera recording and to power off the camera.
10. Videos can then be uploaded remotely from the 360 FLY app to cloud storage, or downloaded from the 360 FLY camera onto a computer once the camera is removed from the hardware.
11. The `motorRun.sh` script can be scheduled to operate at certain times, enabling automatic operation of the phenotyping system. To do this, open the Cron scheduler in the linux terminal while the ssh connection with the Raspberry Pi is established. Open a text editor to edit the Cron scheduler by typing `crontab -e`. Schedule the `motorRun.sh` script to execute at 12:00 noon every day for example, type `0 12 * * * /path/motorRun.sh`. Then exit crontab. NOTE: While Cron scheduling schedules regular motion of the camera, recording of the camera is still not automatic. Additional servos to manually press the power and record button on the 360FLY camera will be necessary to have fully automated video recording using this hardware.

Safety: The safest operation of this hardware is obtained when all clamps (C-clamps, Track Connectors, and Track Supports) are firmly clamped onto their respective surfaces. When sufficiently clamped, each C-Clamp has a clamping force of 226.8 kg, which in combination with the other C-clamps is sufficient to hold the weight of the camera track. To avoid any collapses when installing this hardware, make sure that the C-clamps are fully gripping the L-brackets and the steel posts. Do not install or stand near this installed hardware in the field when thunderstorms are imminent. Finally, do not install this hardware adjacent to or underneath power lines.

Appendix IV. Chapter 2 Supplemental Figures 1-4

Supplemental Figure 1. Control Box wiring diagram

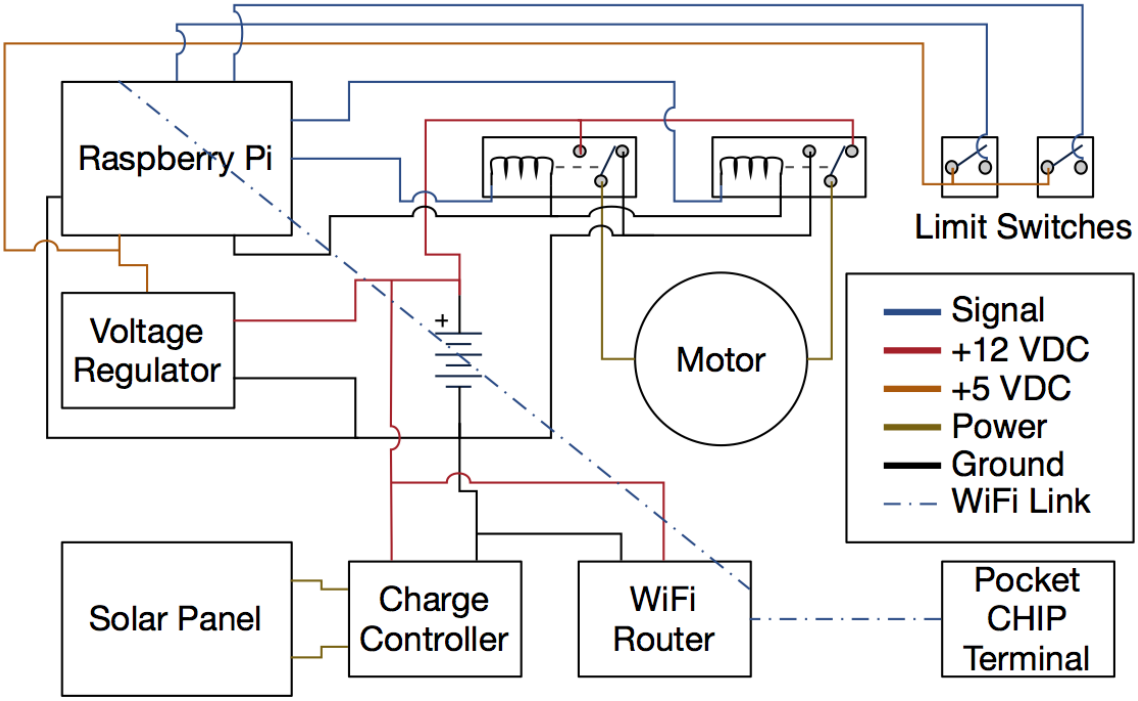

Supplemental Figure 2. Motor and Pulley Mound

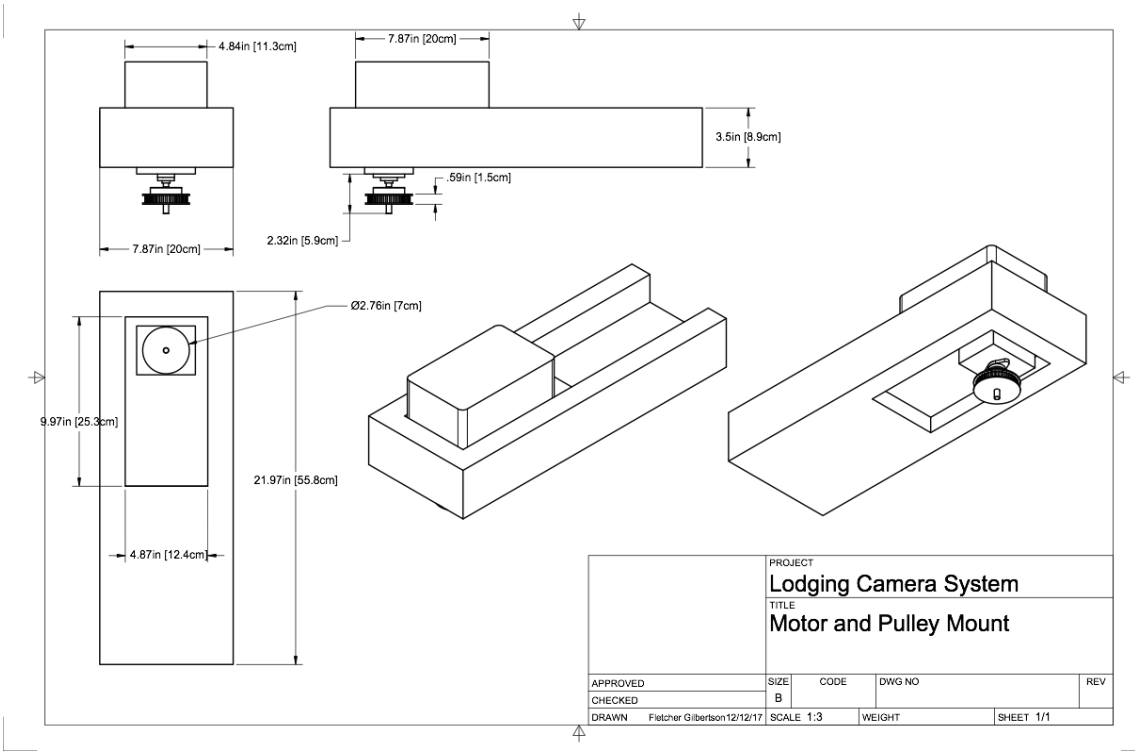

Supplemental Figure 3. Motor Post End Assembly

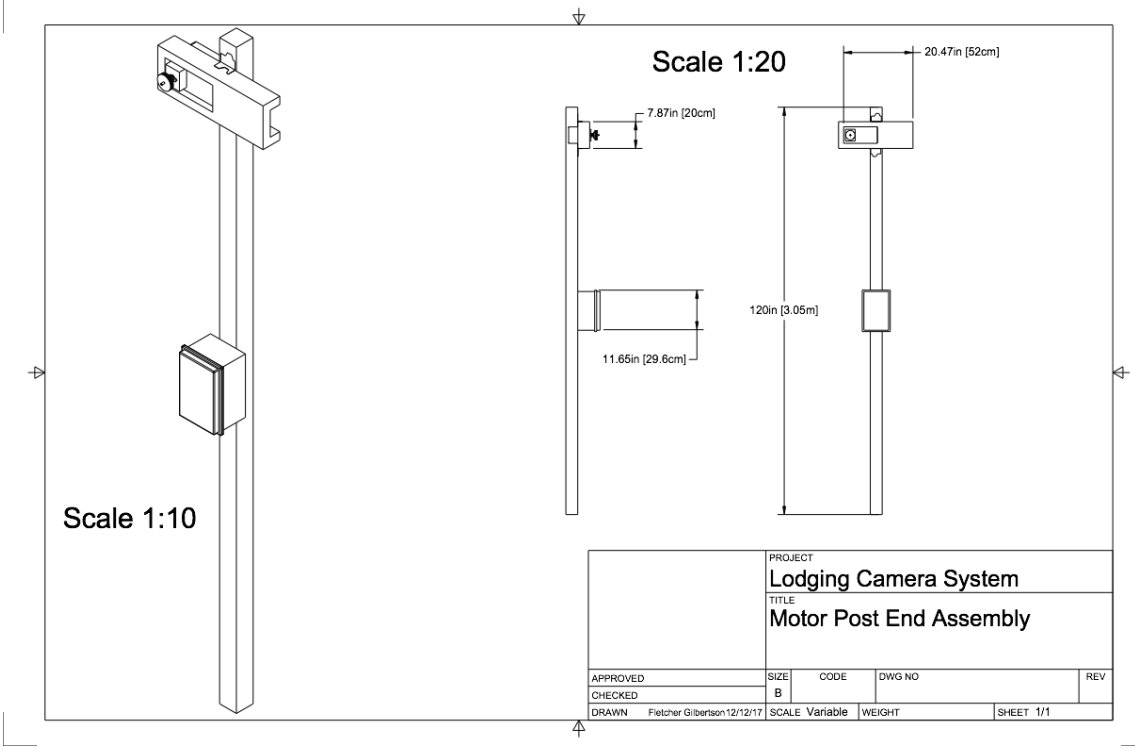

Supplemental Figure 4. Final Track Assembly

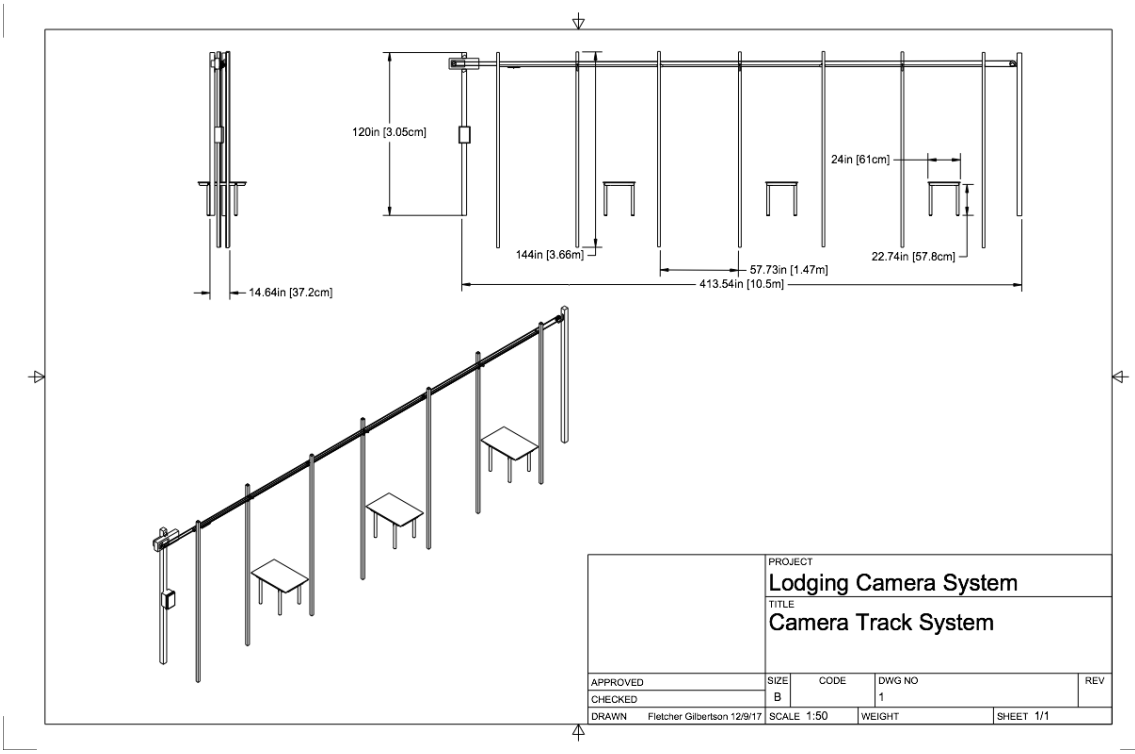
120in [3.05cm]
24in [61cm]
144in [3.66m]
57.73in [1.47m]
22.74in [57.8cm]
413.54in [10.5m]
14.64in [37.2cm]
PROJECT
Lodging Camera System
TITLE
Camera Track System
APPROVED
CHECKED
DRAWN Fletcher Gilbertson 12/9/17
SIZE B
CODE
DWG NO 1
REV
SCALE 1:50
WEIGHT
SHEET 1/1

Appendix V. Chapter 4 Supplemental Material
Supplementary Material

Video of CL_r bending curve. Coordinates *x*,*y* at the end of length *h* are plotted continuously over frames, while the windward edge and stem bending curve are shown at each frame. Empirically generates the red arc shown in Figure 2 and describe in Equations 8a-8e.
https://drive.google.com/open?id=1CS4JfrGRyuqW8ZqtoMfm4gDmtnYfY-iG

Section 1
The power curve fitting the windward edge of the plant with scaling coefficient *c* and power law exponent *d* (Eq. 1)

$$f(x) = cx^d$$

Given the known force required to bend all stems at half-height (*h*) to 50 degrees, the *x* distance where *h* makes a 50° angle with the floor of the wind tunnel is found through (Eq. 2) (Methods figure 4):

$$x = h \operatorname{cosd} 50$$

This *x* distance is used to approximate the bending angle at any frame through (Eq. 3) (Methods figure 5,6)

$$\Theta = \tan^{-1}\frac{f(x)}{x}$$

The area of the cereal as imaged by the side-view camera increases with velocity in the wind tunnel as leaves are blown behind the stems. This side area view of the plant that mostly constitutes leaves is not relevant to drag coefficient estimation, because it is not the frontal area exposed to the airstream. The following equations derive the formula for approximating the frontal area of the cereal at the time of drag coefficient estimation based on the side area in view of the camera when the cereal reaches the standard deformation point.

Assume the volume of the cereal is cylindrical, and that the volume occupied by the cereal conserved through the wind tunnel test (Eq. 4a):

$$Vol = \frac{\pi D^2}{4} H$$

The frontal area of the cereal in the first frame of each video prior to bending (A_{init}) can be represented as (Eq. 4b-c):

$$A_{init} = HD$$

$$D = \frac{A_{init}}{H}$$

Given the conserved volume throughout the test, the width of the cereal L_{leaf}(m) multiplied by the area of the leaves in view of the camera A_{leaf}(m2) is equivalent to (Eq. 4d):

$$L_{leaf}A_{leaf} = \frac{\pi D^2}{4}H$$

Which after substituting Eq. 4c within Eq. 4a yields (Eq. 4e):

$$\frac{\pi {A_{init}}^2}{4H^2}H$$

The non-projected frontal area is thus the product of the height of the plant and the width of the cereal (Eq. 4f):

$$HL_{leaf} = \frac{H\pi {A_{init}}^2}{4HA_{leaf}} = \frac{\pi {A_{init}}^2}{4A_{leaf}}$$

With the frontal area A projected at bending angle Θ in direct contact with the airstream at the time of the standard deformation for drag coefficient estimation (Eq 4g-h):

$$A = HL_{leaf}\sin\Theta$$
$$A = \frac{{A_{init}}^2}{A_{leaf}}\sin\Theta$$

Supplemental Figure 1. Visual representation of frontal area A calculation at the standard deformation. A) Eqs. 4a-c B) Eqs. 4d-e C) Eq. 4f D) Eq 4g-h. Red arrows indicate the direction of airflow in the wind tunnel

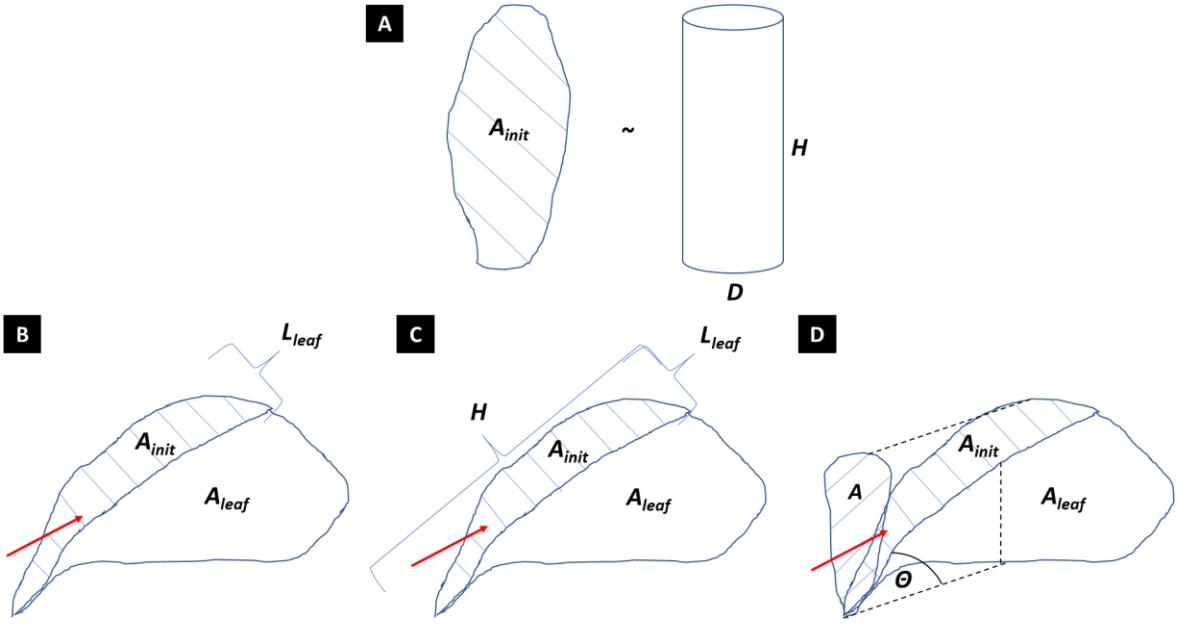

Section 2

Plant drag coefficients are estimated using environmental data from the pitot tube. By estimating the vapor pressure of humid air in (Pascals, Pa) in the wind tunnel (Eq 5a):

$$p_{vap} = 100\left(6.1078\left(10^{\frac{7.5(T_{dp})}{237.3+T_{dp}}}\right)\right)$$

We estimated the vapor pressure of dry air (Pa) (Eq 5b):

$$p_{dry} = 100(p_{atm} - p_{vap})$$

Which was used to calculate the density of humid air (kg/m^3) (Eq 5c):

$$\rho_{air} = \frac{p_{dry}}{R_{air}T} + \frac{p_{vap}}{R_{vap}T}$$

And finally the velocity *u* of the air (m/s) at each second of the video (Eq 5d):

$$u = \sqrt{\frac{19.6(q\rho_{Hg})}{1000(\rho_{air})}}$$

Given the known force required to bend a plant to 50°, the frame where $\Theta = 50°$ uses the velocity of air, density of air, and projected area at that moment to estimate the drag coefficient (Eq 5e):

$$c_d = \frac{2F}{\rho_{air} u^2 A}$$

The Reynolds number is estimated at the standard deformation by dividing the velocity u by the kinematic viscosity of air v at 20°C (1.15×10^{-5} m^2/s) (Eq 5f):

$$R_e = \frac{uH}{v}$$

Section 3

The coefficient of lodging resistance (CL_r) represents the proportion of torque resisted by the stem to that applied to the stem. The applied torque in the wind tunnel is due to the force F of drag due to wind, which is equivalent to that measured by the load cell when the plant is manually bent at a 50° angle. The CL_r expresses a point along a bending stem in terms of the x,y displacements of a force at an initial height b in elliptical form (Eq 6) (Grafius and Brown 1954) (Figure 2A-B):

$$x^2 = a^2 \left(1 - \frac{y^2}{b^2}\right)$$

With the distance a representing the diameter of the ellipse along the x axis and varying with the x and y displacement of the point on the stem under the known force F (Eq 7a) (Grafius and Brown 1954) (Figure 2A-B):

$$a = x \sqrt{\frac{1}{1 - \frac{y^2}{b^2}}}$$

With the CL_r determined using these x,y displacement values, initial height b, and distance a for the frame where the drag force F is known (Eq 7b) (Grafius and Brown 1954):

$$CL_r = \frac{aF}{bx}$$

Assuming the known drag force F acts at the halfway point along the stem, we derive a way to calculate the x and y displacements of any point along a length of stem (h) relative to the plant base (origin) for any frame in the video. Integration is used to calculate the length of the fitted curve representing the windward edge of the stems, and to capture the

x and *y* displacement points relative to the origin. Taking the first derivative of the power curve (Eq. 1) yields the slope at any point along the fitted curve (Eq 8a):

$$f'(x) = cdx^{d-1}$$

With the length of the curve found by integrating from the minimum *x* value of the windward edge (x_{min}) value to the maximum *x* value (x_{max}) of the windward edge over the function below (Eq 8b):

$$\int_{x_{min}}^{x_{max}} \sqrt{1 + f'(x)^2}$$

Then by defining a function $g(x_{max})$ whose solution at length *h* along the stem is equal to 0, we can find the value of x_{max} that produces a length along the curve equivalent to *h* (Eq 8c-d):

$$g(x_{max}) = \left(\int_{x_{min}}^{x_{max}} \sqrt{1 + f'(x)^2} \right) - h$$

$$x = g(x_{max}) = 0$$

Finally, the *y* coordinate of the point on the stem at length *h* is obtained by finding the fitted value along the power curve for the *x* coordinate x_{max} (Eq. 8e):

$$y = f(x_{max})$$

Appendix VI: Chapter 5 Supplemental Material

Supplemental Table S1. Moran's I estimates for mean frequency at each video date, planting date combination

Video date	30 Apr 2018	7 May 2018	15 May 2018	22 May 2018
11 Jun 2018	0.12589*	-0.060101	na	na
14 Jun 2018	0.061126	-0.081627	0.26497*	0.0055941
15 Jun 2018	-0.027412	0.32115*	-0.053657	0.005156
20 Jun 2018	0.13806*	0.22317*	-0.060203	-0.057801
21 Jun 2018	-0.0022694	-0.040885	-0.029124	0.12442*
25 Jun 2018	0.072869	-0.058239	0.0041417	0.037925
28 Jun 2018	0.084986	0.06597	0.13614*	0.32851*
29 Jun 2018	-0.10542	-0.093727	0.15343*	0.047324
02 Jul 2018	-0.073282	-0.029488	0.19337*	-0.072333
09 Jul 2018	-0.083431	0.17999*	0.092953	-0.011729
16 Jul 2018	0.08608	-0.085814	-0.096273	0.41488*

*** indicates a value significantly greater than 0.**

Supplemental Table S2. Moran's I estimates for Hz0.9 amplitude at each video date, planting date combination

Video date	30 Apr 2018	7 May 2018	15 May 2018	22 May 2018
11 Jun 2018	0.040243	0.0042576	na	na
14 Jun 2018	0.062506	0.07472	-0.007546	0.070597
15 Jun 2018	-0.013225	0.043209	-0.02185	0.20016*
20 Jun 2018	-0.003476	0.073577	-0.093873	-0.055692
21 Jun 2018	-0.055026	0.0070314	-0.073493	-0.052377
25 Jun 2018	-0.061367	0.094169	-0.010333	-0.081751
28 Jun 2018	0.037452	0.094978*	0.13454*	-0.024825
29 Jun 2018	-0.066336	0.098946*	0.0013545	0.057092
02 Jul 2018	0.077778	0.098205*	-0.058706	0.023591
09 Jul 2018	-0.041072	0.1064*	0.10548*	-0.10925
16 Jul 2018	0.084131*	-0.03715	0.15535*	0.11894*

*** indicates a value significantly greater than 0.**

Supplemental Table S3. Predicted mean heights (cm) by cultivar and crop for each growth stage

Genotype	Tillering†‡	Elongation†‡	Heading†‡	Dough†‡	Maturity†‡
'Gopher'	21.11EF*	57.71C	78.62A	102.58A	105.20A
IL078721	24.96ABC	59.75AB	61.49G	72.29IJ	73.98I
ND021052	19.42FG	54.17DE	71.15B	97.44B	99.03B
'Reins'	24.87BC	60.39A	68.17D	80.31D	82.57CDE
'AC Metcalf'	25.22ABC	52.21F	64.54F	77.77EF	80.61DEF
'Conlon'	25.70AB	58.43BC	66.43DE	75.91FG	77.65FGH
'ND Genesis'	23.76CD	53.78E	68.33CD	80.32CD	83.01CDE
'Pinnacle'	19.74FG	48.43 G	63.87F	77.94E	80.09EF
'Celebration'	25.52ABC	58.35BC	71.79B	81.30CD	83.79C
'Quest'	22.69DE	59.23AB	71.78B	82.22C	84.61C
'Stellar ND'	23.01D	55.36D	65.36EF	75.24GH	77.86FG
'Tradition'	26.82A	57.35C	70.33BC	81.36CD	83.51CD
'Linkert'	16.75H	42.09H	56.02IJ	70.41J	72.05I
MN113946	17.16H	41.96H	59.55H	80.63CD	82.63CDE
'Rollag'	17.94GH	39.38I	57.40I	75.13GH	77.18GH
'Shelly'	18.32GH	40.03I	54.33J	73.73HI	74.83HI
Oat	22.76B	57.84A	69.63A	87.19A	89.51A
2-row Barley	23.94A	53.24B	65.13B	77.95C	80.45B
6-row Barley	24.08A	57.61A	70.17A	80.52B	82.90B
Wheat	17.67C	40.85C	57.27C	75.62D	76.96C

†indicates a that the cultivar genotypic effect was observed in the growth stage according to the LME model

‡indicates a that the crop genotypic effect was observed in the growth stage according to the LME model

***Unique letters indicate significantly different means at alpha = 0.05**

Supplemental Table S4. Predicted mean internode 23 diameters (mm) by cultivar, crop for each growth stage.

Genotype	Tillering†‡	Elongation†‡	Heading†‡	Dough†‡	Maturity†‡
'Gopher'	3.05GHI*	4.17EFG	4.08D	4.09D	4.13DE
IL078721	3.72CDE	4.27E	4.49C	4.64AB	4.64AB
ND021052	3.64DEF	4.57CD	4.52C	4.31CD	4.19CDE
'Reins'	3.95BCD	4.50D	4.65B	4.79A	4.76A
'AC Metcalf'	3.50EF	4.018GH	3.79EF	3.60E	3.62F
'Conlon'	3.36FG	4.06FG	3.67F	3.43EF	3.36FG
'ND Genesis'	3.17GH	3.88H	3.91E	4.20D	4.14 CDE
'Pinnacle'	3.59EF	4.22EF	4.12D	4.14D	4.12E
'Celebration'	4.53A	4.81AB	4.61BC	4.47BC	4.43BCD
'Quest'	4.14B	4.59CD	4.49C	4.21D	4.18CDE
'Stellar ND'	4.57A	4.94A	4.73AB	4.54B	4.46ABCD
'Tradition'	4.02BC	4.69BC	4.79A	4.51BC	4.47ABC
'Linkert'	2.78IJ	3.68I	3.67F	3.50EF	3.45F
MN113946	2.55JK	3.51I	3.30H	3.10G	3.08G
'Rollag'	2.97HI	3.61I	3.51G	3.33F	3.33FG
'Shelly'	2.31K	3.32J	3.50G	3.38F	3.42F
Oat	3.59B	4.38B	4.45B	4.51A	4.49A
2-row Barley	3.41B	4.04C	3.88C	3.81B	3.78B
6-row Barley	4.32A	4.76A	4.64A	4.43A	4.39A
Wheat	2.65C	3.53D	3.48D	3.30C	3.30C

†indicates a that the cultivar genotypic effect was observed in the growth stage according to the LME model

‡indicates a that the crop genotypic effect was observed in the growth stage according to the LME model

***Unique letters indicate significantly different means at alpha = 0.05**

Supplemental Table S5. Fitted effects internode 23.56 diameter ratios by cultivar, crop for each growth stage.

Genotype	Tillering†	Elongation†‡	Heading†‡	Dough†‡	Maturity†‡
'Gopher'	0.99B*	1.27ABC	1.31ABCD	2.10DE	2.15BC
IL078721	1.27A	1.03D	1.11GH	2.05E	2.13BC
ND021052	1.17AB	1.21ABC	1.26CDEF	2.05E	2.04CD
'Reins'	1.24A	1.16BCD	1.40AB	2.37B	2.43AB
'AC Metcalf'	1.02B	1.27ABC	1.27CDE	2.16CDE	2.28BC
'Conlon'	1.11AB	1.22ABC	1.42A	2.59A	2.66A
'ND Genesis'	1.08AB	1.19ABC	1.24DEFG	2.14CDE	2.25BC
'Pinnacle'	1.13AB	1.21ABC	1.42AB	2.66A	2.67A
'Celebration'	1.12AB	1.31A	1.29BCDE	2.34BC	2.38AB
'Quest'	1.16AB	1.28AB	1.38ABC	2.25BCD	2.24BC
'Stellar ND'	1.14AB	1.25ABC	1.17EFGH	2.10DE	2.16BC
'Tradition'	1.16AB	1.27ABC	1.32ABCD	2.18CDE	2.23BC
'Linkert'	1.16AB	1.28AB	1.07H	1.72FG	1.75DE
MN113946	1.13AB	1.25ABC	1.12GH	1.55FG	1.58E
'Rollag'	1.16AB	1.20ABC	1.14FGH	1.73F	1.80DE
'Shelly'	1.13AB	1.14CD	1.11GH	1.52G	1.57E
Oat	1.17	1.17B	1.34A	2.14B	2.20B
2-row Barley	1.08	1.22AB	1.34A	2.40A	2.49A
6-row Barley	1.15	1.28A	1.29AB	2.22B	2.25B
Wheat	1.14	1.22AB	1.11C	1.63C	1.68C

†indicates a that the cultivar genotypic effect was observed in the growth stage according to the LME model

‡indicates a that the crop genotypic effect was observed in the growth stage according to the LME model

***Unique letters indicate significantly different means at alpha = 0.05**

Supplemental Figure S1. Raster stack by video date of mean frequency values (Hz)*.

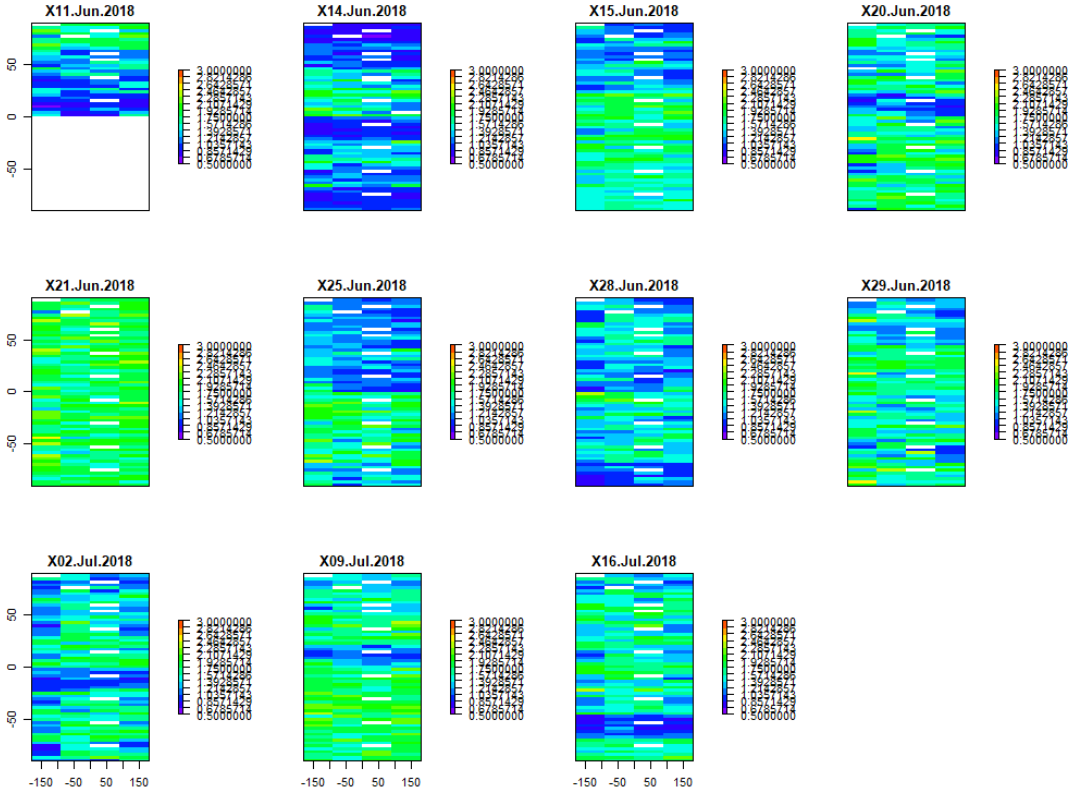

* y axis lables: 50 denotes the boundary between the 1st and 2nd planting dates, 0 denotes the boundary between the 2nd and 3rd planting dates, and -50 denotes the boundary between the 4th and 3rd planting dates.

Supplemental Figure S2. Raster stack by video date of amplitude values (dB) in the 0.9-1.1 Hz frequency bin.

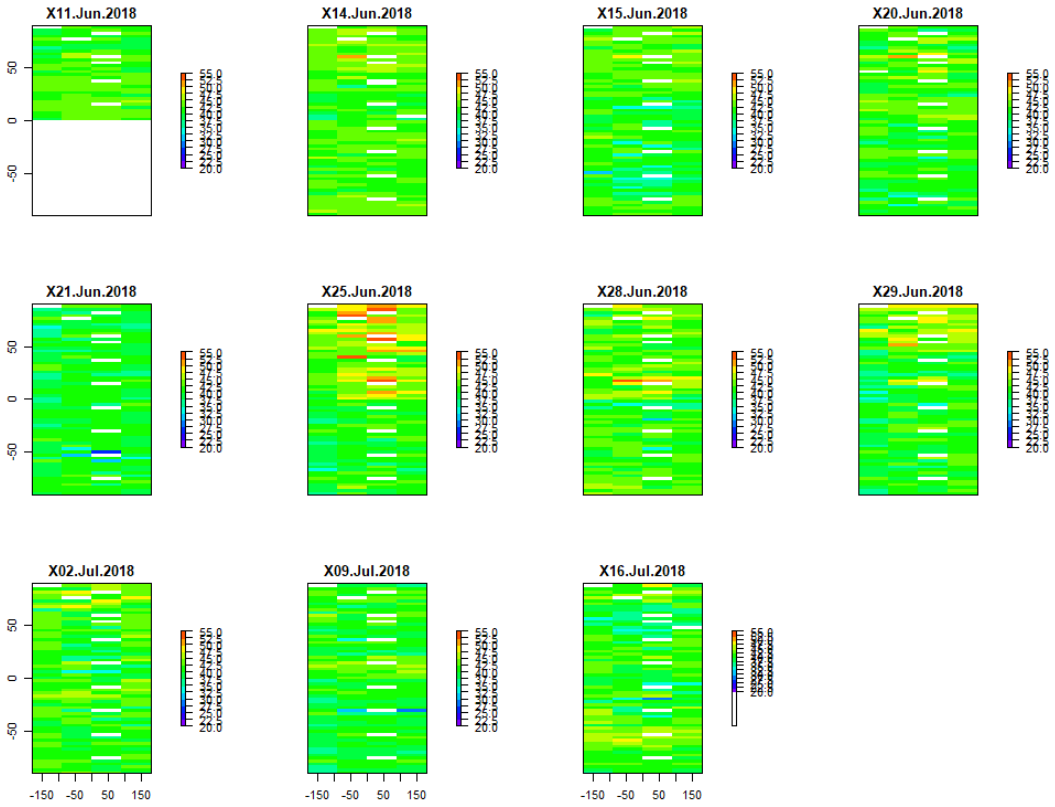

* y axis lables: 50 denotes the boundary between the 1st and 2nd planting dates, 0 denotes the boundary between the 2nd and 3rd planting dates, and -50 denotes the boundary between the 4th and 3rd planting dates.

Supplemental Figure S3. Raster of lodging angle data induced following the storm on 1 Jul 2018.

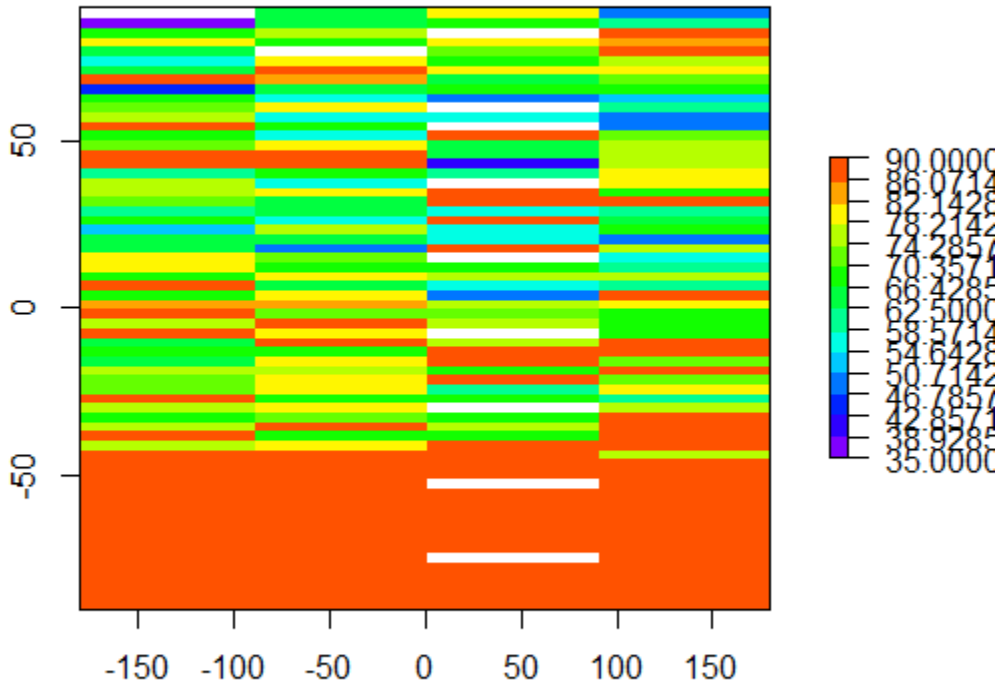

* y axis lables: 50 denotes the boundary between the 1st and 2nd planting dates, 0 denotes the boundary between the 2nd and 3rd planting dates, and -50 denotes the boundary between the 4th and 3rd planting dates.

Supplemental Figure S4. Scatterplots of mean frequency and physiology relationships, with observations color coded by average wind speed on the video date they were obtained.

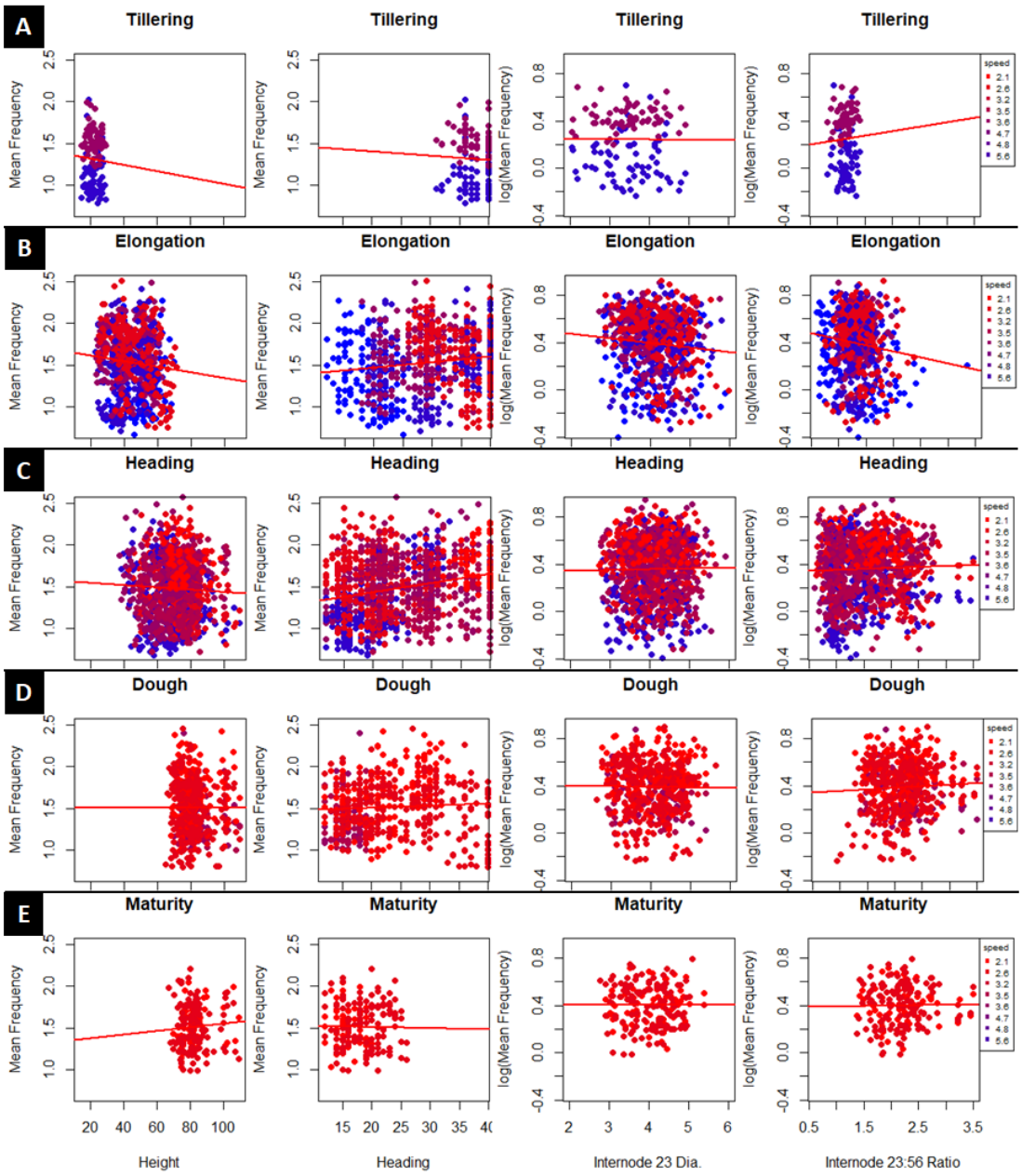

Supplemental Figure S5. PCAs by growth crop, growth stage. Color coded by line.

Crop	elongation	heading	dough	maturity
2-row	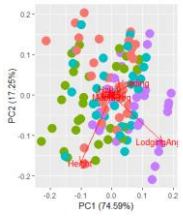	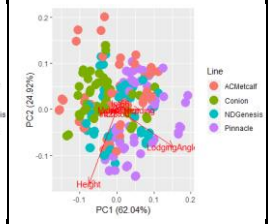	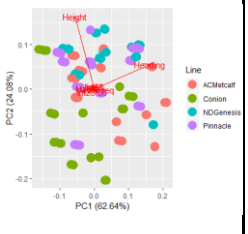	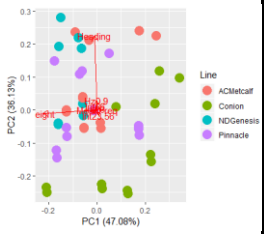
6-row	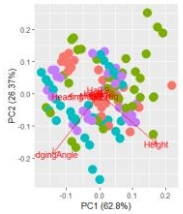	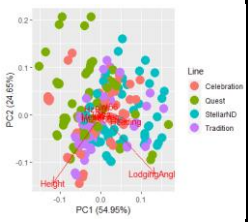	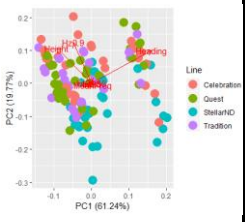	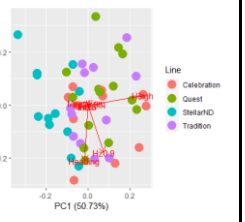
Oat	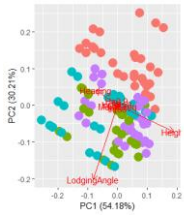	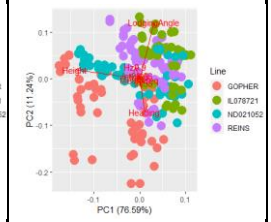	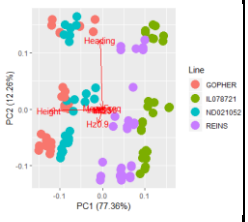	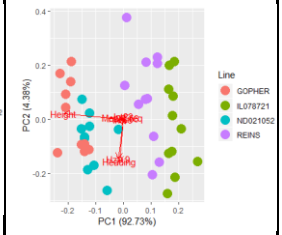
Wheat	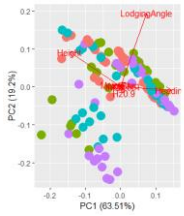	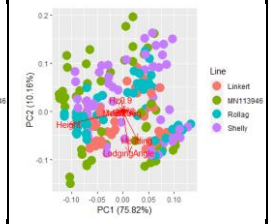	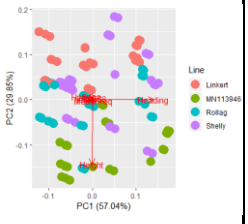	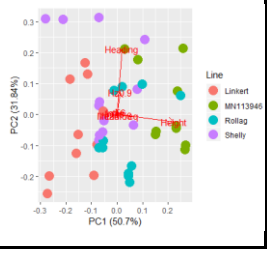

Appendix VII: Chapter 6 Supplemental Material

Supplemental Table S1. Linkage group statistics for biparental population cross A (P0528A1-1/SD090880).

LG	N Markers	Length (cM)	Avg Spacing	Max Spacing	Consensus R^2
Mrg01a	29	48.8639	1.745139	22.51389	0.47055
Mrg01b	27	96.22165	3.700833	25.55533	0.150847
Mrg01c	27	100.6344	3.870554	22.4143	0.994616
Mrg01d	24	73.35338	3.189277	24.13509	0.923418
Mrg02a	22	170.4319	8.115805	52.71328	0.972844
Mrg02b	23	71.63328	3.256058	26.73943	0.991088
Mrg02c	20	206.1862	10.8519	82.36206	0.987415
Mrg02d	19	76.93839	4.274355	19.13513	0.998604
Mrg03a	18	35.64727	2.096898	18.89207	0.029673
Mrg03b	15	19.65686	1.404062	3.491081	0.839611
Mrg04a	15	16.11069	1.150763	4.018423	0.83756
Mrg05a	15	94.28822	6.734873	33.91455	0.988326
Mrg05b	13	15.27931	1.273276	7.051805	0.983078
Mrg06a	14	109.6286	8.43297	40.17856	0.984265
Mrg06b	12	28.7199	2.6109	13.39465	1
Mrg08a	13	123.3501	10.27917	53.4643	0.85236
Mrg08b	11	57.55042	5.755042	23.91548	0.987241
Mrg09a	12	153.7734	13.9794	54.51338	0.921983
Mrg09b	11	11.11445	1.111445	3.26781	0.96172
Mrg09c	11	12.36899	1.236899	4.016432	0.670829
Mrg09d	9	50.47194	6.308993	32.05375	0.952697
Mrg11a	8	8.929514	1.275645	3.651818	0.952995
Mrg11b	9	86.92464	10.86558	37.06528	0.996257
Mrg11c	7	71.4053	11.90088	38.74475	0.986948
Mrg12a	8	26.83136	3.833051	17.02642	0.998603
Mrg13a	8	14.19763	2.028233	8.782419	0.187473
Mrg15a	8	43.66461	6.237801	19.24475	0.932799
Mrg15b	7	2.123765	0.353961	0.72511	0.225229

Mrg17a	7	50.65187	8.441979	38.92423	0.486458
Mrg17b	7	75.10636	12.51773	46.74911	0.996403
Mrg17c	7	77.03894	12.83982	51.45803	0.953786
Mrg18a	7	56.04015	9.340024	22.87267	0.15153
Mrg18b	7	27.27873	4.546455	16.09281	0.690218
Mrg19a	7	48.10699	8.017832	22.78376	0.982343
Mrg19b	6	46.76843	9.353687	18.77942	NA
Mrg20a	6	5.598264	1.119653	2.674244	0.965898
Mrg20b	6	4.852676	0.970535	3.796549	0.989633
Mrg20c	5	2.690304	0.672576	1.208788	0.214901
Mrg20d	6	88.19189	17.63838	57.87389	0.878019
Mrg21a	4	16.32462	5.441541	11.08426	0.96953
Mrg21b	5	23.1736	5.793401	22.19183	0.979388
Mrg23a	5	19.13052	4.78263	6.36996	0.622475
Mrg23b	5	3.042696	0.760674	2.37419	0.911408
Mrg23c	4	12.65427	4.218091	6.693733	NA
Mrg24a	3	11.83373	5.916865	11.57289	0.89332
Mrg24b	4	11.35176	3.78392	7.819698	NA
Mrg24c	4	7.24477	2.414923	7.24475	0.991498
Mrg24d	4	0.521182	0.173727	0.262515	NA
Mrg28a	3	3.285494	1.642747	2.273853	0.84928
Mrg28b	3	32.14759	16.07379	30.78909	0.724072
Mrg33a	16	13.60819	0.907213	1.934485	1
Mrg33b	10	30.8139	3.423767	23.60164	0.102672
Mrg33c	18	34.79289	2.046641	10.95467	0.81495
Mrg33d	20	62.02254	3.264344	13.74943	0.997201

* NA in R2 indicates that only 1 marker on the LG had a map position in the oat consensus map

Supplemental Table S2. Linkage group statistics for biparental population cross B (P0528A1-1/SD111736).

LG	N Markers	Length (cM)	Avg Spacing	Max Spacing	Consensus R^2
Mrg01a	27	37.66154	1.448521	26.45309	0.929777
Mrg01b	23	145.9396	6.633619	31.00643	0.625021
Mrg01c	21	34.02872	1.701436	15.12182	0.99984
Mrg02a	20	79.23551	4.17029	17.87704	0.888766
Mrg03a	17	156.9855	9.811593	127.0056	0.951323
Mrg03b	19	191.3933	10.63296	85.54506	0.916483
Mrg05a	18	115.348	6.785176	24.21753	0.092092
Mrg05b	14	95.41226	7.339404	25.78844	0.962077
Mrg08a	14	105.6817	8.129365	42.87074	0.973643
Mrg08b	14	11.50261	0.884816	4.250951	0.972044
Mrg09a	13	31.4385	2.619875	13.74248	0.863724
Mrg09b	13	117.5078	9.792314	59.73732	0.996131
Mrg11a	13	36.51643	3.043036	9.975386	0.013417
Mrg11b	12	89.29347	8.117588	40.4725	0.456021
Mrg12a	12	36.16334	3.287577	20.79498	0.824742
Mrg12b	12	67.87344	6.170312	30.52222	0.941576
Mrg12c	11	93.24261	9.324261	51.95537	NA
Mrg12d	10	52.40757	5.823064	21.61246	0.949455
Mrg13a	11	55.17109	5.517109	31.35895	0.856876
Mrg13b	9	129.9839	16.24799	58.84092	0.376371
Mrg15a	10	20.93843	2.326492	5.576005	0.669946
Mrg15b	10	140.9407	15.66008	47.50627	0.660072
Mrg17a	8	38.34626	5.478037	16.19663	0.936362
Mrg17b	8	90.49386	12.92769	51.4325	0.997253
Mrg17c	8	4.163823	0.594832	1.027278	1
Mrg18a	6	32.93923	6.587845	24.20472	0.618575
Mrg18b	6	49.49362	9.898724	20.75611	0.04469
Mrg19a	4	2.057924	0.685975	1.277926	1

Mrg19b	4	29.57924	9.859746	26.87708	0.99791
Mrg19c	4	32.50133	10.83378	21.6694	0.969805
Mrg20a	5	47.04567	11.76142	31.40541	0.971396
Mrg20b	4	66.17762	22.05921	56.18491	0.95627
Mrg20c	5	27.79934	6.949834	23.06374	0.931541
Mrg20d	4	28.58354	9.527848	14.62282	1
Mrg21a	4	64.7426	21.58087	58.1711	0.93429
Mrg21b	3	37.09559	18.5478	37.09558	0.950815
Mrg21c	3	4.244177	2.122089	2.941701	1
Mrg21d	3	5.631076	2.815538	4.801458	NA
Mrg23a	3	22.22009	11.11005	16.93739	0.994251
Mrg24a	4	32.59005	10.86335	31.04596	0.82831
Mrg24b	4	66.19362	22.06454	34.07122	0.722347
Mrg28a	9	60.12802	7.516002	21.40523	0.857423
Mrg28b	12	14.76977	1.342707	4.681651	0.278436
Mrg33a	16	8.120534	0.541369	1.923735	0.993085
Mrg33b	14	4.811966	0.370151	2.142079	0.006216

* NA in R2 indicates that only 1 marker on the LG had a map position in the oat consensus map

Supplemental Table S3. Biparental Population ANOVA p-values

Effect	HD	PH	SPM	UA	LVSS
Cross	<0.001	<0.001	0.003	<0.001	<0.001
Environment (E)	<0.001	<0.001	0.111	<0.001	<0.001
Cross/Line (G)	<0.001	<0.001	0.492	<0.001	0.015
Cross x Environment	<0.001	<0.001	0.721	0.005	0.039
(Cross/Line) x Environment (GxE)	0.113	0.002	0.712	0.002	0.039

Supplemental Table S4. HD LOD scores for biparental population cross A (Bonferroni threshold = 4.07)

Marker	Linkage Group	Position (cM)	Consensus Linkage Group	Consensus Position (cM)	Crk Early	Crk Late	St Paul Early	St Paul Late
GMI_ES01_c8165_708	Mrg02a	0	Mrg02	34.1	17.9	16.4	11.5	15.5
GMI_ES03_c4395_765	Mrg02a	4.7	Mrg02	33	29.5	28.6	19.8	23.9
GMI_ES_LB_11316	Mrg02a	4.7	Mrg02	34.1	29.5	28.6	19.8	23.9
GMI_ES_LB_7578	Mrg02a	20.8	Mrg02	13.2	15.7	14.4	11.9	12.9
GMI_ES17_c19068_531	Mrg02a	22	Mrg02	7.9	13.9	12.6	10.9	11.4
GMI_ES05_c5613_127	Mrg02a	27.3	Mrg02	0	9.8	9.7	7.7	8.8
GMI_ES02_c2412_830	Mrg02a	27.3	Mrg02	0	9.8	9.7	7.7	8.8
GMI_ES_LB_11625	Mrg02c	0	Mrg02	0	9.8	9.6	7.8	8.8
GMI_DS_LB_147	Mrg02c	6.4	Mrg12	35.2	15.7	14.6	11.8	13.5
GMI_ES03_c15766_534	Mrg02c	10.8	Mrg02	16.2	22.4	22.3	16.4	19.3
GMI_DS_LB_3922	Mrg02c	17.1	Mrg02	30.1	31.2	30.3	20.2	24
GMI_ES01_c15198_534	Mrg02c	19.1	Mrg02	30.1	31.6	30.9	21.5	25.7

Supplemental Table S5. HD LOD scores for biparental population cross B (Bonferroni threshold = 3.96)

Marker	Linkage Group	Position (cM)	Consensus Linkage Group	Consensus Position (cM)	Crk Early	Crk Late	St Paul Early	St Paul Late
GMI_ES03_c649_134	Mrg02a	0	Mrg02	2.7	8.9	6.5	7.6	4.8
GMI_DS_LB_147	Mrg02a	16.2	Mrg12	35.2	16.5	12	10.4	10.1
GMI_ES03_c15766_534	Mrg02a	20	Mrg02	16.2	20.1	15.7	12.7	13
GMI_GBS_22030	Mrg02a	21.8	Mrg02	27.4	21.1	16.8	14.6	14.1
GMI_DS_LB_860	Mrg02a	30.2	Mrg02	28.1	22.1	15.8	12.9	15
GMI_ES15_c1210_347	Mrg02a	36.6	Mrg02	30.1	33.7	21.3	19	23.4
GMI_ES01_c15144_154	Mrg02a	36.6	Mrg02	30.1	33.7	21.3	19	23.4
GMI_ES15_c8389_147	Mrg02a	38.3	Mrg02	34.1	35.7	22.2	20.3	23.8

Supplemental Table S6. PH LOD scores for biparental population cross A (Bonferroni threshold = 4.07)

Marker	Linkage Group	Position (cM)	Consensus Linkage Group	Consensus Position (cM)	Crk Early	Crk Late	St Paul Early	St Paul Late
GMI_ES01_c8165_708	Mrg02a	0	Mrg02	34.1	14.2	6.1	3.7	7.2
GMI_ES03_c4395_765	Mrg02a	4.7	Mrg02	33	17.2	6.5	6.9	7.9
GMI_ES_LB_11316	Mrg02a	4.7	Mrg02	34.1	17.2	6.5	6.9	7.9
GMI_ES_LB_7578	Mrg02a	20.8	Mrg02	13.2	8.6	3.8	3.9	5.4
GMI_ES17_c19068_531	Mrg02a	22	Mrg02	7.9	8.8	3.7	4.6	5.1

GMI_ES05_c5613_127	Mrg02a	27.3	Mrg02	0	7.6	3.3	3.8	4.6
GMI_ES02_c2412_830	Mrg02a	27.3	Mrg02	0	7.6	3.3	3.8	4.6
GMI_ES_LB_11625	Mrg02c	0	Mrg02	0	7.8	3.3	3.9	5
GMI_DS_LB_147	Mrg02c	6.4	Mrg12	35.2	10.6	4.9	4.9	6.6
GMI_ES03_c15766_534	Mrg02c	10.8	Mrg02	16.2	13.4	6.4	6.4	7.3
GMI_DS_LB_3922	Mrg02c	17.1	Mrg02	30.1	17.4	7.9	7.3	9.5
GMI_ES01_c15198_534	Mrg02c	19.1	Mrg02	30.1	19.2	7.8	8.9	9.2

Supplemental Table S7. PH LOD scores for biparental population cross B (Bonferroni threshold = 3.96)

Marker	Linkage Group	Position (cM)	Consensus Linkage Group	Consensus Position (cM)	Crk Early	Crk Late	St Paul Early	St Paul Late
GMI_ES03_c649_134	Mrg02a	0	Mrg02	2.7	2.1	0.4	1.5	2.5
GMI_DS_LB_147	Mrg02a	16.2	Mrg12	35.2	2.3	0	2.4	4
GMI_ES03_c15766_534	Mrg02a	20	Mrg02	16.2	3.7	0.1	3.3	4.5
GMI_GBS_22030	Mrg02a	21.8	Mrg02	27.4	4.4	0.1	3.6	5.5
GMI_DS_LB_860	Mrg02a	30.2	Mrg02	28.1	5.9	0.4	5.9	6.1
GMI_ES15_c1210_347	Mrg02a	36.6	Mrg02	30.1	7.5	0.7	7	7.8
GMI_ES01_c15144_154	Mrg02a	36.6	Mrg02	30.1	7.5	0.7	7	7.8
GMI_ES15_c8389_147	Mrg02a	38.3	Mrg02	34.1	8.1	0.8	6.7	7.4

Supplemental Table S8. UA LOD scores for biparental population cross B (Bonferroni threshold = 3.96)

Marker	Linkage Group	Position (cM)	Consensus Linkage Group	Consensus Position (cM)	St Paul Late
GMI_ES17_c1186_142	Mrg01a	26	Mrg01	24.7	7.1
GMI_DS_LB_860	Mrg02a	30.2	Mrg02	28.1	9.1
GMI_ES03_c2590_477	Mrg03a	95.4	Mrg03	83.8	5
GMI_GBS_1994	Mrg20a	28.2	Mrg20	236.4	4.7
GMI_GBS_115266	Mrg20a	93.1	Mrg20	195.6	4.6
GMI_ES13_c626_111	Mrg20c	52.4	Mrg20	18	5.1
GMI_ES05_c3954_482	Mrg21b	0	Mrg21	142	8
GMI_ES22_lrc15031_170	Mrg24a	10.7	Mrg24	13.1	7.2
GMI_ES15_c285_271	Mrg24b	9.2	Mrg24	24.4	7.7

Supplemental Figure S1. Cross A biparental linkage map

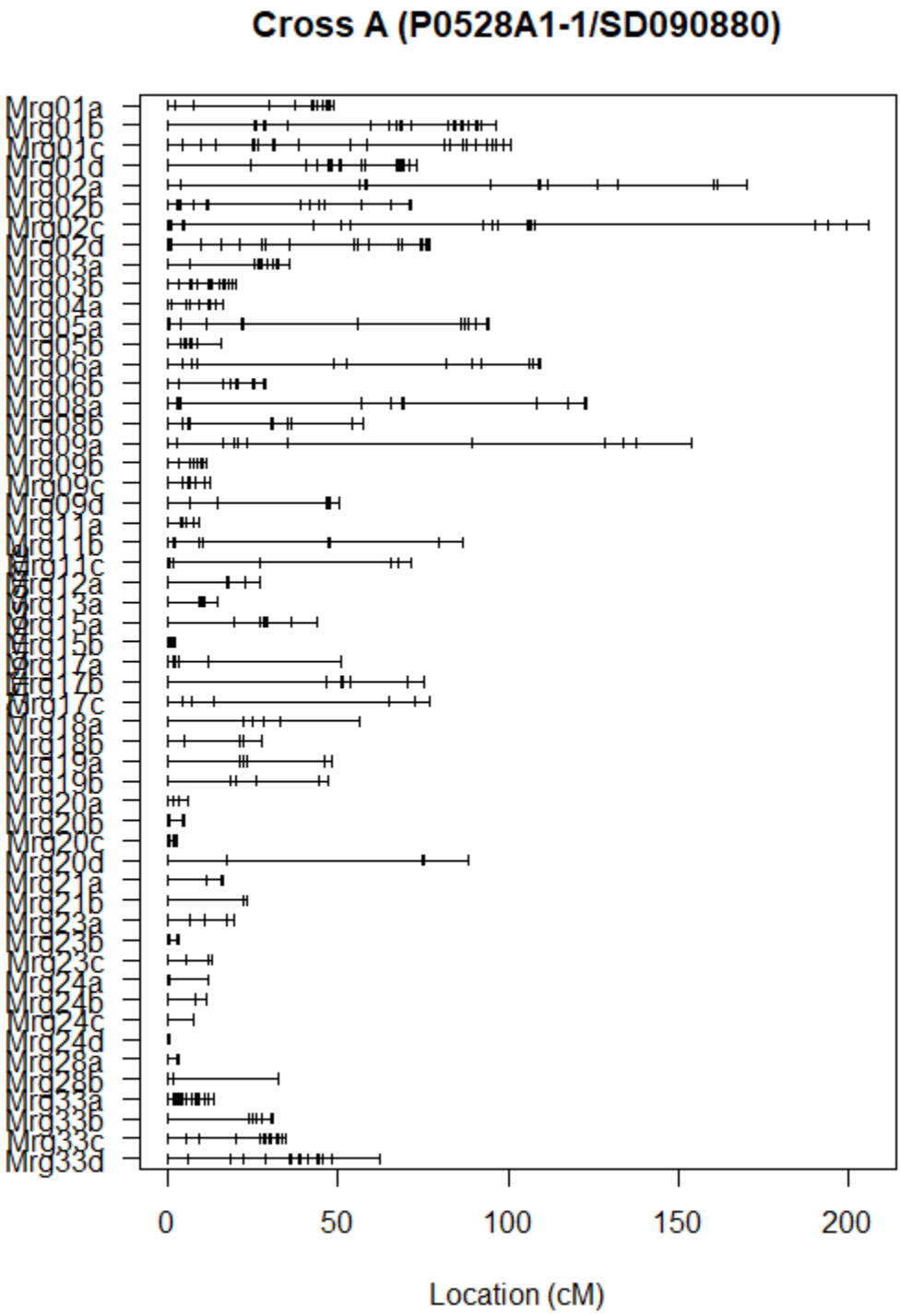

Supplemental Figure S2. Cross B biparental linkage map

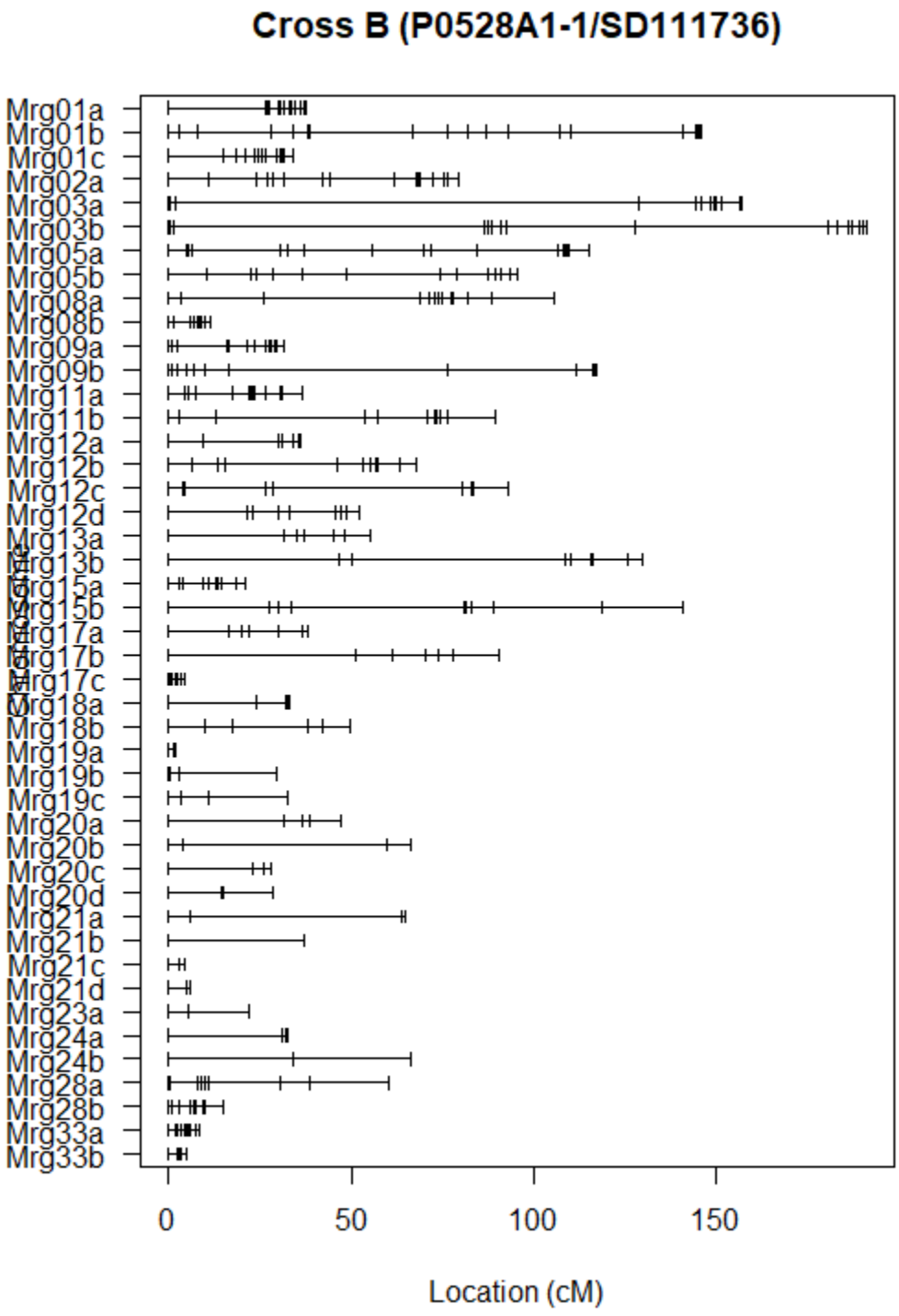

Supplemental Figure S3. SPM associations in individual environments

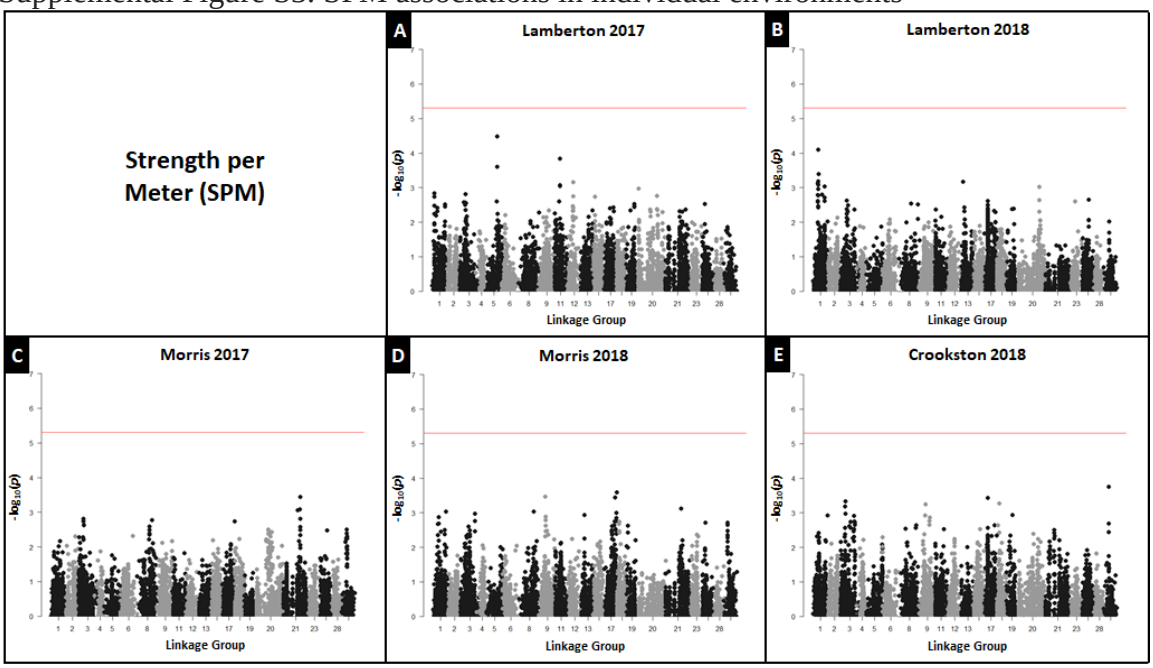

Supplemental Figure S4. UA associations in individual environments

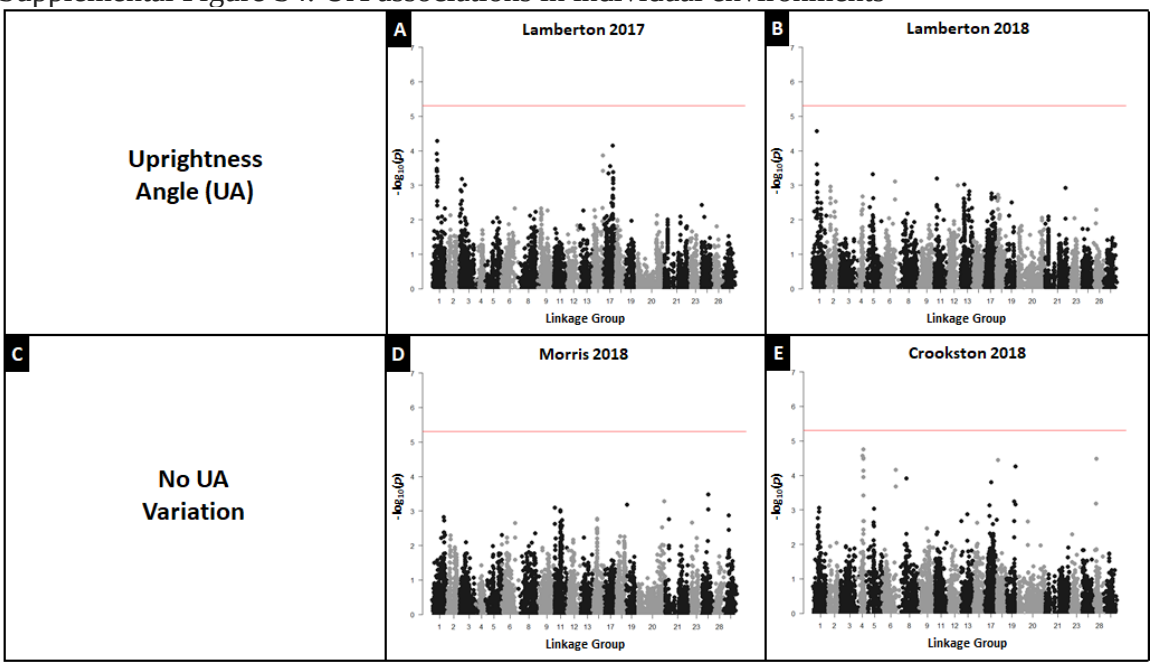

Supplemental Figure S5. RLI associations in individual environments

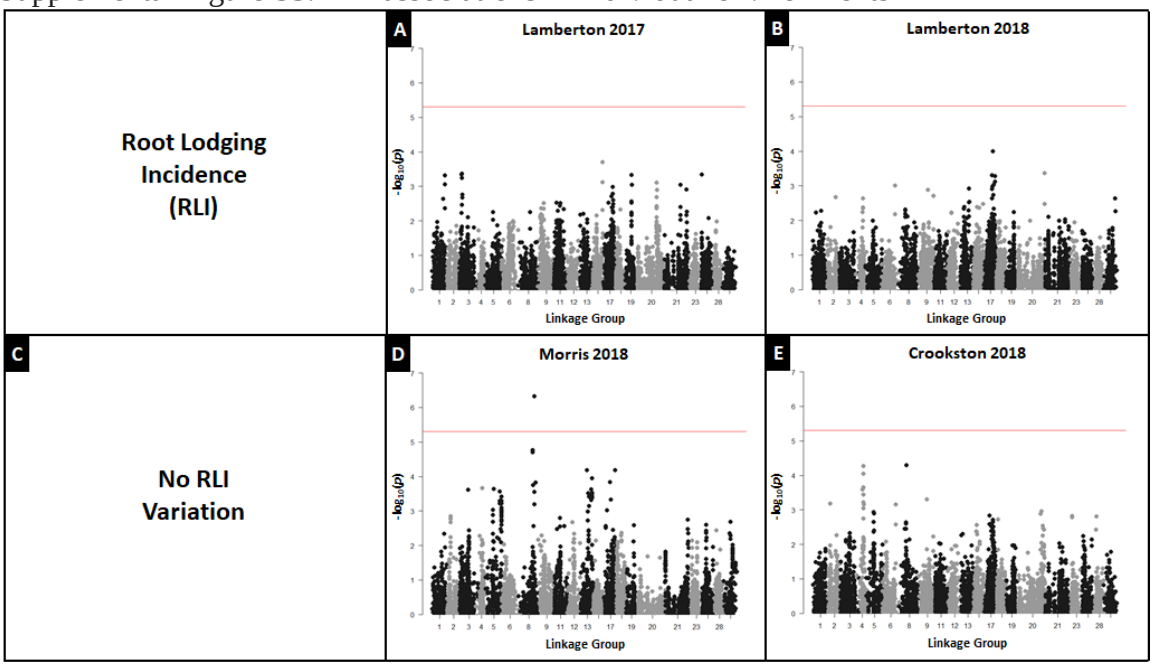

Supplemental Figure S6. SLI associations in individual environments

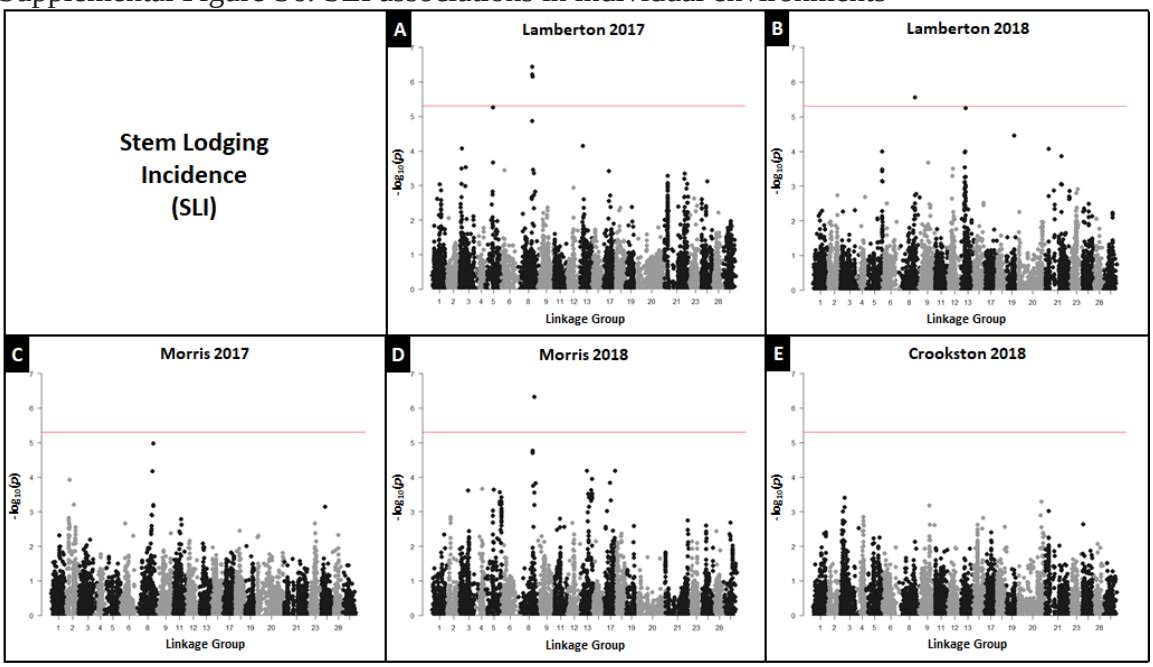

Supplemental Figure S7. LVSS associations in individual environments

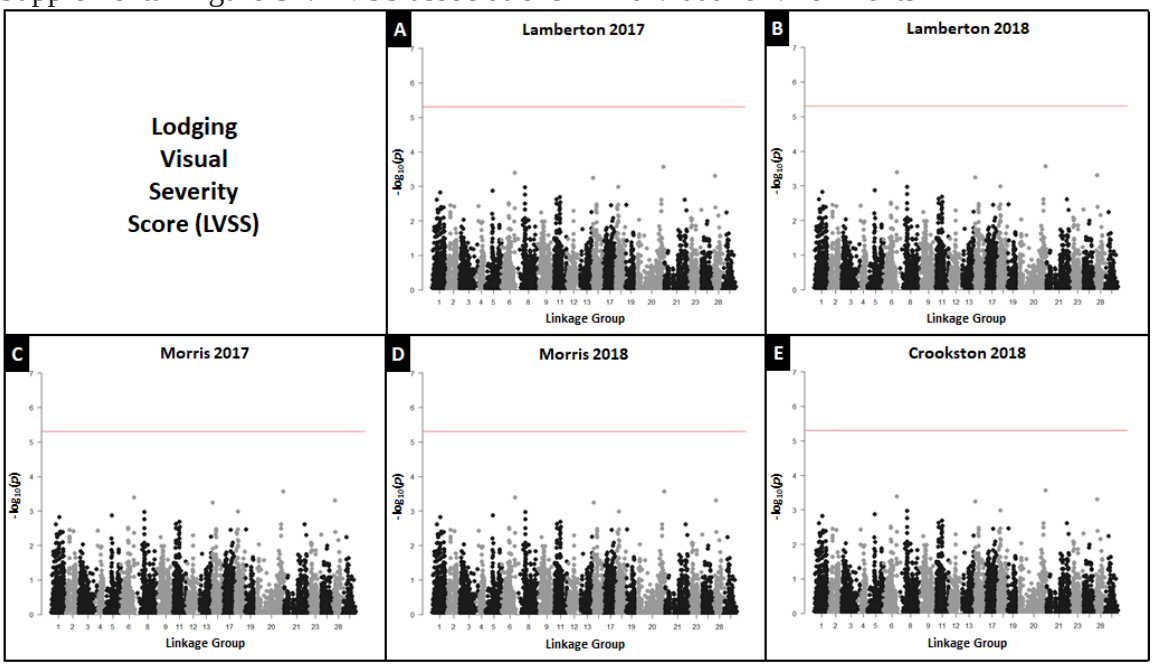

Supplemental Figure S8. QQ plots for lodging traits

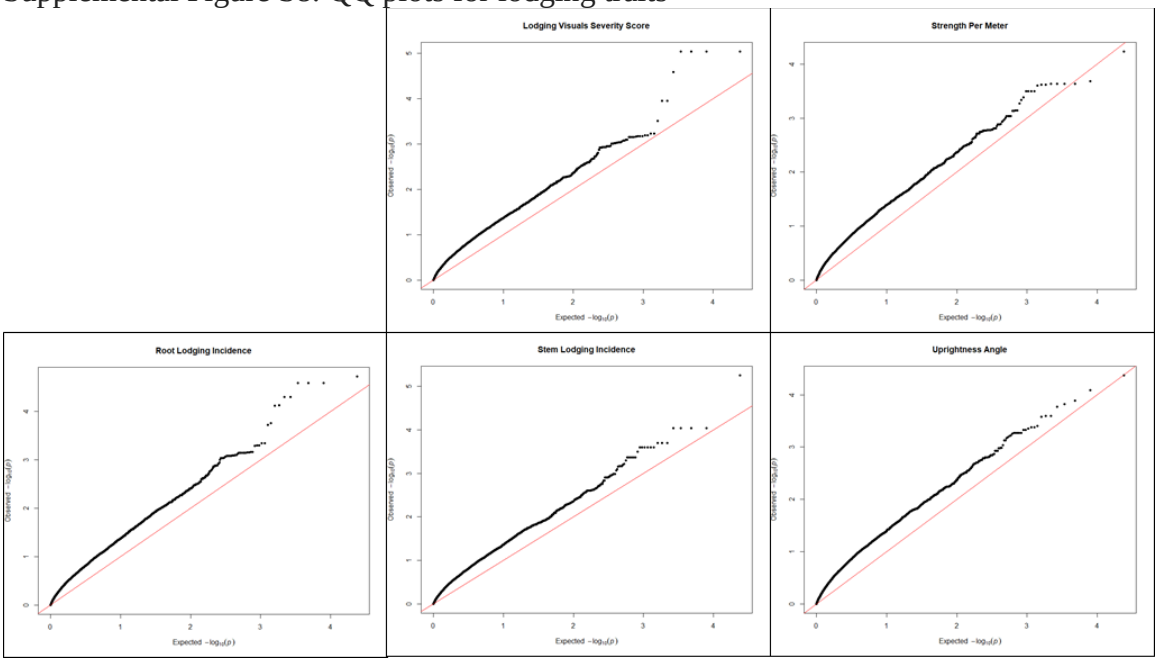

Supplemental Figure S9, QQ plots for related agronomic traits